



(2)

**RESEARCH AND DEVELOPMENT TECHNICAL REPORT**  
**CECOM-TR-85-1**

**A TRANSPORT THEORY OF MILLIMETER WAVE PROPAGATION  
IN WOODS AND FORESTS**

**AD-A151 883**

R. A. JOHNSON AND F. SCHWERING  
CENTER FOR COMMUNICATIONS SYSTEMS

FEBRUARY 1985

**DISTRIBUTION STATEMENT**

Approved for public release;  
distribution is unlimited.

**DTIC FILE COPY**

**CECOM**

**U S ARMY COMMUNICATIONS-ELECTRONICS COMMAND  
FORT MONMOUTH, NEW JERSEY 07703**

**DTIC  
SELECTED  
APR 01 1985  
S E D  
E**

**85 03 13 032**

## **NOTICES**

### **Disclaimers**

**The citation of trade names and names of manufacturers in this report is not to be construed as official Government endorsement or approval of commercial products or services referenced herein.**

### **Disposition**

**Destroy this report when it is no longer needed. Do not return it to the originator.**

**REPORT DOCUMENTATION PAGE**

1a. REPORT SECURITY CLASSIFICATION Unclassified		1b. RESTRICTIVE MARKINGS			
2a. SECURITY CLASSIFICATION AUTHORITY		3. DISTRIBUTION/AVAILABILITY OF REPORT Approved for public release; distribution is unlimited.			
2b. DECLASSIFICATION/DOWNGRADING SCHEDULE		5. MONITORING ORGANIZATION REPORT NUMBER(S)			
4 PERFORMING ORGANIZATION REPORT NUMBER(S) CECOM-TR-85-1		7a. NAME OF MONITORING ORGANIZATION			
6a. NAME OF PERFORMING ORGANIZATION US Army Communications-Electronics Command (CECOM), CENCOMS	6b. OFFICE SYMBOL (if applicable) AMSEL-COM-RM-4	7b. ADDRESS (City, State, and ZIP Code)			
6c. ADDRESS (City, State, and ZIP Code) Center for Communications Systems (CENCOMS) Multichannel Transmission Division, ATTN: AMSEL-COM-RM-4, Fort Monmouth, NJ 07703-5202		8. PROCUREMENT INSTRUMENT IDENTIFICATION NUMBER			
8a. NAME OF FUNDING/SPONSORING ORGANIZATION	8b. OFFICE SYMBOL (if applicable)	10. SOURCE OF FUNDING NUMBERS			
8c. ADDRESS (City, State, and ZIP Code)		PROGRAM ELEMENT NO. 1L161102	PROJECT NO. AH48	TASK NO. PM11	WORK UNIT ACCESSION NO. 01
11. TITLE (Include Security Classification) <b>A TRANSPORT THEORY OF MILLIMETER WAVE PROPAGATION IN WOODS AND FORESTS</b> (W4C1)					
12. PERSONAL AUTHOR(S) R.A. Johnson and F. Schwering					
13a. TYPE OF REPORT Technical Report	13b. TIME COVERED FROM July 82 to July 84	14. DATE OF REPORT (Year, Month, Day) 1985 February		15. PAGE COUNT 84	
16. SUPPLEMENTARY NOTATION					
17. COSATI CODES		18. SUBJECT TERMS (Continue on reverse if necessary and identify by block number) Keywords: Millimeter Wave Propagation; RF Propagation in Woods/Forests; Terrain Effects on Millimeter Wave Transmission; Transport Theory; (contd)			
FIELD 17 20	GROUP 02 14				
19. ABSTRACT (Continue on reverse if necessary and identify by block number) A theory of mm wave propagation in woods and forests is presented which models the vegetation environment as a statistically homogeneous random medium of scatterers characterized by a scatter function (phase function) with a narrow forward lobe and an omnidirectional background. The model describes the medium in terms of four overall theoretical parameters whose numerical values can be determined in principle by comparison of analytical results and experimental data. The scalar transport theory is used to determine the coherent and incoherent field intensities in the forest medium; the problem solved is that of a vegetation halfspace illuminated by a plane wave. Formulas and graphs are presented on the range dependence of the coherent and incoherent intensities, and on the angular spectrum (beam broadening) of the incoherent intensity. Comparison with experimental results obtained by an independent investigation has shown good qualitative agreement of calculated and measured results. Both show that the (contd)					
20. DISTRIBUTION/AVAILABILITY OF ABSTRACT <input checked="" type="checkbox"/> UNCLASSIFIED/UNLIMITED <input type="checkbox"/> SAME AS RPT. <input type="checkbox"/> DTIC USERS		21. ABSTRACT SECURITY CLASSIFICATION Unclassified			
22a. NAME OF RESPONSIBLE INDIVIDUAL F. Schwering		22b. TELEPHONE (Include Area Code) (201) 544-5362		22c. OFFICE SYMBOL AMSEL-COM-RM-4	

~~UNCLASSIFIED~~

~~SECURITY CLASSIFICATION OF THIS PAGE~~

18. SUBJECT TERMS (continued)

Random Media; Coherent and Incoherent Field Components; Range Dependence and Beamwidening of Millimeter Waves in Vegetation.

20. ABSTRACT (continued)

attenuation rate of mm waves decreases from a high value at short distances into vegetation to a lower value at long distances, and that significant beam broadening occurs leading to a broad beamwidth at large vegetation depths. Reasonably good quantitative agreement of experimental and theoretical curves can be obtained at large distances into the vegetation medium (by appropriate adjustment of the parameters of the theoretical model). At short vegetation depths, the measured data indicates a higher attenuation rate than can be accommodated by the present theory.

Accession For	
NTIS GRA&I	<input checked="" type="checkbox"/>
DTIC TAB	<input type="checkbox"/>
Unannounced	<input type="checkbox"/>
Justification	
By	
Distribution/	
Availability Codes	
Serial and/or Dist. Specif.	
A-1	

Page No.



I. INTRODUCTION	1
II. THEORY	3
1. Fundamentals	3
2. Formulation of the Problem	7
3. Solution of the Problem	13
4. Power Received by Highly Directive Antenna	30
III. NUMERICAL EVALUATION	35
IV. EXPERIMENTS	52
1. Description of Experiments	52
2. Experimental Results	53
3. Comparison of Theory and Experiments	58
V. CONCLUSIONS	66
REFERENCES	69
APPENDIX A. Energy Density Associated with $I_1$ .	71
APPENDIX B. Solution of Recursion Relation for $I_1$ .	73
APPENDIX C. Asymptotic Behavior of $I_2$ .	79

## FIGURES

	<u>Page No.</u>
Fig. 1. Definition of Specific Intensity $I$ .	5
Fig. 2. Cylindrical Volume Element in Random Medium of Scatterers.	6
Fig. 3. Forest Halfspace ( $Z > 0$ ) Illuminated by Plane Wave.	8
Fig. 4. Phasefunction with Narrow Forward Lobe and Isotropic Background.	10
Fig. 5. Overlapping Triangular Basis Functions for Interval $-1 \leq \mu \leq +1$ .	20
Fig. 6. Solution of Characteristic Equation (32).	23
Fig. 7. Asymptotic Eigenvalue $S_a$ vs. $\hat{W}$ .	27
Fig. 8. Asymptotic Directional Spectrum.	28
Fig. 9. Asymptotic Amplitude $A_a$ vs. $\hat{W}$ .	29
Fig. 10. Receive Antenna in Forest Halfspace.	31
Fig. 11. Range Dependence of Received Power for Normal Incidence and $\alpha = 0.2$ .	37
Fig. 12. Range Dependence of Received Power for Normal Incidence and $\alpha = 0.5$ .	38
Fig. 13. Range Dependence of Received Power for Normal Incidence and $\alpha = 0.8$ .	39
Fig. 14. Directional Dependence of Received Power for Normal Incidence and $\alpha = 0.5$ , $W = 0.75$ . (a) $360^0$ Scan (b) Expanded $\theta$ -Scale	40 41
Fig. 15. Directional Dependence of Received Power for Normal Incidence and $\alpha = 0.5$ , $W = 0.9$ .	42
Fig. 16. Directional Dependence of Received Power for Normal Incidence and $\alpha = 0.5$ , $W = 0.95$ . (a) $360^0$ Scan (b) Expanded $\theta$ -Scale	43 44
Fig. 17. Directional Dependence of Received Power for Normal Incidence and $\alpha = 0.2$ , $W = 0.9$ .	45

Page No.

Fig. 18.	Directional Dependence of Received Power for Normal Incidence and $\alpha = 0.8$ , $W = 0.9$ .	
	(a) 360° Scan	46
	(b) Expanded $\theta$ -Scale	47
Fig. 19.	Range Dependence of Received Power for Oblique Incidence and $\alpha = 0.5$ .	48
Fig. 20.	Directional Dependence of Received Power for Oblique Incidence and $\alpha = 0.5$ , $W = 0.9$ .	49
Fig. 21.	Photograph of Test Site Used for Vegetation Experiments, (a) Trees without Leaves (April), (b) Trees in Leaf (August).	54
Fig. 22.	Drawing of Test Area	55
Fig. 23.	Received Power in dB (Vegetation Loss) as Function of Number of Trees in Path.	56
Fig. 24.	Received Power in dB (Vegetation Loss) as Function of Number of Trees in Path.	57
Fig. 25.	Directional Dependence of Received Power at Height of 4 m with 1, 3, 8 and 11 Trees in Path	59
Fig. 26.	Directional Dependence of Received Power at Height of 6 m with 1, 3, 8 and 11 Trees in Path.	60
Fig. 27.	Comparison of Theoretical and Experimental Range Dependence.	64
Fig. 28.	Comparison of Theoretical and Experimental Range Dependence.	65
Fig. 29.	Advanced Theoretical Model for the Analysis of Millimeter Wave Propagation in Woods and Forests.	68
Fig. B1.	Directions $\theta$ , $\phi$ and $\theta'_p$ , $\phi'_p$ and $\phi'$ , $\phi'$ .	75
Fig. B2.	Local Coordinate System on Unit Sphere (Planar Projection).	76

## I. INTRODUCTION

The objective of this investigation is the development of a theoretical model for propagation of Extremely High Frequency (EHF) radio waves in a strongly scattering medium such as a forest. The forest is described as a random medium which, in first approximation, may be regarded as statistically homogeneous; and wave propagation in this medium is characterized by the theory of radiative energy transfer (transport theory). This theory permits one to take multiple scattering effects fully into account while interference effects are neglected. Experimental evidence confirms that the coherence length of mm waves in vegetation is short so that the suppression of interference effects is an acceptable approximation.

All scatter objects in a forest environment, including tree trunks, branches, and leaves, or pine needles, have large dimensions compared to a wavelength in the mm-wave region. As a consequence, the forest medium will produce strong forward scattering and its scatter characteristic (phase function) may be represented by a pronounced forward lobe with an isotropic background. Assuming this type of phase function, the medium is characterized by four parameters: the absorption cross section per volume  $\sigma_A$ , the (total) scatter cross section per volume  $\sigma_S$ , the beam width  $\Delta\gamma_S$  of the forward scatter lobe, and the ratio  $\alpha$  of the forward scattered power and the total scattered power.

These four quantities are determined by the macroscopic and microscopic structure parameters of the forest and, in principle, can be derived from these parameters. No attempt is made here to establish this relation theoretically. Considering the structural complexity of the forest environment, this would appear to be a hopeless task. Rather, the transport equation is formulated and solved in general terms and the dependency of the solutions on the parameters  $\sigma_A$ ,  $\sigma_S$ ,  $\Delta\gamma_S$  and  $\alpha$  is established. Comparison with experimental results then permits one to determine estimates for these parameters by adjusting them such that the theoretical curves agree with the experimental data. At the same time, the theory serves to explain and interpret the experimental results. Theory and experiments are shown to be in good qualitative agreement. The experimental data utilized in this report was obtained by Violette and Espeland [1, 2]. Achieving good quantitative agreement, however, is not without difficulties. A larger measured data base and a refinement of the theory will probably be required.

Propagation characteristics to be determined include the range dependence of both the coherent and incoherent field components of mm-wave beams transmitted through woods and forests, and the directional spectrum of the incoherent component (beam broadening) as a function of vegetation depth and density. The theory shows, in particular, that the range dependence is not determined by a simple exponential decrease in signal strength at constant attenuation rate but a high attenuation rate at short distances into woods gradually transforms into a much lower attenuation rate at large distances. This complex range dependence has been confirmed by the experiments and is explained by the interplay of the coherent (direct path) component, which dominates at short distances into woods but is strongly attenuated, and the incoherent (multiply-scattered) component, which is less attenuated and takes over at large distances. The transition is accompanied by substantial beam broadening. The comparison of theory and experiments indicates, furthermore, that the parameter  $\alpha$  is close to unity and that  $\sigma_S \gg \sigma_A$ . In other words, forward scattering seems to be strong and scattering seems to dominate over absorption.

## II. THEORY

### 1. Fundamentals

The electromagnetic field in a random medium of scatterers can be split into two parts, the coherent component and the incoherent component. The coherent component is the average field which at any point in space has a well-defined direction of propagation and a well-defined polarization. This component decreases due to both absorption and scatter, and its attenuation rate is comparatively high. The incoherent component is the zero-mean field. It is generated by the scattering of the coherent component and consists of many wave trains propagating in various directions. Hence, at any point in space, the incoherent component does not have a unique direction of propagation but is characterized by a directional spectrum. In transport theory, it is assumed that the constituent wave trains are uncorrelated in phase and add in power. The incoherent component decreases at a slower rate than the coherent component since it is attenuated due to absorption only (though over an increased path length) while it scatters into itself. Scattering of the incoherent component reproduces the incoherent component. In general, this field component is partially depolarized.

While the coherent component will dominate at short distances from a coherent source, the incoherent component takes over at large distances, leading to a reduced attenuation rate, significant beam broadening, and depolarization. The coherent and incoherent field components are powerwise orthogonal. If  $\bar{E}$  is the electric field strength in a random medium, then the average field intensity is given by

$$\langle \mathbf{E} \cdot \mathbf{E}^* \rangle = \langle \bar{E} \rangle \langle \bar{E}^* \rangle + \langle \Delta \mathbf{E} \cdot \Delta \mathbf{E}^* \rangle \quad \text{with } \Delta \bar{E} = \bar{E} - \langle \bar{E} \rangle$$

In other words, the total intensity is the sum of the intensities of the coherent and incoherent field components.

The fundamental quantity used in transport theory is the specific intensity  $I(\mathbf{r}, \mathbf{s})$  which is defined as the power per unit area and per unit solid angle propagating at point  $\mathbf{r}$  into the direction  $\mathbf{s}$ :

$$I(\mathbf{r}, \mathbf{s}) = \frac{dP(\mathbf{r}, \mathbf{s})}{da d\Omega} \quad (1)$$

Here,  $da$  is the area of the surface element (at point  $\mathbf{r}$ ) normal to the unit vector  $\mathbf{s}$ , and  $d\Omega$  is the differential of the solid angle  $\Omega$  centered about  $\mathbf{r}$ ; see

Fig. 1. Definition (1) applies to time harmonic fields in a time independent random medium, the case considered here. (Wind induced motion in woods and forests is negligibly slow compared to the travel times of EM signals.) The specific intensity can be used to characterize both the coherent and incoherent field components. In the case of the coherent component, which has a unique direction of propagation,  $I$  takes the form of a  $\delta$ -function in  $\vec{s}$ .

The transport equation [3], the basic equation of the theory of radiative energy transfer, is obtained by formulating the power conservation theorem in terms of the specific intensity  $I$ . Consider the cylindrical volume  $dV = da \cdot dl$  of Fig. 2, which is centered at point  $\vec{r}$  and whose axis has the direction of the unit vector  $\vec{s}$ . Radiation with the specific intensity  $I(\vec{r}, \vec{s})$  passing through this volume will vary because of two effects:

- (1) Absorption and scattering by the random medium will reduce the power propagating in the direction  $\vec{s}$ . The specific intensity will decrease by the amount

$$dI_1 = -(\sigma_A + \sigma_S) I(\vec{r}, \vec{s}) dl \quad (2)$$

where  $\sigma_A$  is the absorption cross section per unit volume of the random medium and  $\sigma_S$  is the (total) scatter cross section per volume. In general, both  $\sigma_A$  and  $\sigma_S$  depend on  $\vec{r}$ .

- (2) A fraction of the power propagating in other directions  $\vec{s}'$  will be redirected into the direction  $\vec{s}$  by scattering within the volume element  $dV$ . This effect will increase  $I(\vec{r}, \vec{s})$  by an amount which is determined by the scatter characteristic\* of the medium  $p(\vec{s}, \vec{s}')$ . The increase of  $I(\vec{r}, \vec{s})$  is given by

$$dI_2 = \frac{1}{4\pi} \sigma_S \iint_{4\pi} p(\vec{s}, \vec{s}') I(\vec{r}, \vec{s}') d\Omega' dl \quad (3)$$

where the integration is performed over all spatial directions  $\vec{s}'$  and  $p$  is assumed normalized such that

$$\frac{1}{4\pi} \iint_{4\pi} p(\vec{s}, \vec{s}') d\Omega' = 1 \quad (4)$$

---

\*In transport theory  $p(\vec{s}, \vec{s}')$  is usually called the "phase function" of the scatter medium, though it is not related in any way to the phases of the electric or magnetic field strengths.

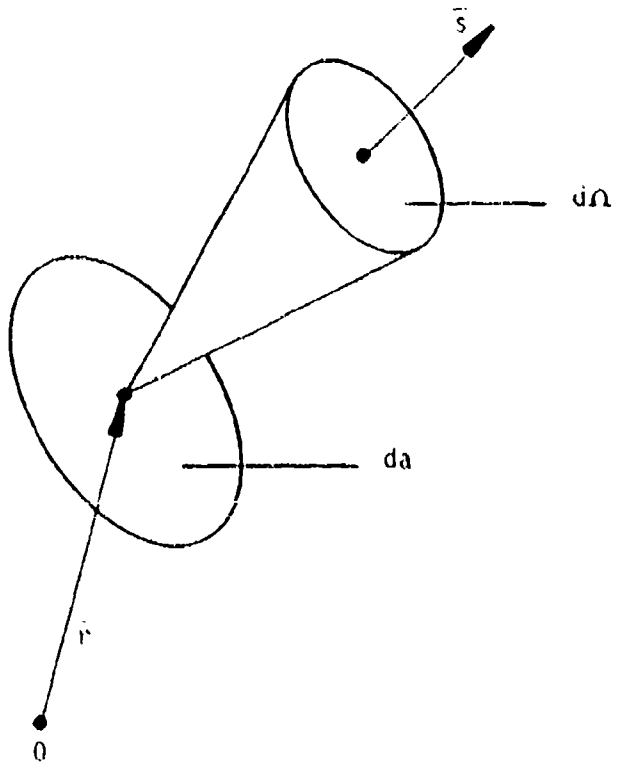


FIGURE 1: Definition of Specific Intensity  $I$

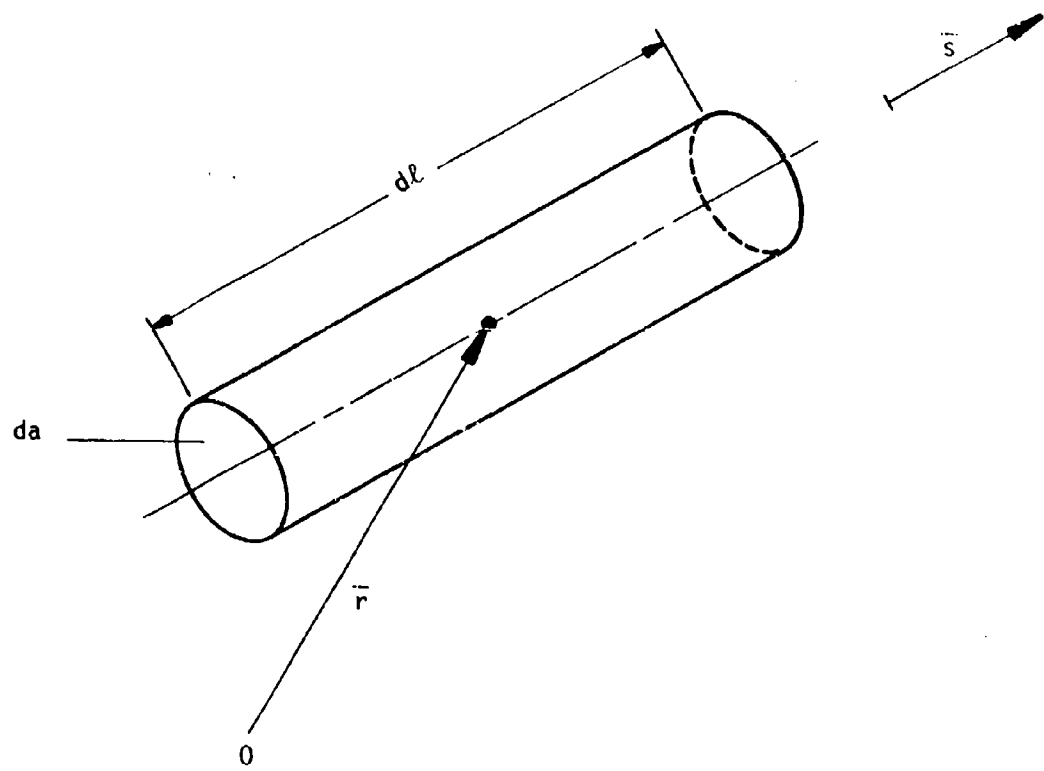


FIGURE 2: Cylindrical Volume Element in Random Medium of Scatterers

Similar to  $\sigma_A$  and  $\sigma_S$ , the scatter characteristic, in general, will be a function of  $\vec{r}$ . Reciprocity requires that  $p$  is symmetric in  $\vec{s}$  and  $\vec{s}'$ :

$$p(\vec{s}, \vec{s}') = p(\vec{s}', \vec{s}) \quad (5)$$

The total variation of the specific intensity  $I$  over the length  $dl$  of the volume element  $dV$  is the sum of  $dI_1$  and  $dI_2$ :

$$dI \equiv [\vec{s} \cdot \text{grad } I(\vec{r}, \vec{s})] dl = dI_1 + dI_2$$

Hence, with Equations (2) and (3):

$$\begin{aligned} \vec{s} \cdot \text{grad } I(\vec{r}, \vec{s}) + (\sigma_A + \sigma_S) I(\vec{r}, \vec{s}) \\ = \frac{\sigma_S}{4\pi} \iint_{4\pi} p(\vec{s}, \vec{s}') I(\vec{r}, \vec{s}') d\Omega' \end{aligned} \quad (6)$$

Equation (6) is the transport equation in its scalar formulation. A forcing term which usually appears on the right side of this equation is omitted here since we will assume that all sources are located outside the random medium. More precisely, we shall assume that the transmit antenna is situated outside the forest at a certain distance from the forest-to-air interface while the receive antenna is placed within the forested region. Reciprocity insures that the same results will be obtained when transmitter and receiver are interchanged.

## 2. Formulation of the Problem

In analyzing mm-wave propagation in woods and forests, we use a simple model which is illustrated in Fig. 3. A forest halfspace is separated by a planar interface from an air halfspace. The forest is characterized as a statistically homogeneous medium of random scatterers. In other words, it is assumed that  $\sigma_A$ ,  $\sigma_S$  and  $p$  do not vary with  $\vec{r}$  and are the same at every point in the medium. Furthermore, we assume that the phase function  $p$  depends only on the scatter angle  $\gamma = \text{arc cos } (\vec{s} \cdot \vec{s}')$  subtended by the directions  $\vec{s}$  and  $\vec{s}'$ . Since, in a forest, all scatter elements are large compared to mm-wavelengths, strong forward scattering will occur and  $p$  is assumed to consist of a narrow Gaussian forward lobe superimposed over an isotropic background, i.e.,

$$p(\gamma) = \alpha \left( \frac{2}{\Delta \gamma_s} \right)^2 e^{-\left( \frac{\gamma}{\Delta \gamma_s} \right)^2} + (1-\alpha) \quad (7)$$

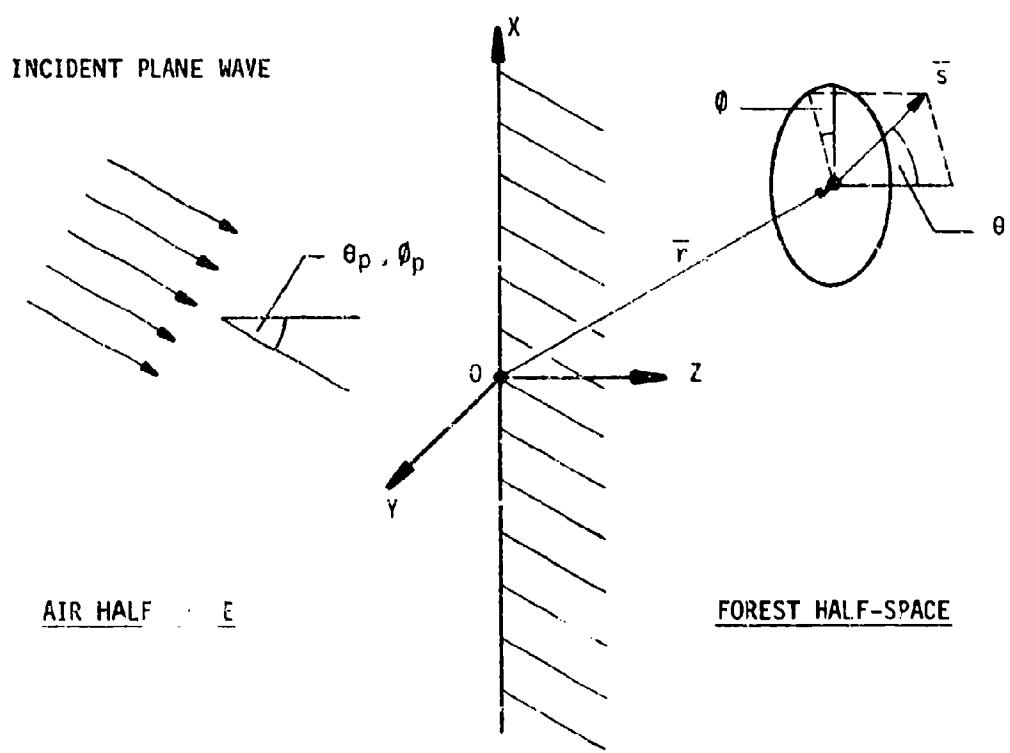


FIGURE 3: Forest Halfspace ( $Z > 0$ )  
Illuminated by Plane Wave

The function  $p(\gamma)$  is indicated in Fig. 4. The width of the forward lobe  $\Delta\gamma_s$  is assumed to be  $\ll\pi$ , and  $\alpha$  is the ratio of the forward scattered and the total scattered power. It is easily verified that  $p(\gamma)$  satisfies Equation (4).

The transmitter in the air halfspace is assumed to be sufficiently far away from the edge of the forest so that the field incident upon the air-to-forest interface can be described as a plane wave. This plane wave may be impinging normally or at an oblique angle. The coordinate system is indicated in Fig. 3. In particular,  $Z$  is the coordinate normal to the interface which is assumed to coincide with the plane  $Z = 0$ ;  $\theta$  is the angle counted from the positive  $Z$ -direction; and  $\phi$  is the projected angle in planes  $Z = \text{constant}$ .

With the above assumptions, the specific intensity  $I$  in the forest medium will depend on the coordinate  $Z$  and the angles  $\theta$  and  $\phi$  only, but it is independent of the cross-sectional coordinates  $x$  and  $y$ . The transport equation (6) then reduces to

$$\begin{aligned} & \cos \theta \frac{\partial I}{\partial Z}(Z; \theta, \phi) + (\sigma_A + \sigma_S) I(Z; \theta, \phi) \\ &= \frac{\sigma_S}{4\pi} \int_0^{2\pi} \int_0^\pi p(\gamma) I(Z; \theta', \phi') \sin \theta' d\theta' d\phi' \quad (8a) \end{aligned}$$

for  $Z > 0$

where

$$\cos \gamma = \cos(\phi - \phi') \sin \theta \sin \theta' + \cos \theta \cos \theta' \quad (8b)$$

In the plane  $Z = 0$ ,  $I$  is determined by the incident plane wave (for all forward directions). Hence, we have the boundary condition

$$I(0; \theta, \phi) = S_p \frac{\delta(\theta - \theta_p)}{\sin \theta} \delta(\phi - \phi_p) \quad \text{for } 0 \leq \theta \leq \frac{\pi}{2} \quad (9a)$$

The symbol  $\delta$  denotes the well known  $\delta$ -function.  $S_p$ ,  $\theta_p$  and  $\phi_p$  are the Poynting vector and the propagation angles of the incident wave. Finally, since the medium is not only scattering but also dissipative,  $I$  must vanish at infinity, i.e.,

$$I(Z; \theta, \phi) \rightarrow 0 \quad \text{for } Z \rightarrow \infty \quad (9b)$$

Equations (8) and (9) provide the transport theory description of the forest model considered here; the equations permit a unique solution of the problem.

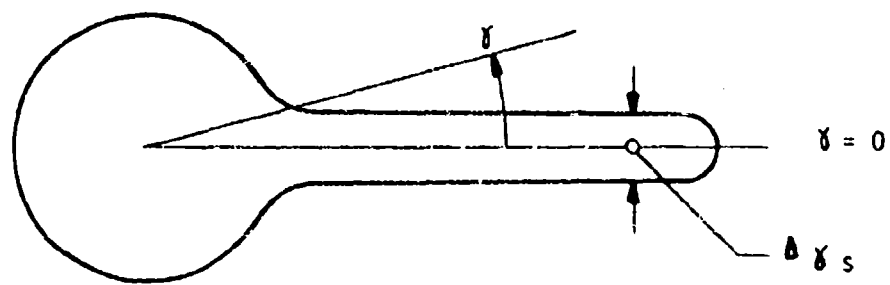


FIGURE 4: Phasefunction with Narrow Forward Lobe  
and Isotropic Background

Mathematically speaking, Equations (8) and (9) formulate the problem in terms of a homogeneous integro-differential equation with an inhomogeneous boundary condition. By a simple transformation, the problem may be reformulated as an inhomogeneous equation with a homogeneous boundary condition. The transformation is discussed here since it provides additional physical insight. We split the specific intensity  $I$  into two parts [3]:

$$I(z; \theta, \phi) = I_{ri}(z; \theta, \phi) + I_d(z; \theta, \phi) \quad (10)$$

where  $I_{ri}$  is called the reduced incident intensity and  $I_d$  the diffuse intensity [3].  $I_{ri}$  is chosen to satisfy the boundary condition in the plane  $z = 0$  and the transport equation (8a) with the interaction term on the right side suppressed, i.e.

$$I_{ri}(0; \theta, \phi) = S_p \frac{\delta(\theta - \theta_p)}{\sin \theta} \delta(\phi - \phi_p) \quad \text{for } 0 \leq \theta \leq \frac{\pi}{2} \quad (11a)$$

$$\cos \theta \frac{\partial I_{ri}}{\partial z} + (\sigma_A + \sigma_S) I_{ri} = 0 \quad \text{for } z \geq 0 \quad (11b)$$

These equations can be solved in closed form:

$$I_{ri}(z; \theta, \phi) = S_p \exp\left\{-\frac{\sigma_A + \sigma_S}{\cos \theta_p} z\right\} \cdot \frac{\delta(\theta - \theta_p)}{\sin \theta_p} \delta(\phi - \phi_p) \quad (12)$$

for  $z \geq 0$

The diffuse intensity then has to satisfy the equations:

$$I_d(0; \theta, \phi) = 0 \quad \text{for } 0 \leq \theta \leq \frac{\pi}{2}, z = 0 \quad (13a)$$

$$I_d(z; \theta, \phi) \rightarrow 0 \quad \text{for } z \rightarrow \infty \quad (13b)$$

$$\begin{aligned} \cos \theta \frac{\partial I_d}{\partial z} + (\sigma_A + \sigma_S) I_d &= \\ &= \frac{\sigma_S}{4\pi} \int_0^{2\pi} \int_0^{\pi} p(\gamma) I_d(z; \theta', \phi') \sin \theta' d\theta' d\phi' \\ &\quad + \frac{\sigma_S}{4\pi} S_p e^{-\frac{\sigma_A + \sigma_S}{\cos \theta_p} z} p(\gamma_p) \quad \text{for } z \geq 0 \end{aligned} \quad (13c)$$

$$\text{with } \cos \gamma_p = \cos(\phi - \phi_p) \sin \theta \sin \theta_p + \cos \theta \cos \theta_p \quad (13d)$$

The second term (forcing item) on the right side of Equation (13c) is the contribution of  $I_{ri}$  to the interaction integral.

Evidently, the reduced incident intensity  $I_{ri}$  is the continuation of the incident plane wave into the random medium where its magnitude decreases exponentially with distance because of absorption and scattering. Similar to the incident plane wave,  $I_{ri}$  has a well-defined direction of propagation; it can be considered as the coherent field component, i.e., as the specific intensity of the average field.

The diffuse intensity  $I_d$ , on the other hand, can be interpreted as the incoherent field component, i.e., it represents the specific intensity of the zero-mean field. The incoherent component is generated by the scattering of the coherent component as represented by the inhomogeneous term in Equation (13c). The energy flow of  $I_d$  directed into the scatter medium is zero in the interface plane  $Z = 0$  where no scattering of the coherent component has taken place as yet. This is formulated by boundary condition (13a).

Before proceeding to solve Equations (13), the problem of characterizing the polarization properties of electromagnetic fields in random media is briefly discussed here. The coherent component has the same well-defined polarization as the incident plane wave. The incoherent component, on the other hand, is in general, partially depolarized. This means that, in actuality, the diffuse component should be represented in terms of the four Stokes parameters and the phase function  $p$  in terms of a  $4 \times 4$  element Stokes matrix, which would result in a formulation of the radiative energy transfer problem in a forest in terms of four coupled integro-differential equations.

However, if reasonable assumptions are made concerning the scatter properties of the forest medium, the Stokes matrix can be simplified and the equation for the first Stokes parameter becomes decoupled from the remaining three equations. The first Stokes parameter is of particular interest since it represents the sum of the intensities associated with two orthogonal polarizations, i.e., it represents the total intensity of the incoherent component at any point in space. The decoupled equation for this first Stokes parameter takes the form of the scalar transport equation considered here (Equations (13)) and permits determination of the range dependence and beam broadening of EM-waves traveling through vegetation. Study of this equation, therefore, appears well justified,

although an investigation of depolarization effects would require consideration of the three remaining equations as well.

The conditions under which decoupling of the equation for the first Stokes parameter occurs can be expressed in terms of the co-polarized and cross-polarized field strength components of scattered wave trains and their correlation. Though conceptually not difficult, a detailed discussion of these conditions is rather tedious and goes beyond the scope of this report. In physical terms, the conditions can be stated simply by considering a wavetrain incident from direction  $\bar{s}'$  and scattered into direction  $\bar{s}$ . Decoupling will occur when the total intensity of the scattered wave train will depend only on the total intensity of the incident wave train but (when averaged over many  $\bar{s}' + \bar{s}$  scatter events with both  $\bar{s}'$  and  $\bar{s}$  fixed) is independent of the polarization properties of the incident radiation. It can be assumed that this condition is satisfied for mm-waves propagating in a forest environment.

### 3. Solution of the Problem.

We write with Equation (7)

$$p(\gamma) = \alpha q(\gamma) + (1 - \alpha) \quad (14a)$$

where

$$q(\gamma) = \left( \frac{2}{\Delta \gamma_s} \right)^2 e^{-\left( \frac{\gamma}{\Delta \gamma_s} \right)^2}, \quad \Delta \gamma_s \ll \pi \quad (14b)$$

is the forward lobe of the phase function  $p$  and  $(1-\alpha)$  is the isotropic background. To solve Equations (13), we split the diffuse intensity  $I_d$  into two parts

$$I_d(z; \theta, \phi) = I_1(z; \theta, \phi) + I_2(z; \theta) \quad (15)$$

where  $I_1$  is determined primarily by the forward lobe  $q(\gamma)$  of the scatter function and  $I_2$  is the remainder of  $I_d$  which is primarily determined by the isotropic background. Thus, Equation (13c) is separated into two equations:

$$\begin{aligned} \cos \theta \frac{\partial I_1}{\partial z} + (\sigma_A + \sigma_S) I_1 &= \frac{\sigma_S}{4\pi} \alpha \int_0^{2\pi} \int_0^\pi q(\gamma) I_1(z; \theta', \phi') \sin \theta' d\theta' d\phi' \\ &+ \frac{\sigma_S}{4\pi} \alpha S_p e^{-\frac{\sigma_A + \sigma_S}{\cos \theta} Z} q(\gamma_p) \end{aligned} \quad (16a)$$

$$\begin{aligned} \cos\theta \frac{\partial I_2}{\partial Z} + (\sigma_A + \sigma_S) I_2 &= \frac{\sigma_S}{4\pi} \alpha \int_0^{2\pi} \int_0^\pi q(\gamma) I_2(z; \theta') \sin\theta' d\theta' d\phi' \\ &+ \frac{\sigma_S}{4\pi} (1 - \alpha) \int_0^{2\pi} \int_0^\pi (I_1(z; \theta', \phi') + I_2(z; \theta')) \sin\theta' d\theta' d\phi' \\ &+ \frac{\sigma_S}{4\pi} (1 - \alpha) S_p e^{-\frac{\sigma_A + \sigma_S z}{\cos\theta_p}} \end{aligned} \quad (16b)$$

for  $Z > 0$

Equations (16) can be interpreted on physical grounds and can be simplified by introducing the following approximations:

- (a) Since the specific intensity  $I_1$  is generated by forward scattering (only the forward lobe  $q$  of the scatter characteristic appears in Equation (16a)), it can be expected that  $I_1$  will be characterized by a strong and relatively narrow peak about the incidence direction of the primary wave, while  $I_1$  will be very small in other directions. Hence, the factor  $\cos\theta$  in the first term on the left side of Equation (16a) can be replaced by  $\cos\theta_p$  which simplifies solution of this equation considerably.
- (b) The specific intensity  $I_2$  is primarily determined by the isotropic background of the scatter characteristic  $p$  and will have a broad directional spectrum. Hence, in evaluating the first integral on the right side of Equation (16b), the function  $q(\gamma)$ , which is characterized by a narrow peak, can be treated as a  $\delta$ -function. With Equations (4) and (8b), we find:

$$\frac{1}{4\pi} \int_0^{2\pi} \int_0^\pi q(\gamma) I_2(z; \theta', \phi') \sin\theta' d\theta' d\phi' \approx I_2(z; \theta, \phi) \quad (18a)$$

(c) In Appendix A, it is shown that with approximation (a)

$$\int_0^{2\pi} \int_0^\pi I_1(z; \theta, \phi) \sin\theta d\theta d\phi = S_p \left\{ \exp\left(-\frac{\sigma_A + (1-\alpha)\sigma_S z}{\cos\theta_p}\right) - \exp\left(-\frac{\sigma_A + \sigma_S z}{\cos\theta_p}\right) \right\} \quad (18b)$$

which simplifies the second integral on the right side of Equation (16b).

With these approximations Equations (16a) and (16b) reduce to

$$\mu_p \frac{\partial I_1}{\partial \tau} + I_1 = \frac{\alpha W}{4\pi} \int_0^{2\pi} \int_{-1}^{+1} q(\gamma) I_1(\tau; \mu', \phi') d\mu' d\phi' \\ + \frac{\alpha W}{4\pi} S_p e^{-\frac{\tau}{\mu_p}} q(\gamma_p) \quad (19a)$$

$$\mu \frac{\partial I_2}{\partial \hat{\tau}} + I_2 = \frac{\hat{W}}{2} \int_{-1}^{+1} I_2(\hat{\tau}; \mu') d\mu' + \frac{\hat{W}}{4\pi} S_p e^{-\frac{\hat{\tau}}{\mu_p}} \quad (19b)$$

where

$$\cos \gamma = \cos (\phi - \phi') [(1-\mu^2)(1-\mu'^2)]^{1/2} + \mu \mu'$$

$$\cos \gamma_p = \cos (\phi - \phi_p) [(1-\mu^2)(1-\mu_p^2)]^{1/2} + \mu \mu_p$$

We have introduced here the following normalizations which are in accordance with common usage:

$$\mu = \cos \theta \quad (20a)$$

$$\mu_p = \cos \theta_p$$

$$\tau = (\sigma_A + \sigma_S) Z = \sigma_t Z \quad (\text{optical density}) \quad (20b)$$

$$\hat{\tau} = (\sigma_A + (1-\alpha) \sigma_S) Z = \hat{\sigma}_T Z = \tau (1-\alpha W)$$

$$W = \frac{\sigma_S}{\sigma_A + \sigma_S} \quad (\text{Albedo}) \quad (20c)$$

$$\hat{W} = \frac{(1-\alpha)\sigma_S}{\sigma_A + (1-\alpha)\sigma_S} = \frac{(1-\alpha)W}{1-\alpha W}$$

Both  $I_1$  and  $I_2$  are assumed to satisfy the boundary conditions (13a) and (13b), i.e.,

$$I_1(\tau; \mu, \phi) = 0 \quad \text{for} \quad \begin{cases} \tau = 0 & 0 \leq \mu \leq 1 \\ \tau \rightarrow \infty & \end{cases} \quad (21a)$$

$$I_2(\hat{\tau}; \mu) = 0 \quad \text{for} \quad \begin{cases} \hat{\tau} = 0 & 0 \leq \mu < 1 \\ \hat{\tau} \rightarrow \infty & \end{cases} \quad (21b)$$

Note that Equation (19b) is the well-known transport equation for isotropic scattering. The only difference is that the scatter cross section is reduced by multiplication with  $(1-\alpha)$  (only the fraction  $1-\alpha$  of the total power scattered in any scatter event is transferred into the isotropic background). The solution of the isotropic transport equation depends only on the coordinates  $\hat{\tau}$  and  $\mu$  (i.e.,  $Z$  and  $\theta$ ) but is independent of  $\phi$ . Hence,  $I_2 = I_2(\hat{\tau}; \mu)$  as indicated already in Equation (15). In contrast,  $I_1$  will, in general, depend on all three coordinates  $\tau$ ,  $\mu$ , and  $\phi$ . The only exception is the case of normal incidence of the primary plane wave ( $\theta_p = 0$ ) where full symmetry about the  $Z$ -direction is maintained and  $I_1$  is independent of  $\phi$ .

### Solution of Equation for $I_1$

Equation (19a) is solved by the method of undetermined coefficients, that is, by writing  $I_1$  in the form:

$$I_1(\tau; \mu, \phi) = (b_1\tau + b_2\tau^2 + b_3\tau^3 + \dots) e^{-\frac{\tau}{\mu_p}} \quad (22)$$

where the  $b_n$  are unknown coefficients. Note that representation (22) already satisfies the boundary condition (21a), that  $I_1$  should vanish at  $\tau = 0$  and  $\infty$ . The  $b_n$ , in general, are functions of  $\mu$  and  $\phi$ .

A recursion relation for these coefficients is obtained by using Equation (22) in Equation (19a) and observing that the latter equation must be satisfied for any  $\tau > 0$ :

$$b_1(\mu, \phi) = \frac{S_p}{4\pi} \frac{\alpha W}{\mu_p} q(\gamma_p) \quad (23a)$$

$$b_m(\mu, \phi) = \frac{1}{4\pi} \frac{\alpha W}{\mu_p} \frac{1}{m} \int_0^{2\pi} \int_{-1}^{+1} q(\gamma) b_{m-1}(\mu', \phi') d\mu' d\phi' \quad (23b)$$

$$m = 2, 3, \dots$$

With the assumed Gaussian forward lobe  $q(\gamma)$ , Equation (14b), the recursion relation can be solved in good approximation in closed form. Details are shown in Appendix B; the result is

$$b_m(\mu, \phi) = \frac{S_p}{4\pi} \frac{1}{m!} \left( \frac{\alpha W}{\mu_p} \right)^m q_m(\gamma_p) \quad (24a)$$

$m = 1, 2, \dots$

where

$$q_m(\gamma_p) = \frac{4}{m \Delta \gamma_s^2} e^{-\frac{1}{m} (\frac{\gamma_p}{\Delta \gamma_s})^2} \quad (24b)$$

The approximation is valid for  $\Delta \gamma_s \ll \pi$ , the case considered here. Note that the functions  $q_n$  have the same general form as the forward lobe  $q$  of the phase function; but the beamwidth  $\Delta \gamma_s$  is broadened to  $\sqrt{m} \Delta \gamma_s$ .

By combining Equations (22) and (24) we obtain for  $I_1$

$$I_1(\tau; \mu, \phi) = \frac{S_p}{4\pi} e^{-\frac{\tau}{\mu_p}} \sum_{m=1}^M \frac{1}{m!} \left( \frac{\alpha W}{\mu_p} \tau \right)^m q_m(\gamma_p) \quad (25)$$

with  $\cos \gamma_p = \cos(\phi - \phi_p) [(1 - \mu_p^2)(1 - \mu_p^2)]^{1/2} + \mu_p$

$M$  is a suitably chosen upper limit. The general behavior of  $I_1$ , as expressed by Equation (25), is in accordance with expectation. For small distances into the scatter medium, the first term of the sum dominates, which means that  $I_1$  increases linearly with  $\tau$ , and its directional spectrum is narrow. ( $I_1$  is generated by forward scattering of the coherent field component in accordance with the scatter function  $q(\gamma_p)$ ).

As  $\tau$  increases,  $I_1$  reaches a maximum and then decreases again because of the exponential factor  $\exp(-\tau/\mu_p)$ . Simultaneously, higher order terms in the sum on the right side of Equation (25) become significant, which has the effect that (a) the attenuation rate is slowed down and (b) beam broadening occurs.

The reduction of the attenuation rate can be determined explicitly by considering the forward direction where  $\gamma_p = 0$ . For this direction the summation can be performed in closed form. We have

$$I_1(\tau; \mu, \phi) = \frac{S_p}{4\pi} \left\{ [e^{-\frac{\tau}{\mu_p}} e^{-\frac{\tau}{\mu_p}}] q_M(\gamma_p) \right. \\ \left. + e^{-\frac{\tau}{\mu_p}} \sum_{m=1}^M \frac{1}{m!} \left( \frac{\alpha \omega_p}{\mu_p} \right)^m [q_m(\gamma_p) - q_M(\gamma_p)] \right\} \quad (26)$$

As before, it is assumed that  $M$  is sufficiently large so that the value of  $I_1$  no longer changes when  $M$  is increased. The minimum required  $M$  will increase with  $\tau$ .

### Solution of Equation for $I_2$

Equation (19b) for  $I_2$  is the well-known transport equation for isotropic scattering. The scatter cross section per volume which appears in this equation is determined by the isotropic background of the phase function and is given by  $(1-\alpha)\sigma_S$ . This modification does not change the mathematical character of the equation.

A number of solution methods for the isotropic transport equation are available in the literature; see, for example, References [3-6]. Numerous additional references can be found in [3]. In the present paper we use a moment method approach [6] which expands the  $\mu$ -dependence of  $I_2$  into a series of overlapping triangular basis functions. These functions,  $F_n(x)$ , are defined as indicated in Fig. 5. The range  $-1 \leq \mu \leq +1$  is subdivided into  $N$  intervals

$$\mu_{n-1} \leq \mu \leq \mu_n \quad n = 1, 2, \dots, N \quad (27a)$$

where  $N$  is assumed to be odd and  $\mu_n$  is defined by

$$\mu_n = \cos \left( 1 - \frac{n}{N} \right) \pi = -\cos \left( \frac{n}{N} \pi \right), \quad n = 0, 1, 2, \dots, N \quad (27b)$$

Thus:

$$F_n(\mu) = \begin{cases} 0 & \text{for } -1 \leq \mu \leq \mu_{n-1} \\ \frac{\mu - \mu_{n-1}}{\mu_n - \mu_{n-1}} & \mu_{n-1} \leq \mu \leq \mu_n \\ \frac{\mu_{n+1} - \mu}{\mu_{n+1} - \mu_n} & \mu_n \leq \mu \leq \mu_{n+1} \\ 0 & \mu_{n+1} \leq \mu \leq 1 \end{cases} \quad (28a)$$

$n = 1, 2, \dots, N-1$

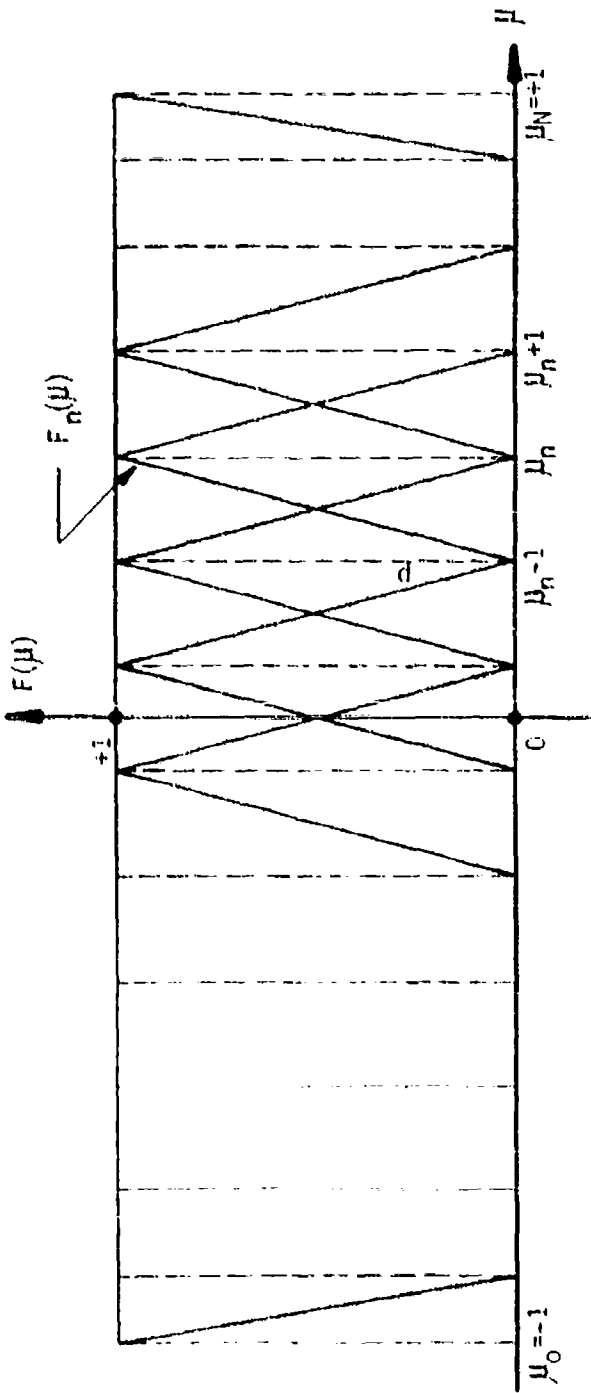


FIGURE 5: Overlapping Triangular Basis Functions for Interval  
 $-1 \leq \mu \leq +1$ .

The "boundary" functions  $F_0(\mu)$  and  $F_N(\mu)$  have the shape of half-triangles and are defined by

$$F_0(\mu) = \begin{cases} \frac{\mu_1 - \mu}{\mu_1 + 1} & \text{for } -1 \leq \mu \leq \mu_1 \\ 0 & \mu \leq \mu \leq +1 \end{cases} \quad (28b)$$

$$F_N(\mu) = \begin{cases} 0 & -1 \leq \mu \leq \mu_{N-1} \\ \frac{\mu - \mu_{N-1}}{1 - \mu_{N-1}} & \mu_{N-1} \leq \mu \leq +1 \end{cases} \quad (28c)$$

Expansion of the specific intensity  $I_2$  into the functions  $F_n(\mu)$  yields

$$I_2(\hat{\tau}, \mu) = \sum_{n=0}^N a_n(\hat{\tau}) F_n(\mu) \quad (29a)$$

where the expansion coefficients

$$a_n(\hat{\tau}) = I_2(\hat{\tau}; \mu_n) \quad 0, 1, 2, \dots, N \quad (29a)$$

are the values of  $I_2$  at  $\mu = \mu_n$ . In other words, Equation (29a) replaces  $I_2$  by a piecewise linear approximation in  $\mu$ , which is exact at the points  $\mu = \mu_n$ .

With Equation (29a), the transport equation (19b) reduces to a system of coupled differential equations of the first order in  $\hat{\tau}$

$$\mu_n \frac{da_n}{d\hat{\tau}} + a_n = \frac{\hat{W}}{2} \cdot \sum_{k=0}^N (p_k a_k) + \frac{\hat{W}}{4\pi} \cdot S_p e^{-\frac{\hat{\tau}}{\mu_j}} \quad (30a)$$

$$n = 0, 1, \dots, N$$

where

$$p_k = \int_{-1}^{+1} F_k(\mu) d\mu = \begin{cases} \frac{1}{2} (\mu_{k+1} - \mu_{k-1}) = \sin\left(\frac{\pi k}{N}\right) \sin\left(\frac{\pi k}{N}\right) & \text{for } k = 1, 2, \dots, N-1 \\ \frac{1}{2} (1 + \mu_1) = \frac{1}{2} (1 - \mu_{N-1}) = \sin^2\left(\frac{\pi}{2N}\right) & \text{for } k = 0, N \end{cases} \quad (30b)$$

We have assumed, furthermore, that the direction-cosine  $\mu_p$  of the incident plane wave coincides with one of the  $\mu_n$  values ( $n = j$ ); for normal incidence, in particular, we have  $j = N$ . Equations (30), a linear system of coupled differential equations of the first order, can be solved by assuming an exponential  $\hat{\tau}$ -dependence of  $a_n$ . It is straightforward to show that the general solution takes the form:

$$a_n(\hat{\tau}) = \frac{S_p}{2\pi} \left\{ -\frac{e^{-\frac{\hat{\tau}}{\mu_j}}}{p_j} \delta_{jn} + \sum_{k=0}^N \frac{A_k}{1 - \frac{\mu_n}{S_k}} e^{\frac{\hat{\tau}}{S_k}} \right\} \quad (31)$$

$n = 0, 1, 2, \dots, N$

$$\delta_{jn} = \begin{cases} 1 & \text{for } n = j \\ 0 & n \neq j \end{cases}$$

The first term within the parentheses is a particular solution of the inhomogeneous equation, the sum term is the general solution of the homogeneous equation. The coefficients  $A_n$  are unknown amplitudes which have to be determined from the boundary conditions. The attenuation coefficients  $S_k$  are solutions of the characteristic equation

$$\frac{\hat{W}}{2} \sum_{n=0}^N \frac{p_n}{1 - \frac{\mu_n}{S}} = 1 \quad (32)$$

which has to be solved numerically. Useful insight into the general behavior of the  $S_k$  spectrum can be gained by plotting the left side of Equation (32) as a function of  $S$ . From Equations (27b) and (30b), it can be seen that

$$\mu_{N-n} = -\mu_n, \quad p_{N-n} = p_n$$

and the left side of Equation (32),  $L(S)$ , is symmetric in  $S$ . The same is true, of course, for the right side  $R(S) = 1$ .

In Fig. 6,  $L(S)$  is sketched for  $N = 9$ . The function has  $N + 1$  poles, located at the points  $S = \mu_n$ . In the regions between adjacent poles  $L(S)$  varies from  $-\infty$  to  $+\infty$ . (The only exception is the interval between the two poles closest

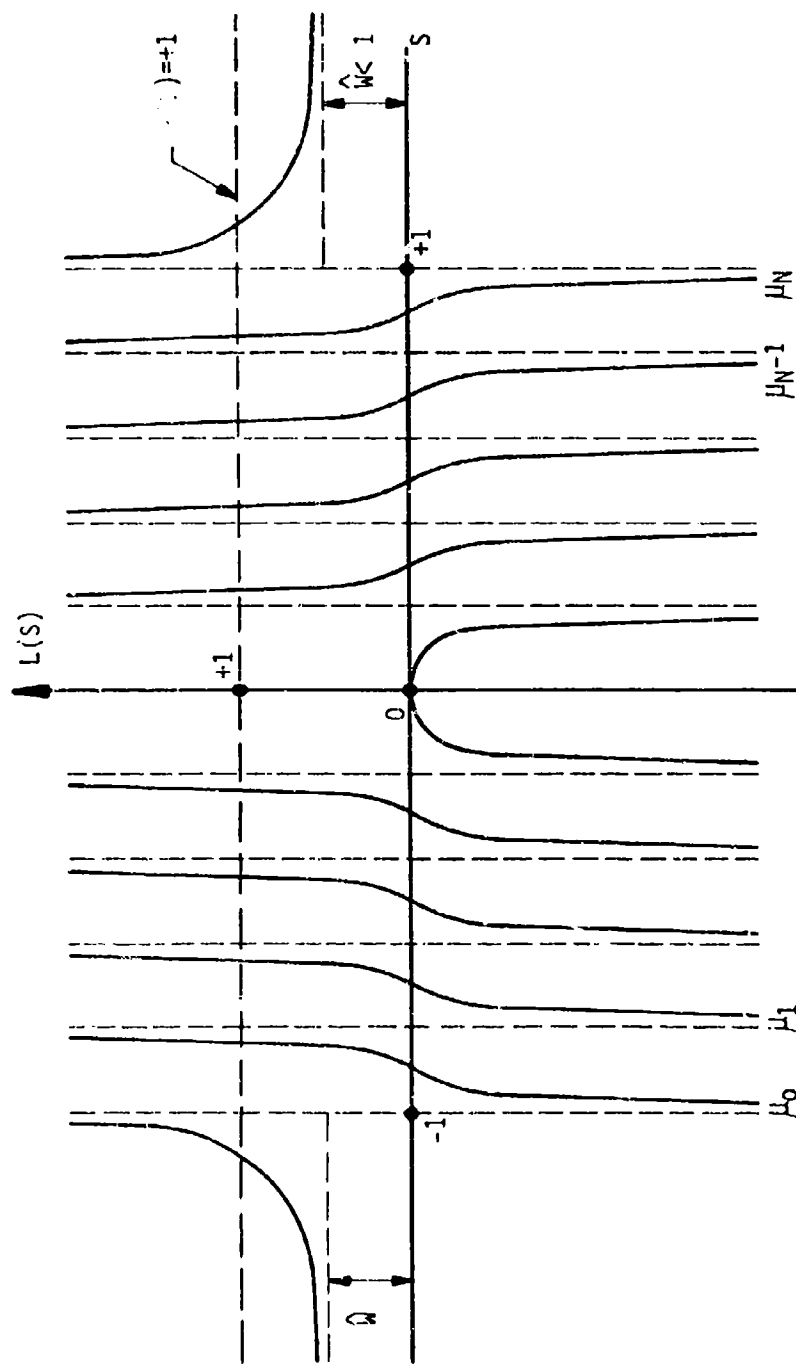


FIGURE 6: Solution of Characteristic Equation (32)

to  $S = 0$ .) Therefore,  $L(S)$  crosses  $R(S) = 1$   $N-1$  times between  $-1 \leq S \leq 1$ . Furthermore, for  $S \rightarrow \pm \infty$ , we have\*

$$L(S) + \frac{\hat{W}}{2} \sum_{n=0}^N P_n = \hat{W}$$

Since  $\hat{W} < 1$ ,  $L(S)$  intersects the line  $R(S) = +1$  twice for  $|S| > 1$ . Fig. 6 indicates the  $N+1$  solutions  $S_k$  of Equation (32) which are distributed symmetrically about the point  $S = 0$ . Counting these solutions in order of ascending value, the first  $\frac{N+1}{2}$  eigenvalues,  $S_0, \dots, S_{\frac{N-1}{2}}$ , are negative and would lead to a specific intensity which increases exponentially with  $\hat{\tau}$ . The boundary condition at  $\hat{\tau} \rightarrow \infty$  eliminates solutions of this type. The remaining  $\frac{N+1}{2}$  solutions,  $S_{\frac{N+1}{2}}, \dots, S_N$ , are positive and lead to physically meaningful results.

Fig. 6 shows that all  $S_k$  have magnitudes smaller than unity except for the largest eigenvalue  $S_N$  which is  $> 1$  and provides the lowest attenuation rate. The associated term in Equation (31) is of particular interest since it determines the asymptotic behavior of  $I_2$  at large distances into the scatter medium.

The number of eigenvalues  $S_k$  within the range  $0 \leq S \leq 1$  increases with  $N$ , the order of the approximation. For  $N \rightarrow \infty$ , the  $S_k$  form a continuous spectrum covering the entire range from 0 to 1. The eigenvalue  $S_N$ , however, remains discrete and for  $N \rightarrow \infty$  approaches a limiting value  $S_a > 1$  which will be further discussed below. Numerical evaluations have shown that if  $N$  is reasonably large (21 or greater),  $S_N$  approximates  $S_a$  closely and does not vary significantly as  $N$  is further increased.

As stated before, the boundary condition at  $\hat{\tau} \rightarrow \infty$  eliminates all expansion terms in Equation (31) associated with negative eigenvalues  $S_k$ . We have

$$A_k = 0 \quad \text{for } k = 0, 1, \dots, \frac{N-1}{2} \quad (33a)$$

The remaining amplitudes  $A_{\frac{N+1}{2}}, \dots, A_N$  are determined by the boundary condition at  $\hat{\tau} = 0$ . By applying Equation (21b) to Equations (29) and (31) the following system

---

\*From Fig. 5, it is easy to see that  $\sum_{n=0}^N F_n(\mu) = 1$  for  $-1 \leq \mu \leq +1$ .

Hence  $\sum_{n=0}^N P_n = \int_{-1}^{+1} \sum_{n=0}^N F_n(\mu) d\mu = 2$ .

of linear equations is obtained for these amplitudes:

$$\sum_{k=\frac{N+1}{2}}^N \frac{A_k}{1-\mu_n} = \frac{\delta_{jn}}{p_j} \quad \text{for } n = \frac{N+1}{2}, \dots, N \quad (33b)$$

This system has to be solved by computer. With the  $A_k$  and  $S_k$  determined, the solution for  $I_2$  takes the final form

$$I_2(\tau, \mu) = \frac{S_p}{2\pi} \left\{ -e^{-\frac{\hat{\tau}}{\mu_j}} \frac{F_j(\mu)}{p_j} + \sum_{k=\frac{N+1}{2}}^N [ A_k e^{-\frac{\hat{\tau}}{\mu_n}} \cdot \frac{F_n(\mu)}{1-\frac{\mu_n}{S_k}} ] \right\} \quad (34)$$

for  $\hat{\tau} \geq 0, -1 \leq \mu \leq +1$

$$\mu_j = \cos \theta_p = \mu_p$$

It is instructive to examine the behavior of  $I_2$  at small and very large  $\hat{\tau}$ . For small  $\hat{\tau}$ ,  $I_2$  can be approximated by

$$I_2(\hat{\tau}; \mu) \approx \frac{S_p}{4\pi} \hat{W} \cdot \begin{cases} -\frac{\hat{\tau}}{\mu_p} & -\frac{\hat{\tau}}{\mu} \\ \frac{e^{-\frac{\hat{\tau}}{\mu}} - e^{-\frac{\hat{\tau}}{\mu_p}}}{1 - \frac{\mu}{\mu_p}} & \text{for } 0 \leq \mu = \cos \theta \leq 1 \\ -\frac{\hat{\tau}}{\mu_p} \\ \frac{e^{-\frac{\hat{\tau}}{\mu}}}{1 - \frac{\mu}{\mu_p}} & -1 \leq \mu = \cos \theta \leq 0 \end{cases} \quad (35)$$

This so-called first order multiple scattering approximation is obtained if Equation (19b) is solved with the integral term on the right side suppressed [3]. Equation (35) shows that  $I_2$  is zero at the air-forest interface for  $0 \leq \theta \leq \frac{\pi}{2}$ , as required by boundary condition (21b). As  $\hat{\tau}$  is increased,  $I_2$  at first increases linearly with distance ( $I_2$  is generated by scattering of the coherent field component  $I_{ri}$  in this region) but then reaches a maximum and decreases again because of absorption in the scatter medium. At very large distances,  $I_2$  is determined by the asymptotic solution [3]:

$$I_2(\hat{\tau};\mu) = \frac{S_p}{2\pi} A_a f_a(\mu) e^{-\frac{\hat{\tau}}{S_a}} \quad \text{for } \hat{\tau} \rightarrow \infty \quad (36a)$$

$-1 \leq \mu = \cos \theta \leq +1$

where

$$f_a(\mu) = \frac{S_a - 1}{S_a - \mu} \quad (36b)$$

and  $S_a$  is determined by the equation

$$\frac{\hat{W}}{2} S_a \ln\left(\frac{S_a + 1}{S_a - 1}\right) = 1 \quad (36c)$$

The quantities  $S_a$ , and  $f_a$  are shown in Figs. 7 and 8 as functions of  $\hat{W}$ . The asymptotic amplitude  $A_a$  depends on the boundary conditions and is plotted versus  $\hat{W}$  in Fig. 9 for the conditions shown in Equation (21b). The figures show that in a strongly scattering medium with  $\hat{W}$  close to unity, the asymptotic attenuation rate  $1/S_a$  is low, the amplitude  $A_a$  is substantial, and the directional spectrum  $f_a$  is wide. Experimental results indicate that the forest environment has these characteristics and is a strongly scattering medium at mm-wave lengths. In Appendix C it is shown that the expansion term in Equation (34) associated with the largest eigenvalue  $S_N$  converges towards Equations (36) as  $N \rightarrow \infty$ .

A final remark is concerned with backscattering out of the forest medium into the air halfspace. While  $I_{ri}$  is zero and  $I_1$  is negligible in the range of the backscatter directions  $-1 \leq \mu = \cos \theta \leq 0$ ,  $I_2$  is different from zero in this range. Backscatter into the air halfspace is determined by the  $\mu$ -spectrum of  $I_2$  at  $\hat{\tau} = 0$ . With Equation (35), we have

$$I_2(0;\mu) = \frac{S_p}{4\pi} \frac{\hat{W}}{\frac{1-\mu}{\mu_p}} \quad \text{for } -1 \leq \mu = \cos \theta \leq 0$$

Apparently, side scatter ( $\theta = 90^\circ$ ) is moderately stronger than direct backscatter ( $\theta = 180^\circ$ ). Note that the backscatter radiation is generated by the (isotropic) scattering within the forest medium; but it is not caused by reflection of the incident energy at the air-to-forest interface (which is insignificant). It is a volume rather than a surface effect.

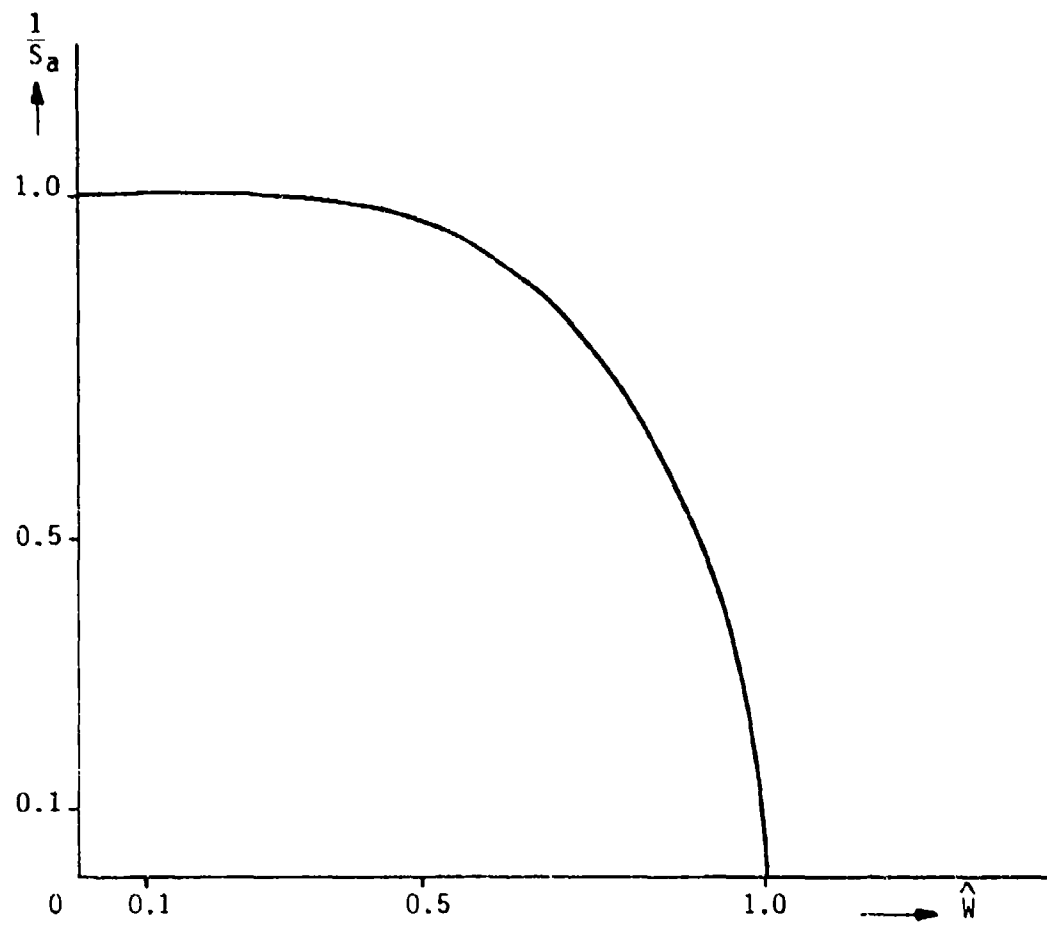


FIGURE 7: Asymptotic Eigenvalue  $S_a$  Versus  $\hat{W}$

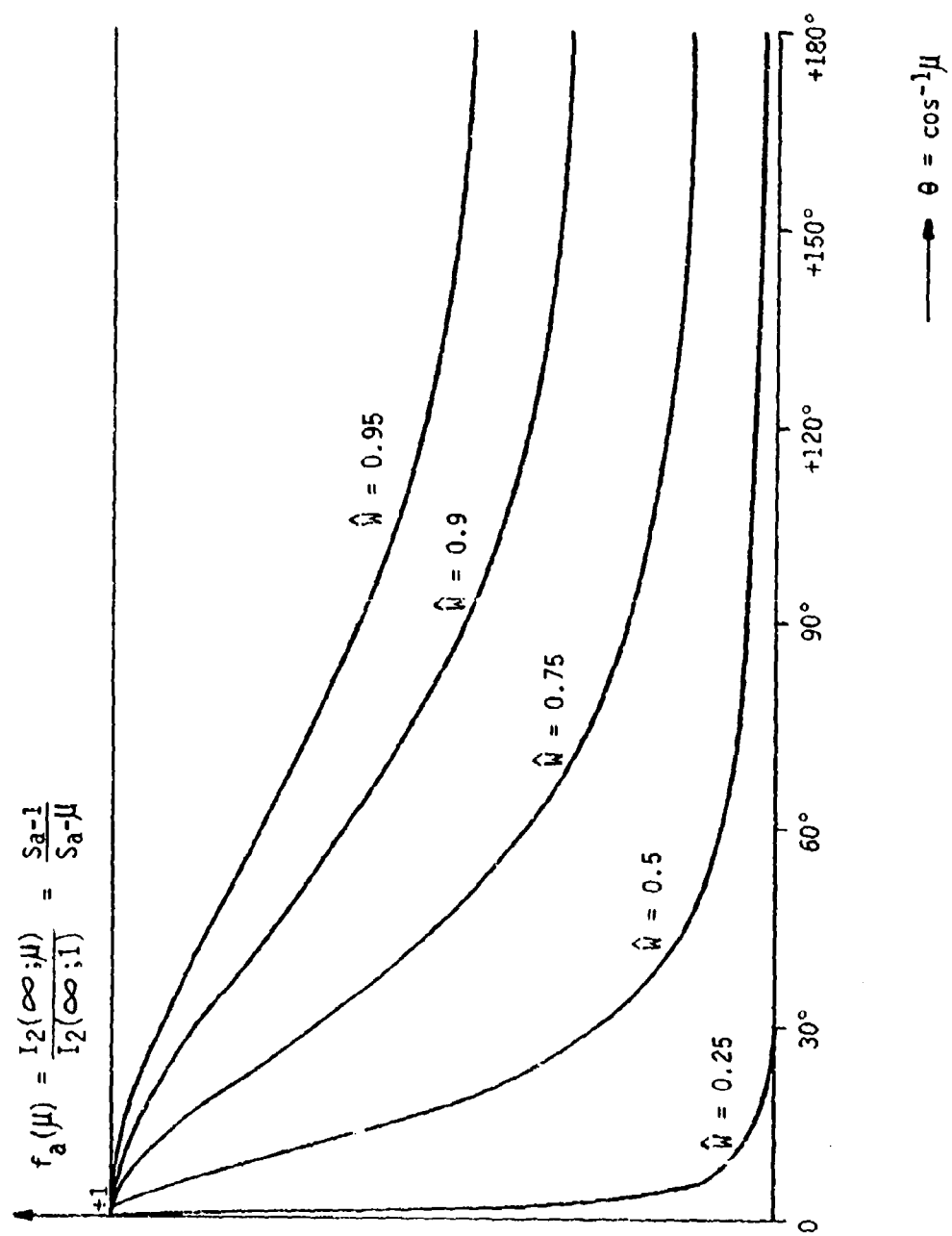


FIGURE 8: Asymptotic Directional Spectrum

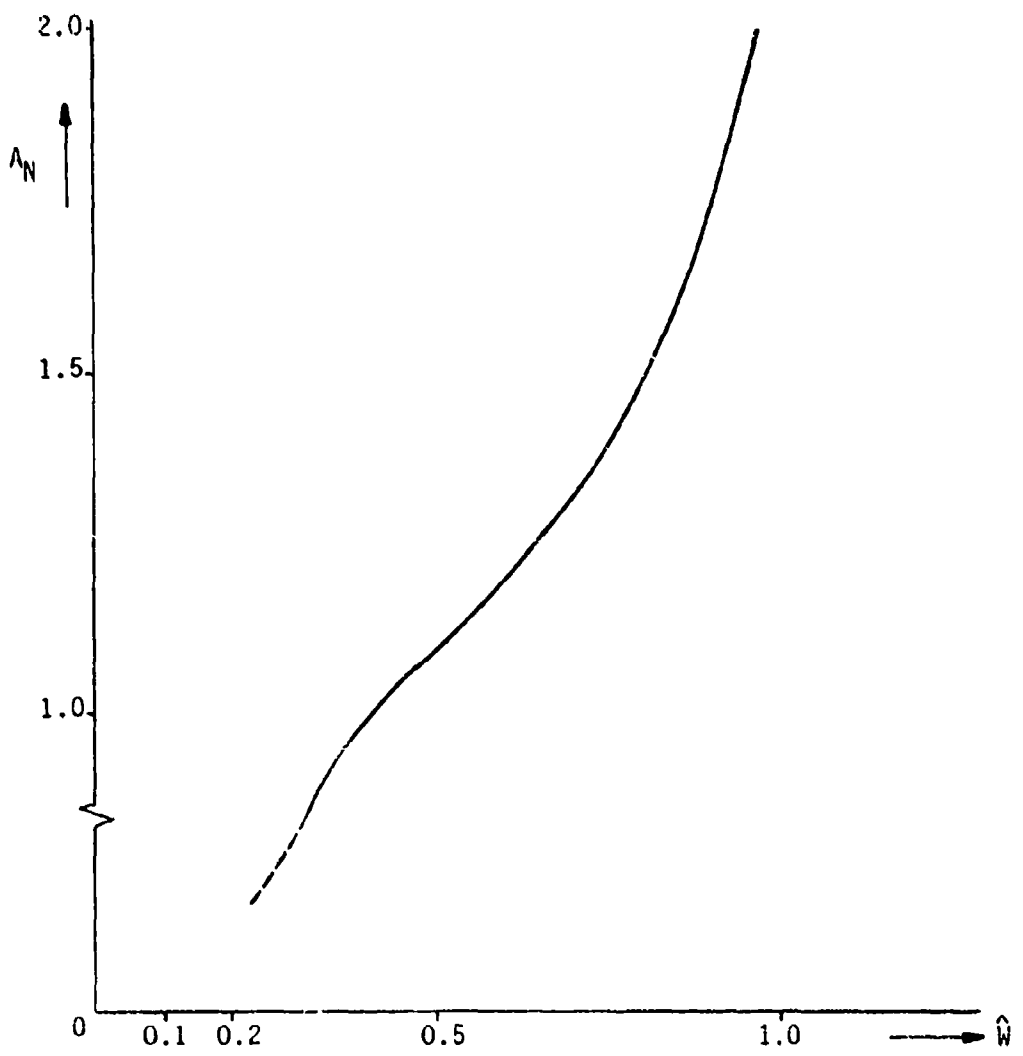


FIGURE 9: Asymptotic Amplitude  $A_a$  Versus  $\hat{W}$

#### 4. Power Received by Highly Directive Antenna

The present theory assumes that the forest halfspace is illuminated by a plane wave incident from the air halfspace. This situation can be approximated by locating the transmit antenna at a sufficiently large distance from the edge of the forest. We assume, furthermore, that the receive antenna, which is located inside the vegetated area, is a highly directive antenna of narrow beamwidth. This is in accordance with the experiments to which the theory will be compared in the next section. We characterize the receiving antenna by its power radiation pattern  $G_R(\gamma_R)$  where  $\gamma_R$  is the angle which the direction of observation  $\theta, \phi$  includes with the pointing direction of the antenna axis  $\theta_R, \phi_R$  (main beam direction); see Fig.

10. Evidently

$$\cos \gamma_R = \cos (\phi - \phi_R) \sin \theta \sin \theta_R + \cos \theta \cos \theta_R \quad (37a)$$

We normalize  $G_R$  such that

$$\int_0^{2\pi} \int_0^{\pi} G_R(\gamma_R) \sin \theta d\theta d\phi = 4\pi \quad (37b)$$

The directivity gain of the antenna is then given by  $G_R(0)$ . The power  $P_R$  received by the antenna is determined from the well-known relation  $A_{\text{eff}} = \frac{\lambda_0^2}{4\pi} G$  for the effective receiving cross section of a perfectly matched antenna of directivity  $G$ . Thus

$$P_R(\tau; \mu_R, \phi_R) = \frac{\lambda_0^2}{4\pi} \int_0^{2\pi} \int_{-1}^1 G_R(\gamma_R) I(\tau; \mu, \phi) d\mu d\phi \quad (38)$$

where  $\lambda_0$  is the wavelength. We have used here the normalized coordinates  $\tau = (\sigma_A + \sigma_S) Z$ ,  $\mu_R = \cos \theta_R$  and  $\mu = \cos \theta$ .  $P_R$ , of course, depends on the location and orientation of the antenna.

From the analytical viewpoint, it is convenient to assume a Gaussian radiation pattern

$$G_R(\gamma_R) = \left(\frac{2}{\Delta \gamma_R}\right)^2 e^{-\left(\frac{\gamma_R}{\Delta \gamma_R}\right)^2} \quad (39)$$

where  $\Delta \gamma_R$  is the beamwidth of the antenna. The receive antennas used

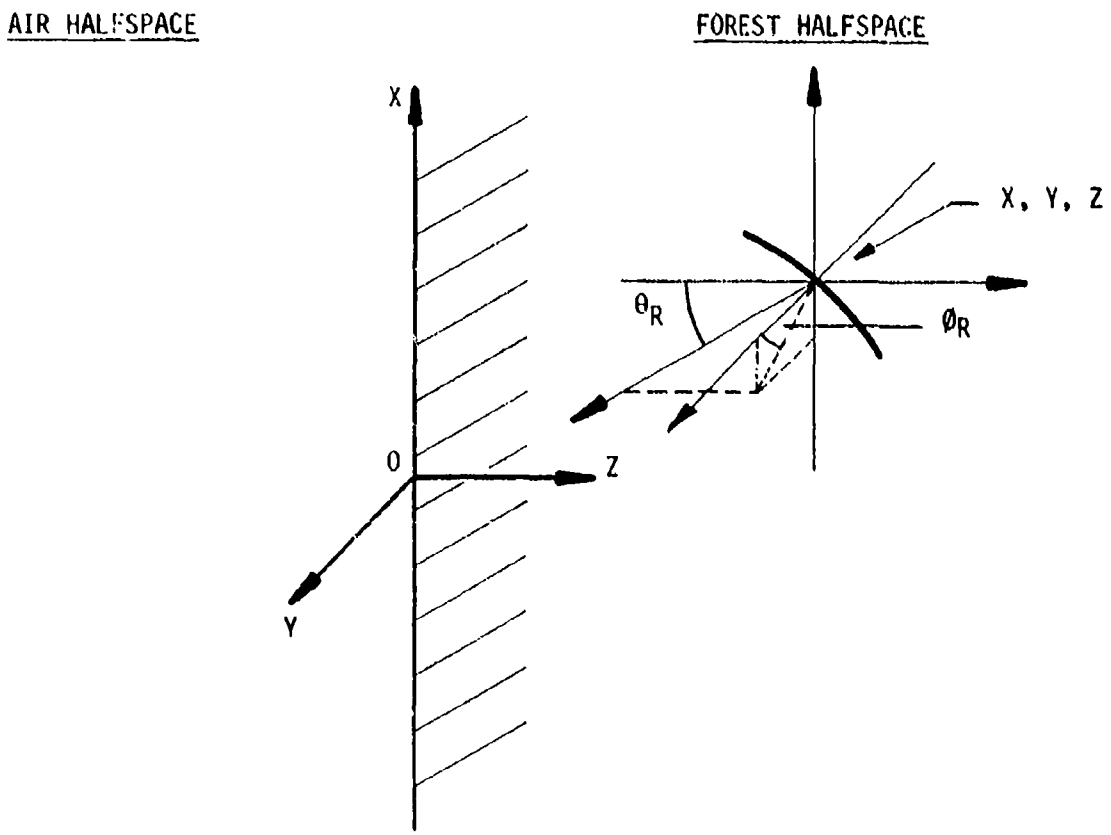


FIGURE 10: Receive Antenna in Forest Halfspace

in the experiments had a very small beamwidth of  $1.2^\circ$  and we shall assume in the numerical evaluation that the width of the forward scatter lobe of the phase function of the medium,  $\Delta\gamma_S$ , exceeds  $\Delta\gamma_R$  by a factor of 3-10. (The aperture size of the test antennas was significantly larger than the cross section of most scatter objects in a forest environment with the exception, perhaps of tree trunks.)

Using Equations (12), (26) and (34) for  $I_{ri}$  and  $I_2$ , respectively, we obtain for the received power

$$\begin{aligned} \frac{P_R(\tau; \mu_R, \phi_R)}{P_{Max}} = & \exp \left\{ -\left( \frac{\gamma_{RP}}{\Delta\gamma_R} \right)^2 - \frac{\tau}{\mu_p} \right\} \\ & + \frac{\Delta\gamma_R^2}{4} \left\{ \left[ e^{-\frac{\hat{\tau}}{\mu_p}} - e^{-\frac{\tau}{\mu_p}} \right] \bar{q}_M(\gamma_{RP}) \right. \\ & \left. + e^{-\frac{\tau}{\mu_p}} \sum_{m=1}^M \frac{1}{m!} \left( \frac{\Delta\gamma_R}{\mu_p} \right)^m [\bar{q}_m(\gamma_{PR}) - \bar{q}_M(\gamma_{PR})] \right\} \quad (40a) \\ & + \frac{\Delta\gamma_R^2}{2} \left\{ -e^{-\frac{\hat{\tau}}{\mu_p}} F_j(\mu_R) + \sum_{k=\frac{N+1}{2}}^N \left[ A_k e^{-\frac{\hat{\tau}}{S_k}} \sum_{n=0}^{N-k} \frac{F_n(\mu_R)}{1 - \frac{\mu_n}{S_k}} \right] \right\} \end{aligned}$$

$$\text{where } \bar{q}_m(\gamma_{PR}) = \frac{4}{\Delta\gamma_R^2 + m\Delta\gamma_S^2} e^{-\frac{\gamma_{PR}^2}{\Delta\gamma_R^2 + m\Delta\gamma_S^2}} \quad (40b)$$

$$\cos \gamma_{PR} = \cos(\phi_p - \phi_R) [(1 - \mu_p^2)(1 - \mu_R^2)]^{1/2} + \mu_p \mu_R \quad (40c)$$

We have normalized the received power by division with the maximum power  $P_{max}$  which is received if the antenna is placed at the forest boundary  $\tau = 0$  and is aligned with the incident radiation, i.e.,  $\theta_R = \theta_p$ ,  $\phi_R = \phi_p$ . Evidently

$$P_{max} = P_R(0; \mu_p, \phi_p) = \frac{\lambda_0^2}{4\pi} G_R(0) S_p = \frac{\lambda_0^2}{4\pi} \left( \frac{2}{\Delta\gamma_R} \right)^2 S_p.$$

The first term on the right side of Equation (40a) is the contribution of  $I_{ri}$  to the received power, the second and third terms are those due to  $I_1$  and  $I_2$ . The integrals occurring in the contribution of  $I_1$  have been evaluated by using Equation

(B.6), and the integrals in the term due to  $I_2$  were solved by regarding  $G_R$  as a  $\delta$ -function. This is justified since  $I_2$  is independent of  $\phi$  and changes very slowly with  $\mu$  as compared to  $G_R$ . The normalized variables are defined by Equations (20).

At small distances into the random medium, for  $\tau$  in the order of 3 or smaller, the coherent field component dominates and  $P_R/P_{\max}$  is in good approximation given by the first term of Equation (40):

$$\frac{P_R}{P_{\max}} = e^{-\left(\frac{\gamma_{PR}}{\gamma_R}\right)^2} \cdot e^{-\frac{\tau}{\mu_p}} = \frac{G_R(\gamma_{PR})}{G_R(0)} e^{-\frac{\tau}{\mu_p}} \quad (41)$$

In this region, the angular dependence of  $P_R$  is determined by the radiation pattern of the receiving antennas and the attenuation rate  $\tau/2 = \sigma_A + \sigma_S$  is comparatively high. Both attenuation and scatter reduce the power of coherent component.

In the range of intermediate distances ( $\tau$  in the order of 10), the forward scattered component  $I_1$  dominates and  $P_R$  is primarily determined by the second term in Equation (40). In this region, the beamwidth gradually broadens as higher and higher terms in the sum over M become significant while the attenuation rate decreases from  $\tau/2 = \sigma_A + \sigma_S$  to  $\hat{\tau}/Z = \sigma_A + (1-\alpha)\sigma_S$ .  $I_1$  is attenuated due to absorption and scattering, but scattering into the isotropic background only.

At large  $\tau$ , the received power is primarily determined by the contribution of  $I_2$ , i.e., by the last term in Equation (40). Asymptotically,  $P_R$  is with Equation (36a) given by

$$\frac{P_R}{P_{\max}} = \frac{2A_a}{G_R(0)} f_a(\mu_R) e^{-\frac{\tau}{S_a}} \quad \text{for } \tau \rightarrow \infty \quad (42)$$

$A_a$ ,  $f_a(\mu)$  and  $1/S_a$  are shown in Figs. 7 to 9 as functions of  $W$ . For large  $W$  ( $1$ ), the practically interesting case, the directional spectrum is broad and  $1/S_a$  is small so that the asymptotic attenuation rate  $\tau/(Z \cdot S_a) = (\sigma_A + (1-\alpha)\sigma_S)/S_a$  is significantly reduced from the initial value of  $\sigma_A + \sigma_S$ . The intensity  $I_2$  decreases essentially due to absorption only (though over an extended path length because of multiple scattering); but it scatters into itself.

In summary: While a mm wave beam transmitted through a forest will be highly directive and strongly attenuated at short distances, it will transform into a

radiation field of large beamwidth attenuated at a much reduced rate at large distances. These theoretical predictions are in agreement with expectation and have been confirmed by the experiments.

A similar range dependence in woods and forests, i.e., a transition from a high attenuation rate at short distances to a much lower rate at large distances has also been observed at much lower frequencies, i.e., for propagation of VHF signals through dense vegetation (jungles). The underlying mechanism, however, is completely different. The change of attenuation rate of VHF signals is attributed to the so-called up-over-down propagation mechanism where a lateral wave is excited which travels along the horizontal boundary surface between the forest canopy and the air region above it (Tamir theory). Since this wave propagates mostly in the air region, it is much less attenuated than the direct-wave traveling through the forest medium.

However, the lateral wave has a substantial launching loss. Hence, at short distances, the power transfer between two antennas located in the jungle is determined by the direct wave and the attenuation increases rapidly with antenna spacing. At large distances, on the other hand, the lateral wave will dominate and the attenuation rate is significantly reduced. Note that the effect is determined by the coherent field component alone while the incoherent component is negligible at wavelengths in the VHF region. In contrast, in the mm-wave region, the incoherent component is significant in forests, and, as explained above, will dominate at large distances. The decreasing attenuation rate is caused by the interplay between this component and the more strongly attenuated coherent component. A lateral wave supported by the canopy-to-air interface should not be expected at mm-wave length. The interface is extremely rough in the mm scale.

### III. NUMERICAL EVALUATION

A computer program for the evaluation of Equation (40) has been written. While the first and second terms of this equation (which represent the contribution of  $I_{ri}$  and  $I_1$ ) appear in explicit form, the third term contains the eigenvalues  $S_k$  and amplitudes  $A_k$  of  $I_2$ , which have to be determined by numerical solution of the characteristic Equation (32) and the linear system (33b), respectively. A null finding procedure and a matrix inversion subroutine for the solution of these equations are included in the program.

Numerical results are shown in Figs. 11 through 20. Table 1 summarizes the parameter values applying to the various curves. Throughout it is assumed that the receiving antenna has the same 3 dB beamwidth of  $1.2^\circ$  as the antenna used in the experimental study, which means that\*

$$\Delta\gamma_R = 0.7^\circ = 0.012 \text{ rad}$$

Furthermore, we assume that the 3 dB width of the forward scatter lobe of the phase function of the scatter medium is  $6^\circ$ , or

$$\Delta\gamma_S = 3.5^\circ = 0.060 \text{ rad}$$

The quantity  $Q$  appearing in the figures is the normalized received power expressed in dB, i.e.,

$$Q = 10 \lg\left(\frac{P_R}{P_{\max}}\right)$$

The distance into the forest halfspace is expressed in terms of the normalized vegetation depth  $\tau = (\sigma_A + \sigma_S)Z$  as measured from the air-to-forest interface;  $\tau$  is sometimes referred to as "optical distance."

#### Discussion

Figs. 11-13 show the range dependence of the received power, i.e.,  $Q = Q(\tau)$  for various values of  $W$  and  $\alpha$ . It is assumed here that the primary plane wave is incident normal to the air-to-forest interface (plane  $Z = 0$ ) and that the receive antenna is pointed into the direction of this wave; thus,  $\theta_p = \theta_R = 0$ . The curves demonstrate the change in attenuation rate from a high value at small  $\tau$  to a lower value at large  $\tau$ . The effect is pronounced, in particular, for strongly scattering media with  $\sigma_S \gg \sigma_A$  where the albedo  $W$  is close to unity. Increasing  $\alpha$ , the

\* $\Delta\gamma_R$  is the angle counted from the antenna axis at which the mainlobe of the power radiation pattern of the antenna is down by a factor  $1/e$ ; see Equation (39). This angle is related to the 3 dB beamwidth of the antenna by  $\Delta\gamma_R = 0.6 \Delta\gamma_{3dB}$ .  $\Delta\gamma_S$  is similarly defined.

TABLE 1. Summary of Figures 11 to 20

<u>Fig. No.</u>	<u>Incidence Angles (<math>\theta_p, \phi_p</math>)</u>	<u>Function Plotted (<math>Q=10 \log (P_R/P_{\max})</math>)</u>	<u>Parameters (<math>W, \alpha</math>)</u>	<u>Purpose</u>
11-13	$\theta_p, \phi_p = 0$	$Q = f(\tau)$ for $\theta_R, \phi_R = 0$	$W = 0.5, 0.75, 0.9, 0.95$ $\alpha = 0.2, 0.5, 0.8$	Range dependence of $P_R$ at normal incidence.
14-16	$\theta_p, \phi_p = 0$	$Q = f(\theta_R)$ for $\tau = 0, 0.1, 0.3,$ $\phi_R = 0$	$W = 0.75, 0.8, 0.95$ $\alpha = 0.5$	Directional dependence of $P_R$ at normal inci- dence.
17-18			$W = 0.9$ $\alpha = 0.2, 0.8$	
36	$\theta_p = 45^\circ, \phi_p = 0$	$Q = f(\tau)$ for $\theta_R = 45^\circ, \phi_R = 0$	$W = 0.5, 0.75, 0.9, 0.95$ $\alpha = 0.5$	Range dependence of $P_R$ at oblique incidence.
19				
20	$\theta_p = 45^\circ, \phi_p = 0$	$Q = f(\theta_R)$ for $\tau = 0, 0.1, 0.3,$ $\phi_R = 0, 180^\circ$	$W = 0.9$ $\alpha = 0.5$	Directional dependence of $P_R$ at oblique inci- dence.

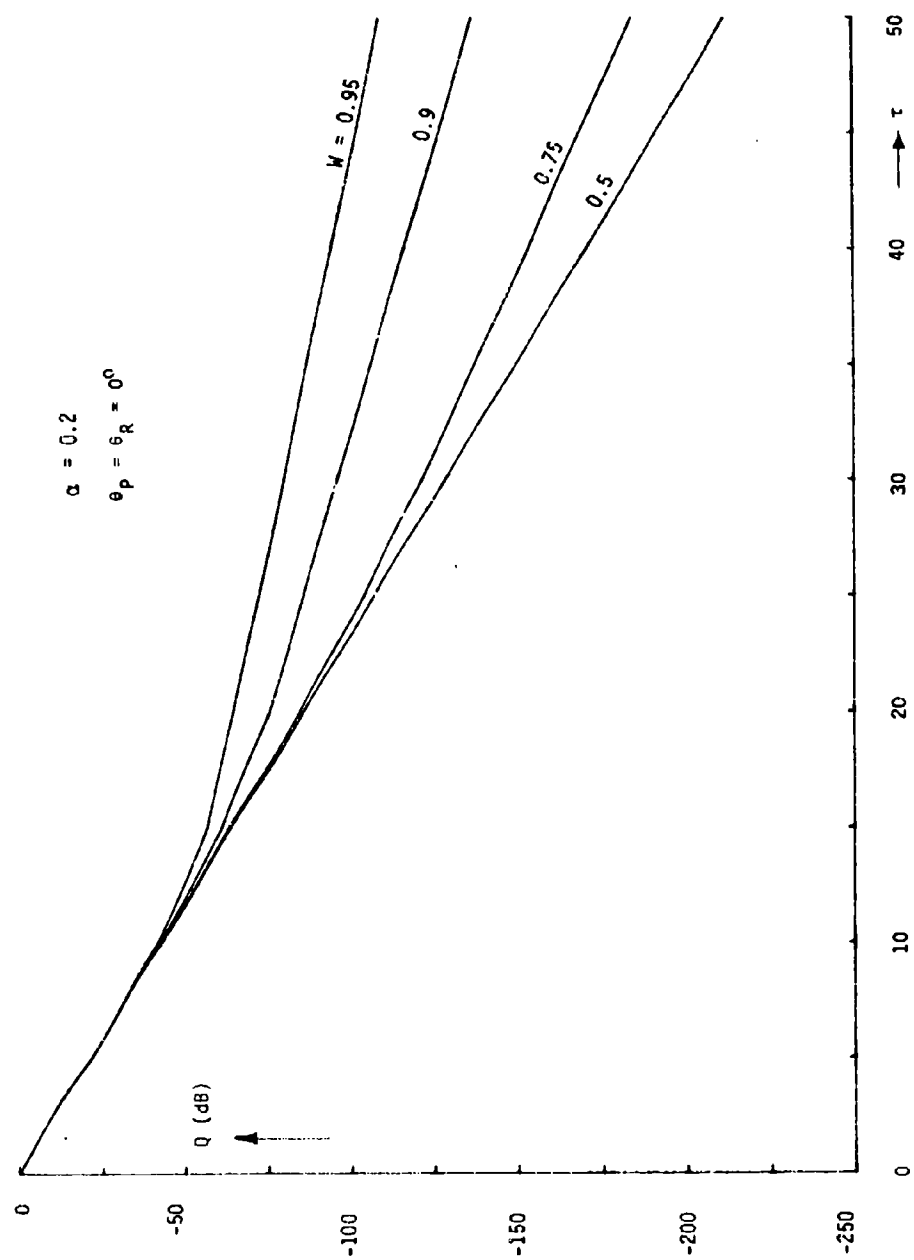


FIGURE 11: Range Dependence of Received Power for Normal Incidence and  $\alpha = 0.2$

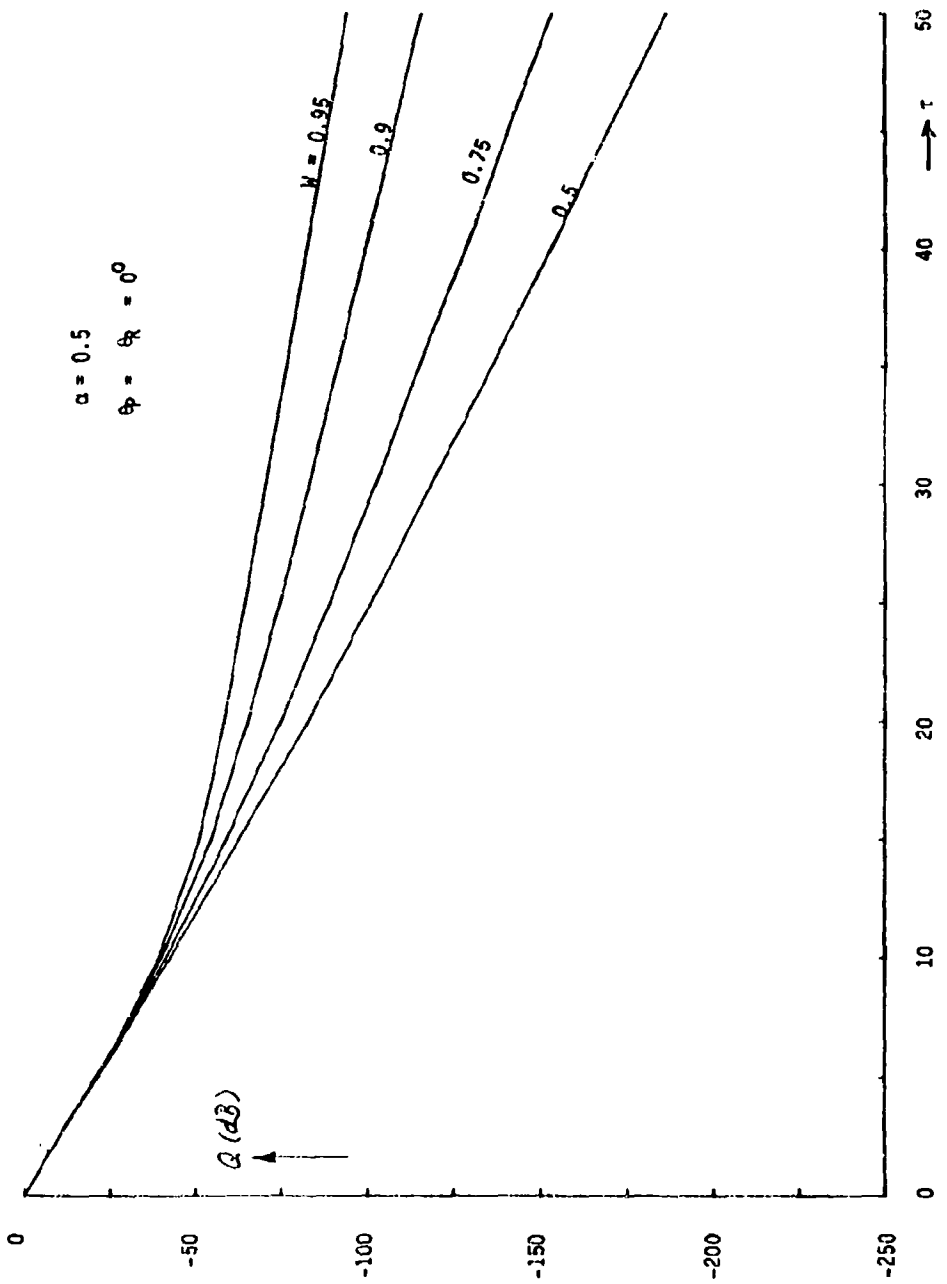


FIGURE 12: Range Dependence of Received Power for Normal Incidence and  $\alpha = 0.5$

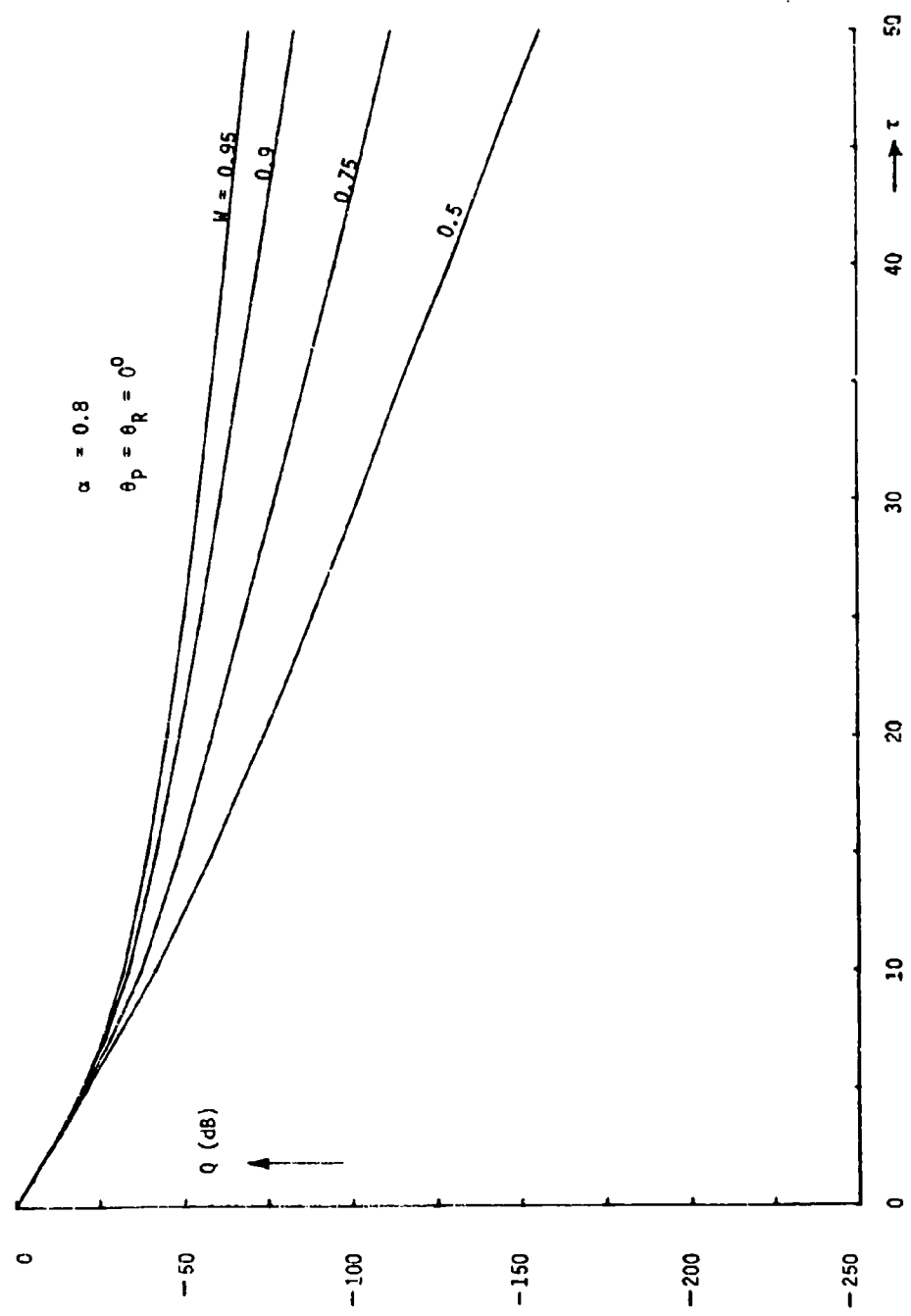


FIGURE 13: Range Dependence of Received Power for Normal Incidence and  $\alpha = 0.8$

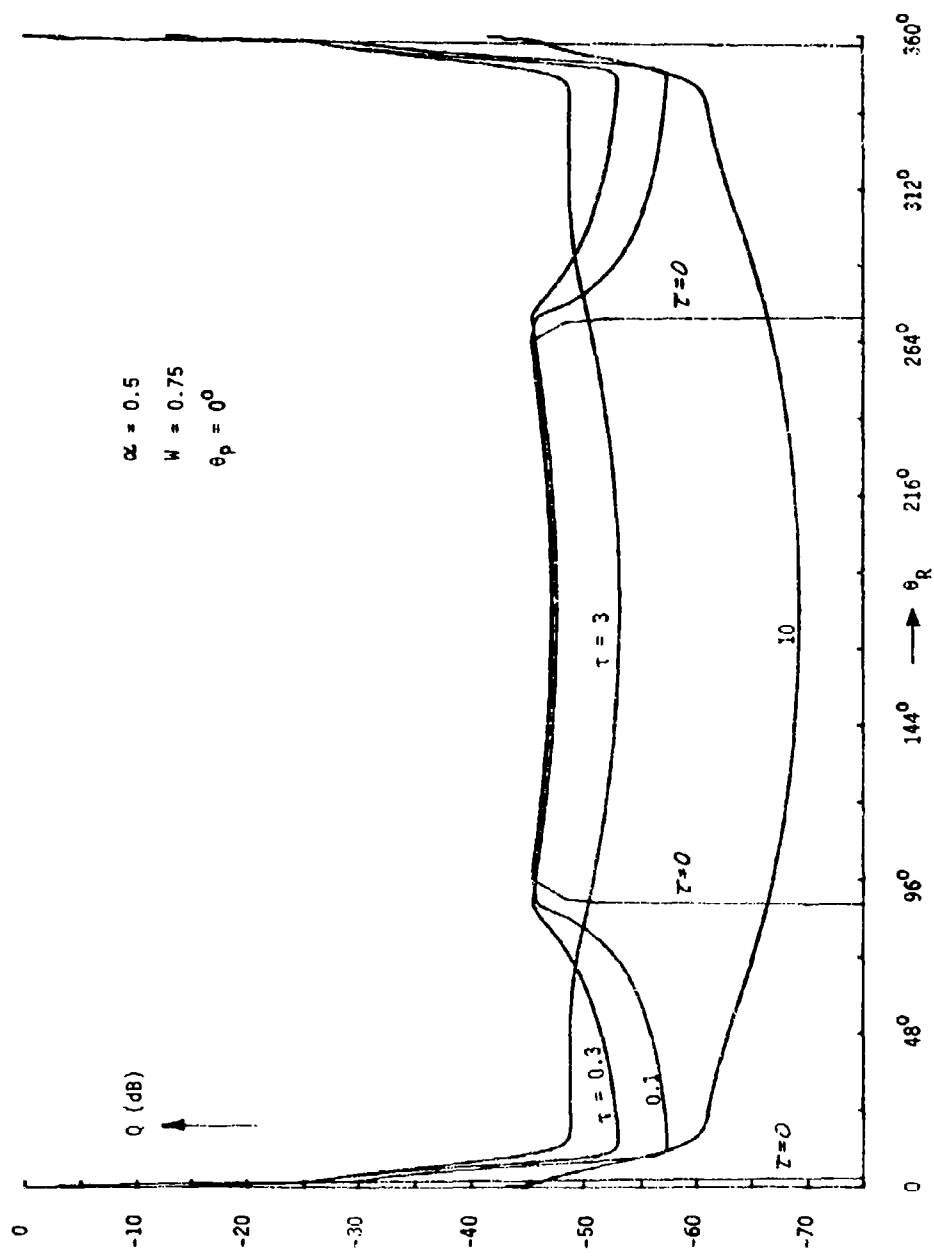


FIGURE 14a: Directional Dependence of Received power for Normal Incidence and  $\alpha = 0.5$ ,  $W = 0.75$   
 (a)  $360^\circ$  Scan

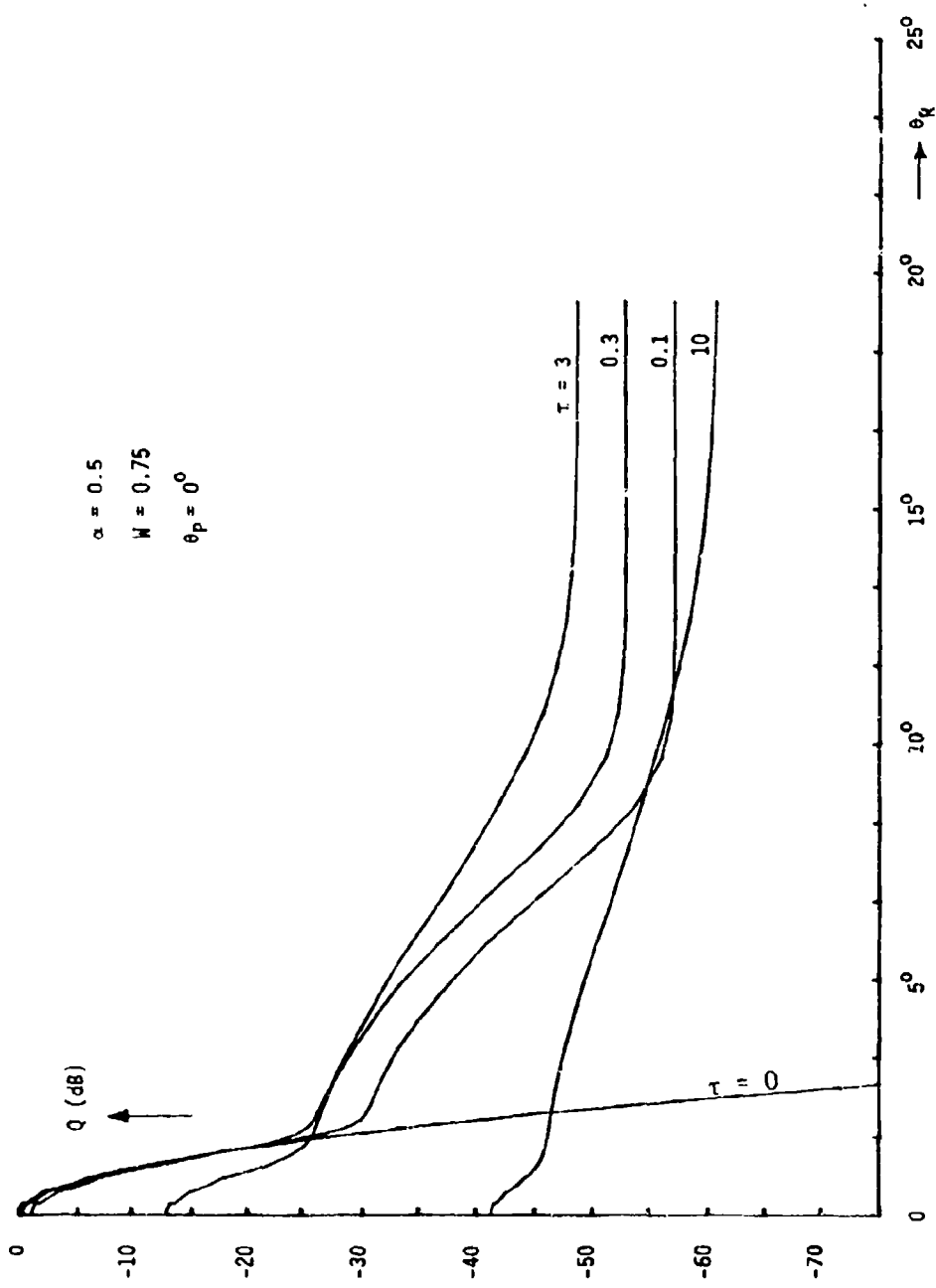


FIGURE 14b: Directional Dependence of Received power for Normal  
 Incidence and  $\alpha = 0.5$ ,  $W = 0.75$   
 (b) Expanded  $\theta$ -Scale

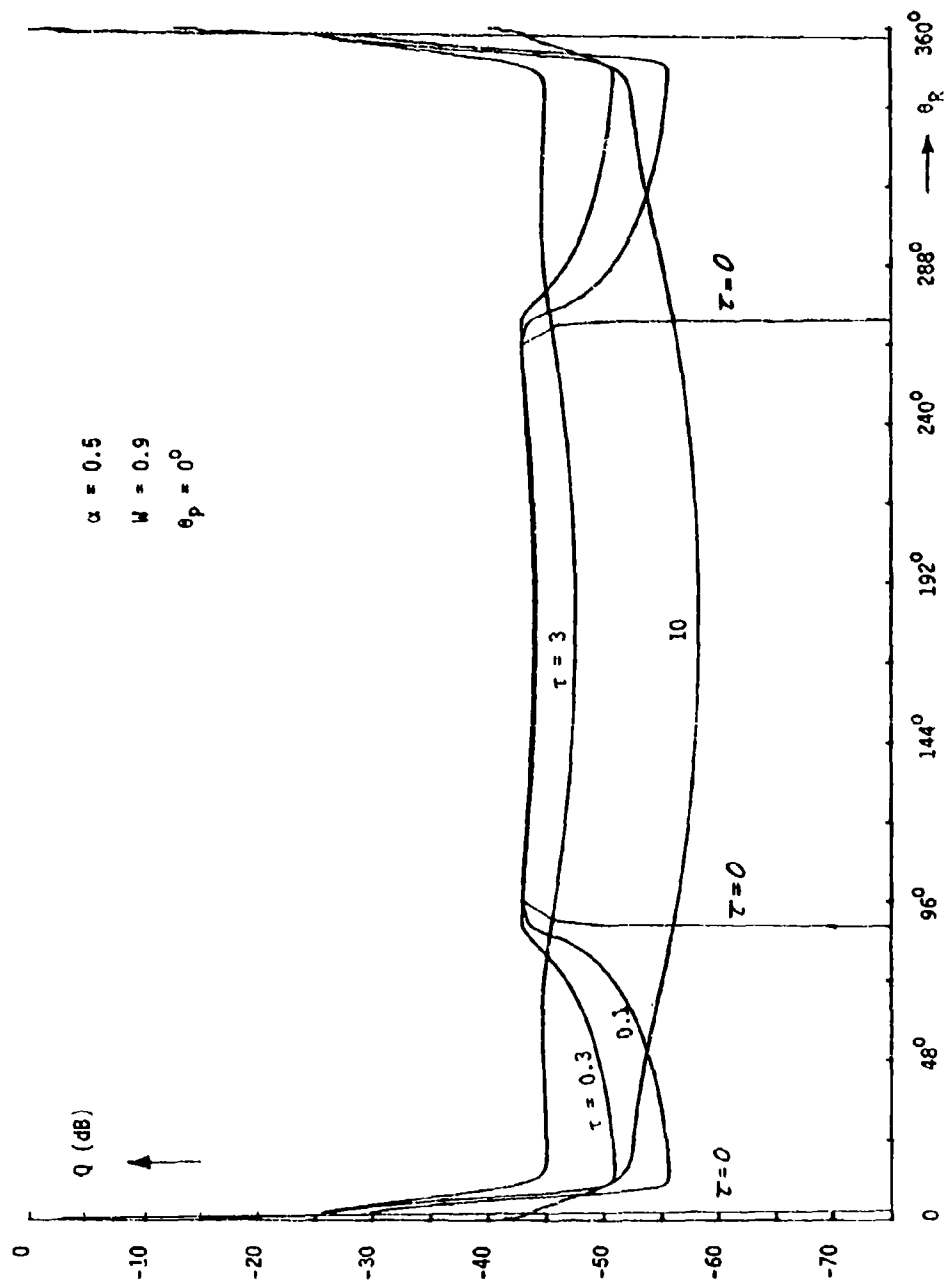


FIGURE 15: Directional Dependence of Received Power for Normal Incidence and  $\alpha = 0.5$ ,  $W = 0.9$

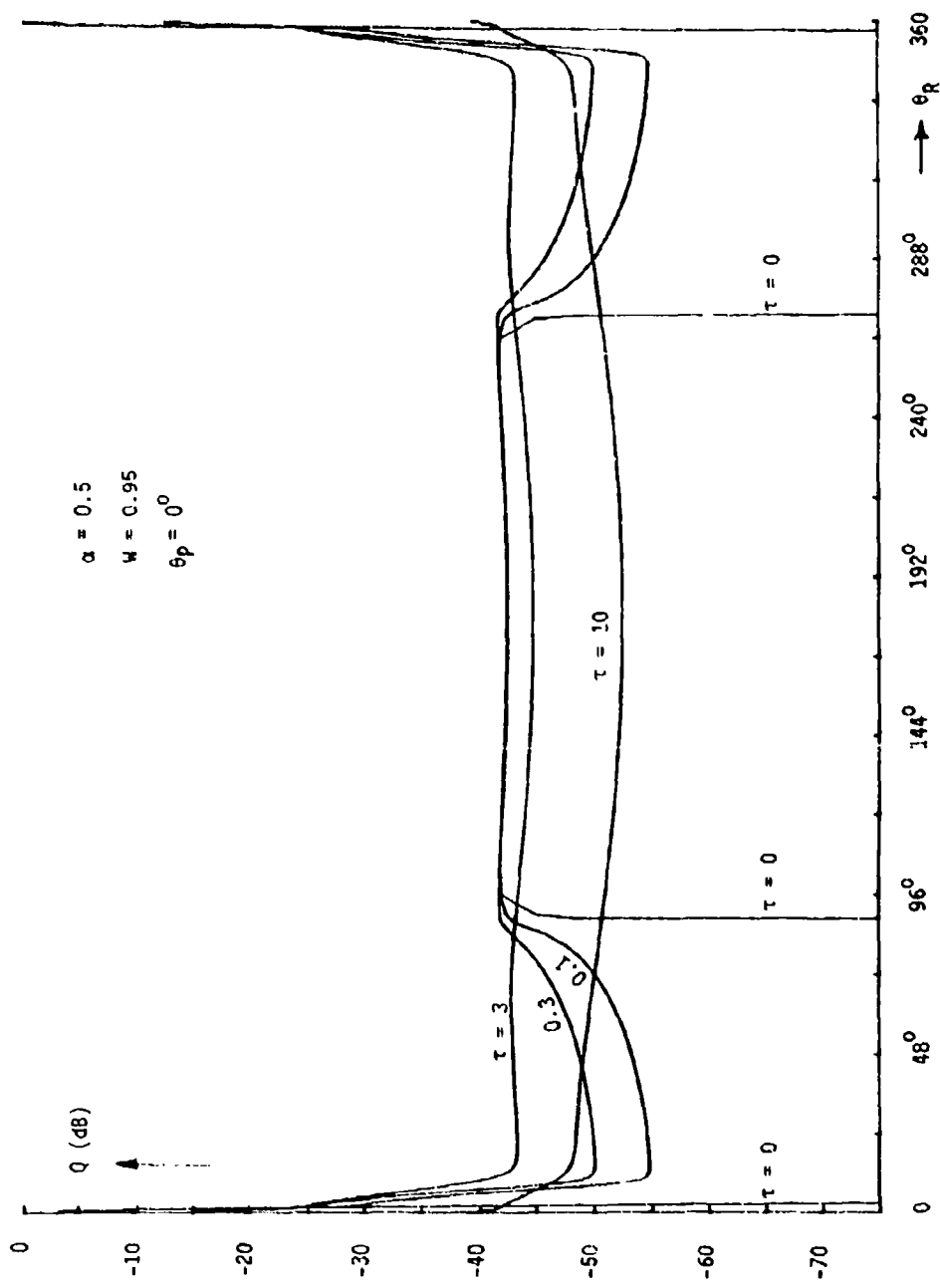


FIGURE 16a: Directional Dependence of Received Power for Normal Incidence and  $\alpha = 0.5$ ,  $W = 0.95$   
 (a)  $360^\circ$  Scan

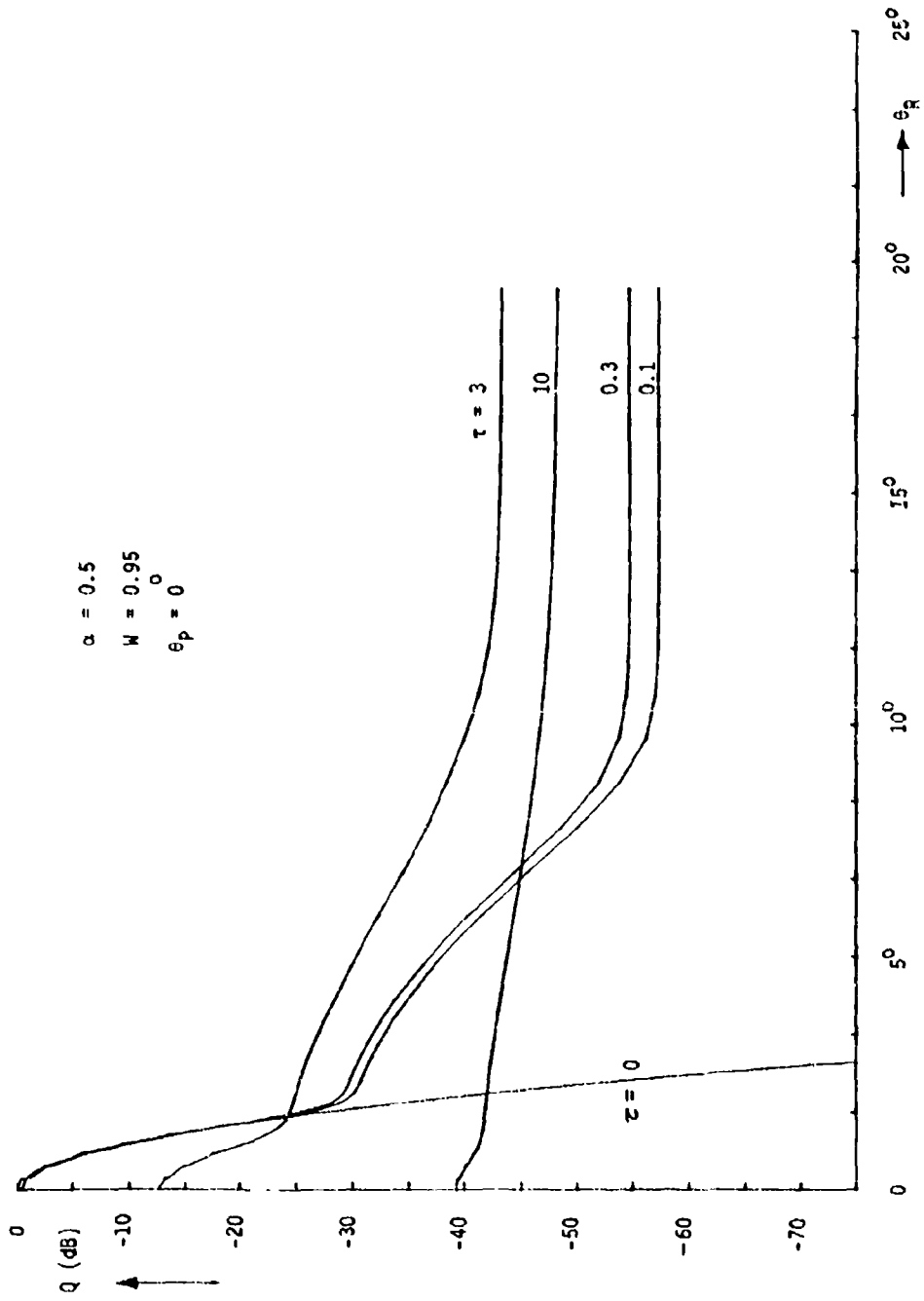


FIGURE 16b: Directional Dependence of Received Power for Normal  
 Incidence and  $\alpha = 0.5$ ,  $W = 0.95$   
 (b) Expanded  $\theta$ -scale

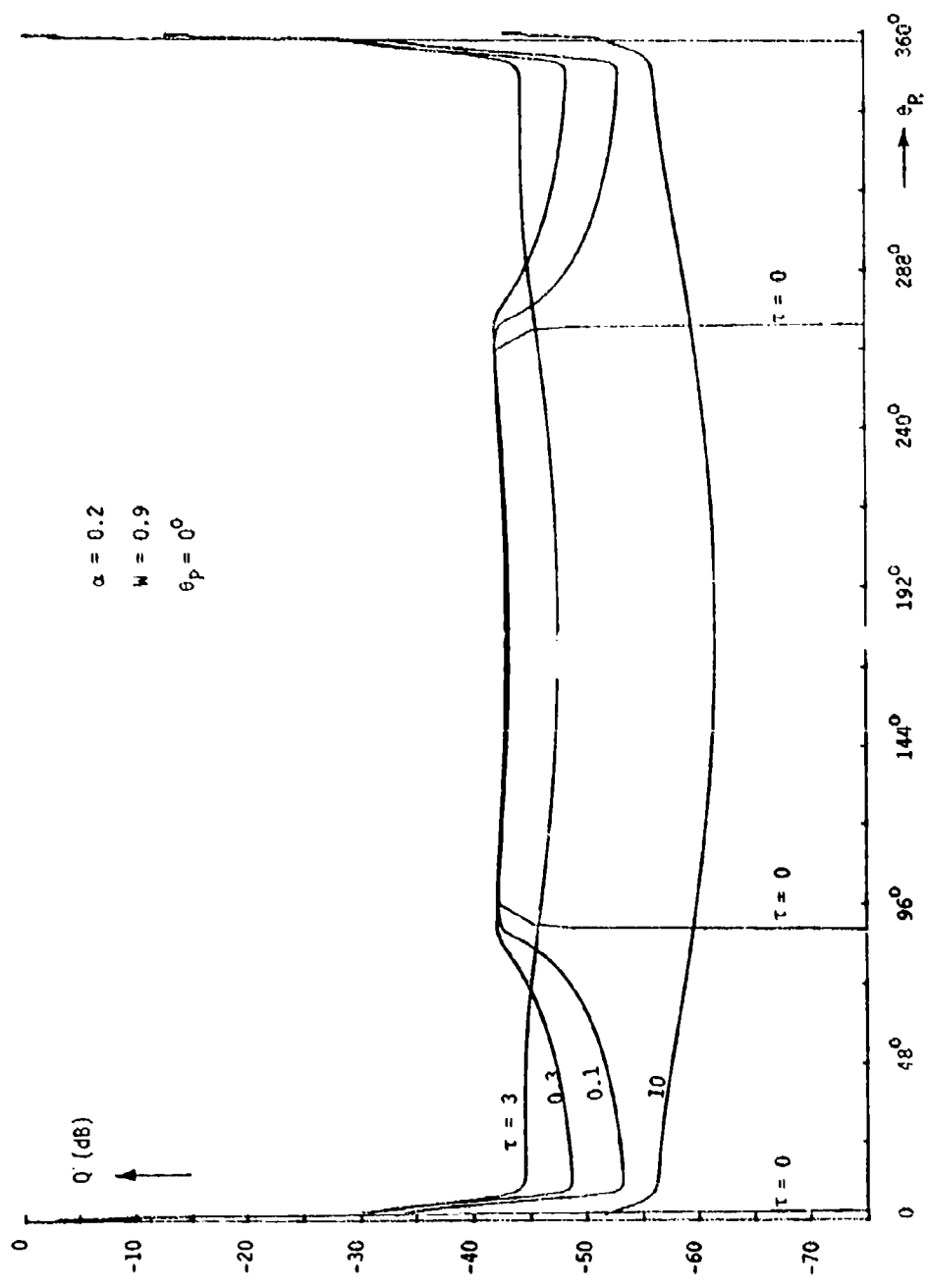


FIGURE 17: Directional Dependence of Received Power for Normal Incidence and  $\alpha = 0.2$ ,  $W = 0.9$

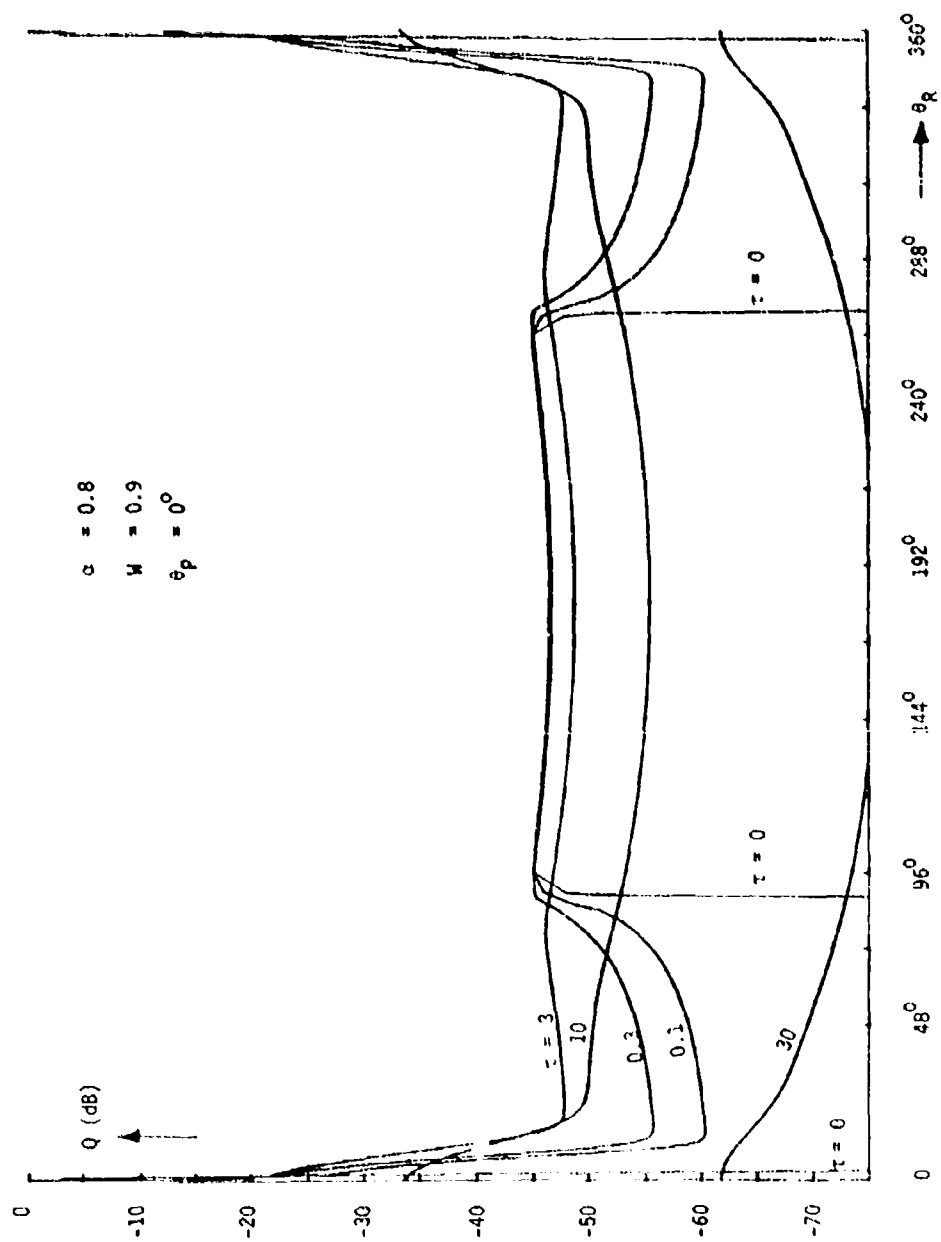


FIGURE 18a: Directional Dependence of Received Power for Normal Incidence and  $\alpha = 0.8$ ,  $W = 0.9$   
 (a) 360° Scan

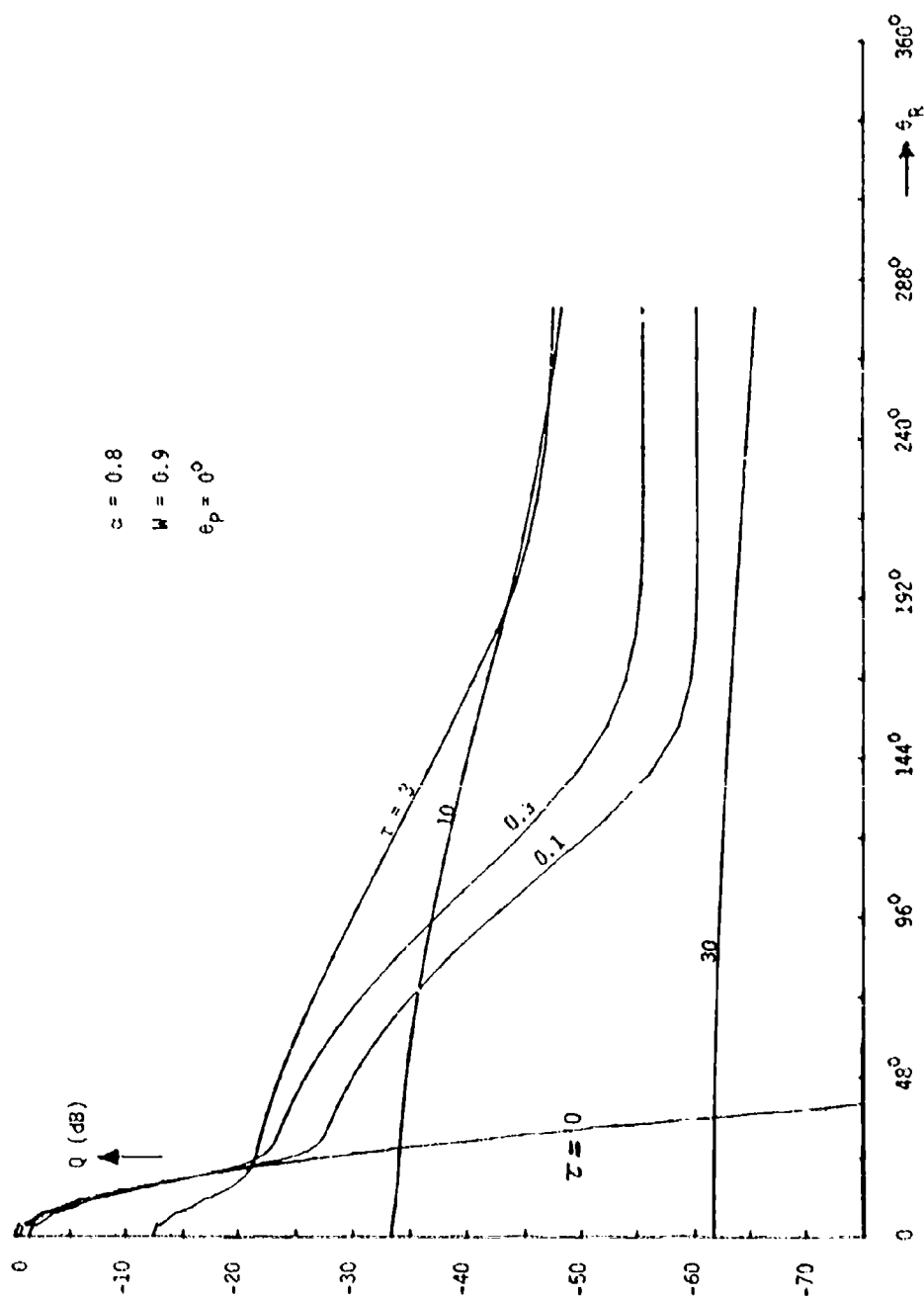


FIGURE 18b: Directional Dependence of Received Power for Normal Incidence and  $\alpha = 0.8$ ,  $W = 0.9$   
 (b) Expanded  $\theta$ -scale

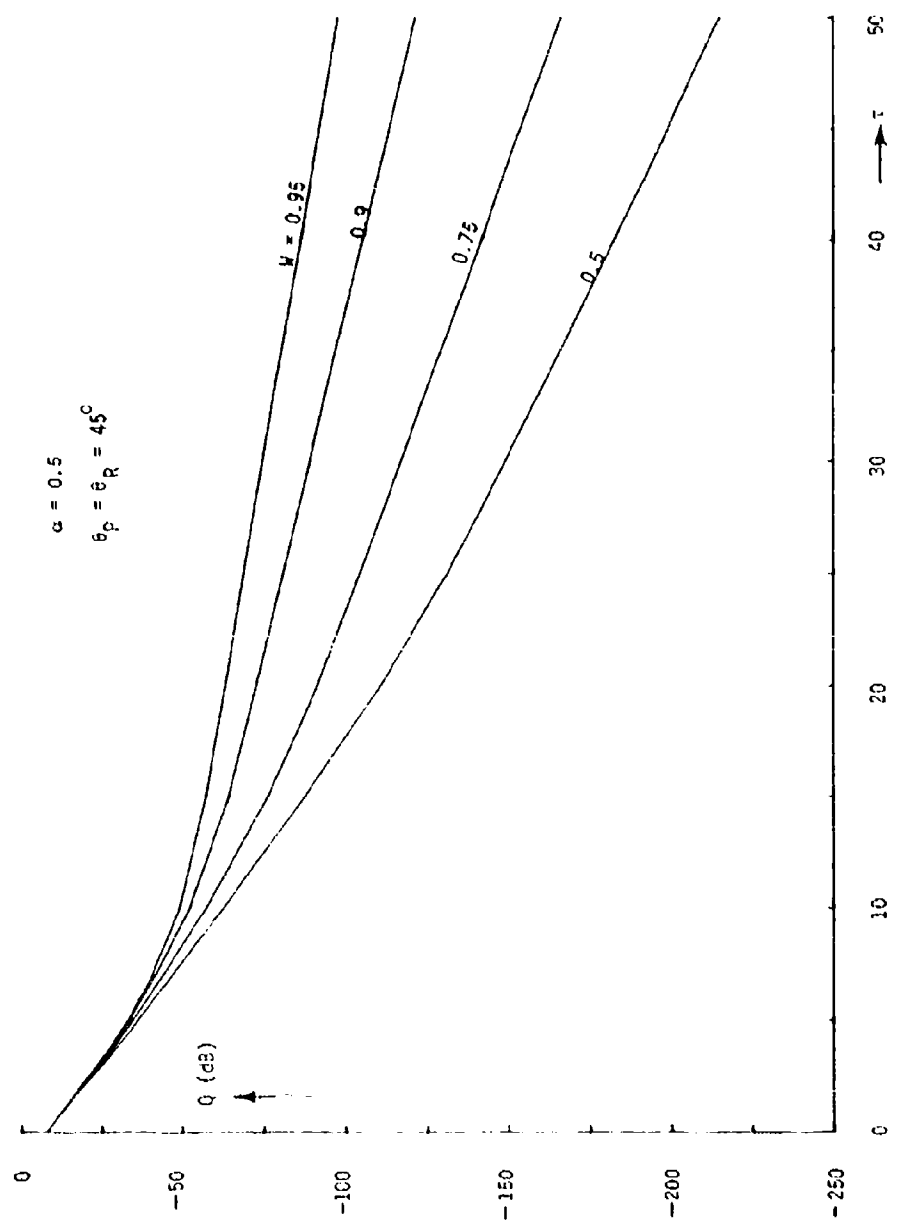


FIGURE 19: Range Dependence of Received power for Oblique Incidence and  $\alpha = 0.5$

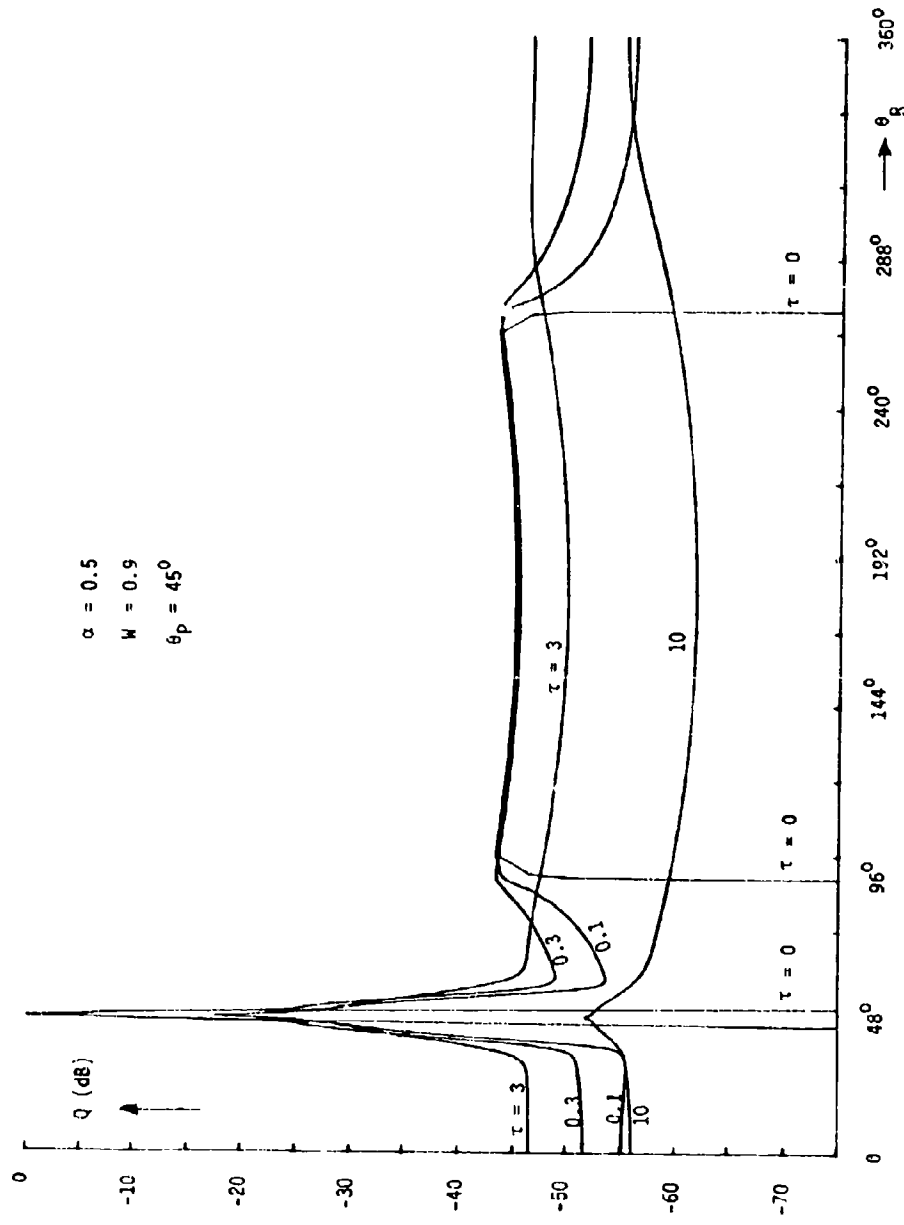


FIGURE 20: Directional Dependence of Received Power for Oblique Incidence and  $\alpha = 0.5$ ,  $W = 0.9$

ratio of the forward scattered power to the total scattered power, has a similar effect, which is easy to understand since the attenuation rates of the field intensity components  $I_1$  and  $I_2$ , which dominate at large  $\tau$ , are proportional to  $(1-\alpha W)$  in this region.

Typically, for  $W = 0.75$  and  $\alpha = 0.8$ , the coherent field component  $I_{ri}$  provides the dominant contribution to the received power in the range  $0 \leq \tau \leq 7$ , while  $I_1$  is the dominant component in the range  $7 < \tau < 50$ , and  $I_2$  in the range  $\tau > 50$ . If  $W$  is increased, i.e., for  $W = 0.95$ ,  $\alpha = 0.8$ , the changeover occurs earlier, i.e., at  $\tau = 5$  rather than 7, and 30 rather than 50.

The curves  $Q = Q(\theta_R)$  of Figs. 14 to 18 show the dependence of the received power on the pointing direction of the receiving antenna. It is assumed here that the antenna is placed at various vegetation depths  $\tau$  where it performs a full  $360^\circ$  scan. As before, it is assumed that the primary plane wave is normally incident upon the air-to-forest interface. In this case,  $Q$  depends on  $\theta_R$  only but is independent of  $\phi_R$ . Figs. 14b, 16b and 18b show  $Q(\theta_R)$  in an expanded  $\theta_R$ -scale.

For  $\tau = 0$ , when the receiving antenna is positioned in the interface plane, the curves  $Q(\theta_R)$  show the Gaussian radiation pattern of the receiving antenna. (The incident field, in this case, is an unperturbed plane wave.) This holds for the two forward quadrants  $0 \leq \theta_R \leq 90^\circ$  and  $270^\circ \leq \theta_R \leq 360^\circ$ . In the range of backward directions,  $90^\circ \leq \theta_R \leq 270^\circ$ , the antenna receives the backscatter radiation emerging from the forest. The figures show that this backscatter radiation has a rather uniform directional distribution with sidescatter moderately higher than direct backscatter, i.e.,

$$Q\left(\frac{\pi}{2}\right) = Q\left(\frac{3\pi}{2}\right) \approx Q(\pi) \quad \text{for } \tau = 0$$

As  $\tau$  is increased, beam broadening occurs. For small  $\tau = 0.1$  and 0.3, the coherent component remains dominant, as indicated by the narrow spike about  $\theta_R = 0$ . But the incoherent component produces a broad tail consisting of a peak of moderate height and width extending to about  $\theta_R = 10^\circ$ , and a very broad back scatter spectrum. The peak is determined by  $I_1$  and the background by  $I_2$ .  $I_1$  depends on  $\Delta_{YS}$ , the width of the forward lobe of the phase function; if  $\Delta_{YS}$  would be increased from  $3.5^\circ$ , the value assumed here, to  $7^\circ$ , the peak corresponding to  $I_1$  would decrease in height by 6 dB and increase in width to about  $\theta_R = 20^\circ$ . For  $\tau = 3$ , the coherent component is still clearly visible, but for  $\tau = 10$  it has all but disappeared within the incoherent component. At  $\tau = 30$ , (Fig. 18), the incoherent component has

taken over completely, the signal level has dropped significantly, and the beam has broadened out substantially.

For  $2^{\circ} < \theta_R < 90^{\circ}$ , i.e., in the range of forward directions away from the spike of the coherent component, the received power level  $Q$  first increases with  $\tau$ , up to about  $\tau = 3$ , and then decreases again. This is explained by the fact that the incoherent component, which determines the received power in this  $\theta$ -region, is generated by the scattering of the coherent component in the range of small  $\tau$ , but, after reaching a maximum, decreases again because of absorption. The maximum occurs near  $\hat{\tau} = \tau \cdot (1-\alpha W) = 1$  which roughly corresponds to  $\tau = 3$  for most of the  $\alpha$  and  $W$  values considered here.

The receiving antenna assumed here is an idealized antenna radiating a narrow mainbeam but no sidelobes. Practical antennas produce sidelobes and the measured directional spectrum  $Q(\theta_K)$  will be influenced by the sidelobe structure of the test antenna. It is likely that such distortions will obscure some of the details of the directional spectrum of  $I_1$  and  $I_2$ ; in particular, those at a level of more than 30 or 40 dB below the main peak.

Figs. 19 and 20 show the range dependence and directional spectrum of the received power for the case that the primary wave is incident under an oblique angle, i.e.,  $\theta_p = 45^{\circ}$ ,  $\phi_p = 0$ . In calculating the range dependence curves of Fig. 19, it was assumed that the receiving antenna is pointed into the direction of the incident wave such that  $\theta_R = 45^{\circ}$ ,  $\phi_R = 0$ .\* The figures show the same general behavior of  $Q$ , the normalized received power, as those for normal incidence, with the exception that in Fig. 20 the maximum of the received power occurs at  $\theta_R = 45^{\circ}$  rather than  $0^{\circ}$ . A second difference may be seen by comparison of Figs. 19 and 12, which show the range dependence of  $Q$ , at oblique and normal incidence, for the same values of  $\alpha$  and  $W$ . For  $W = 0.5$ , when absorption is strong, the attenuation rate for oblique incidence is significantly above that for normal incidence. This is due to the fact that in the case of oblique incidence the wave trains received at a given point  $\tau$  in the medium have traveled a path which, in effect, is by a factor  $(\cos \theta_p)^{-1}$  longer than in the case of normal incidence. Hence, the attenuation is that accumulated over a longer path. (Note that the receive antenna is a narrow beam antenna pointed into the direction  $\theta_R = \theta_p$  so that it receives primarily forward scattered wave trains.) The effect is clearly visible in the  $\tau$ -range where the "directive" field components  $I_{ri}$  and  $I_1$  dominate, but it levels off in the

\*The curves in Fig. 19 should start at  $Q = 0$  dB for  $\tau = 0$ . The deviation is due to a computational quantization error.

range of very large  $\tau$  where  $I_2$  is the strongest field component.  $I_2$  propagates by omnidirectional scattering and its magnitude at any point  $\tau$  is primarily determined by the constituent wave trains having traveled along the shortest paths, i.e., along those directed normally into the forest medium. (But the directional spectrum of  $I_2$  is very broad so that the received power does not depend significantly on antenna pointing.)

#### IV. EXPERIMENTS

Systematic test series on mm-wave propagation in woods and forests were conducted by Violette, Espeland, et al.\* Detailed reports on these studies have been published recently [1, 2]. The following discussion draws strongly from these reports.

##### 1. Description of Experiments

The experiments were conducted at three frequencies simultaneously, i.e., at 9.6, 28.8 and 57.6 GHz. The first of these frequencies is at X-band; the two remaining frequencies are close to the 35 and 60 GHz bands which are primarily of interest in tactical communication. The transmit antennas have a comparatively broad beamwidth of  $10^{\circ}$  and provide wide angle illumination of the test area. The receiving antennas have narrow beamwidth, i.e.,  $4^{\circ}$  at X-band and  $1.2^{\circ}$  at the two mm-wave frequencies. In the numerical evaluation of the theory, the  $1.2^{\circ}$  beamwidth was assumed for the receive antenna.

The antennas are linearly polarized and in the experiments of interest here were operated in co-polarization. The experiments have shown that at mm-wave frequencies, the propagation conditions in vegetation are practically the same for vertical and horizontal polarization so that the direction of polarization is of no consequence. This was also assumed in the theory. There is, however, the following difference. The theory is based on the scalar transport equation which means that the received power is obtained as the total power intercepted from both the co-polarized and cross-polarized field components. In the experiments, which utilize linearly polarized antennas, only the copolarized component contributes to the received power. Cross-polarization experiments have shown, however, that over the distances considered here, mm-wave beams do not become fully depolarized in vegetation and that the cross-polarized component remains several dB below the copolarized component. Hence, errors due to this discrepancy of theory and experiments should not exceed 1-2 dB.

\*The investigators are with NTIA/ITS, US Dept. of Commerce, Boulder, CO. The experiments were performed under contract with the US Army Communications-Electronics Command, Fort Monmouth, NJ.

Normally, the vegetation density in a forest will change strongly with location and is difficult to characterize. To eliminate this uncertainty, the experiments were conducted in a regularly planted, well-groomed orchard of pecan trees (near Wichita Falls, TX) which should approximate a statistically homogeneous vegetation medium - as far as this is possible. The trees in this orchard were of roughly equal growth they were planted in a regular square pattern spaced about 13 m apart, and individual trees had a height of approximately 10 m. Maximum vegetation density occurred in the canopy region between 4 and 6 m above ground. The experiments were conducted both under summer and winter conditions, i.e., with trees in leaf and without leaves. Fig. 21 shows the test site in early April and late August when the experiments were conducted.

The experiments which are of interest in the context of the present paper can be described with the help of Fig. 22. The black circles in this figure indicate some of the trees. The transmit antenna was located at or near the point  $T_{3A}$  outside the orchard at a distance of ~300 m from the first row of trees. The receive antenna was located within the orchard and was moved to various locations  $R_3$ ,  $R_4$ ,  $R_5$ , etc., as indicated in the figure. In each case, the receive antenna was positioned at the same height as the transmit antenna, and the line-of-sight followed a path of maximum vegetation density through one column of trees. The measurements were taken at three different heights above ground, i.e., at 1 m, 4 m, and 6 m. The 4 and 6 m experiments are primarily of interest here. At each receiver position and height, the receive antenna was first pointed towards the transmit antenna so that its main beam direction coincided with the line-of-sight. The receive antenna then performed a scan in azimuth by  $\pm 15^\circ$  and in elevation by  $\pm 10^\circ$ . The quantity measured was the received power at constant transmit power.

## 2. Experimental Results

Results applicable to this paper are shown in Figs. 23 to 26. In the first two figures, the range dependence of the received power is plotted. The quantity shown is the maximum of the received power observed during the azimuth and elevation scans. The power is normalized to 0 dB at the edge of the orchard. Furthermore, free-space path losses ( $R^{-2}$  dependence) and atmospheric attenuation (at 57.6 GHz) have been subtracted so that the curves show the vegetation loss only. Because of this normalization, comparison with the theoretical results based on the assumption of an incident plane wave seems appropriate. The abscissa scale shows the number of trees on the line-of-sight; this number multiplied by the tree spacing of 13 m yields the vegetation depth in meters. The solid curves



(b) Trees in Leaf  
(August)



(a) Trees Without Leaves  
(April)

FIGURE 21: Photographs of Test Site Used for Vegetation Experiments  
(From Violette and Espeland [2])

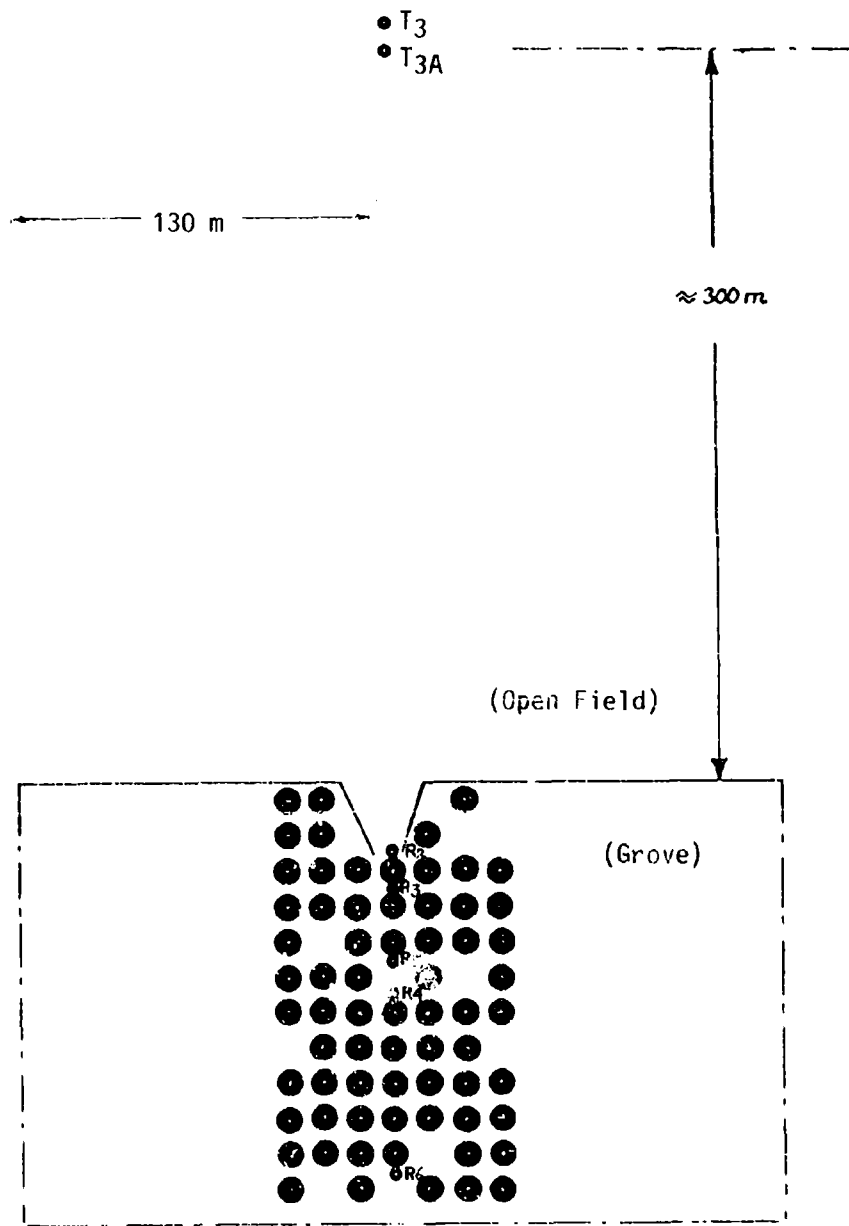


FIGURE 22: Drawing of Test Area

The black circles show some of the trees. In the experiments of interest here, the transmitter terminal was located outside the orchard at point T3A. The receiver terminal was positioned inside the orchard; receiver locations are indicated by R<sub>2</sub>, R<sub>3</sub>, etc.

(From Violette and Espeland [2].)

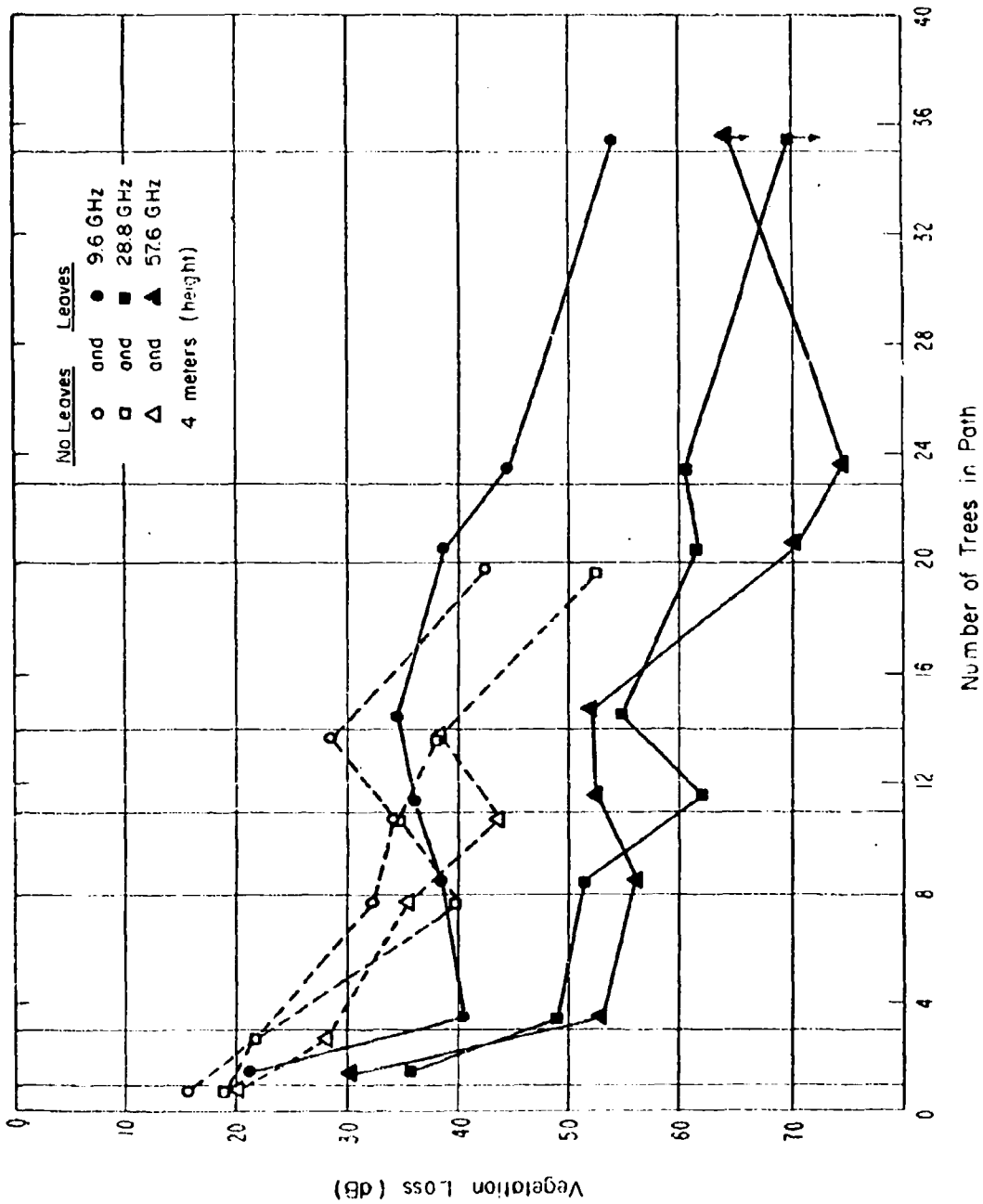


FIGURE 23: Received Power in dB (Vegetation Loss) as Function of Number of Trees in Path.

The line-of-sight (LOS) followed a maximum vegetation density path at a height of 4 m above ground. The trees are spaced  $\approx$ 13 m apart.

Solid Lines: Vegetation loss for trees in leaf.

Dashed Curves: Vegetation loss for trees without leaves.

(From Violette and Espeland [2].)

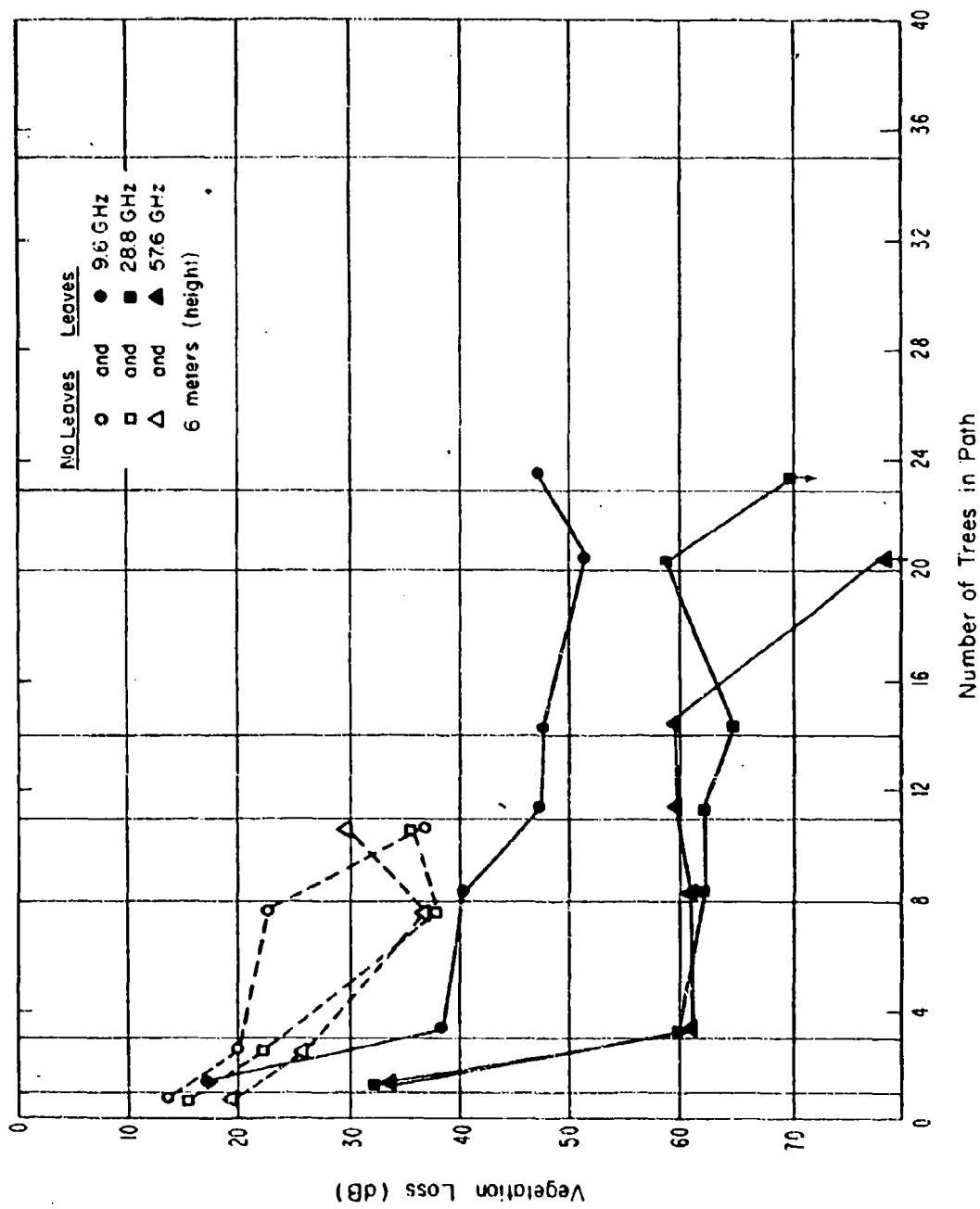


FIGURE 24: Received Power in dB (Vegetation Loss) as Function of Number of Trees in Path

Height above ground: 6 m. Other conditions are those of Figure 23.  
 (From Violette and Espeland [2].)

show the summer data, the dashed curves the winter data. Apparently, leaves have a strong effect on mm-wave attenuation. As one should expect, the attenuation increases with frequency though the effect is not dramatic in the mm-wave region. It is evident that the experimental results confirm the theoretical prediction that the mm-wave attenuation rate in woods decreases from a high value at small vegetation depths to a much smaller value at large depth; the transition between these two regions appears to be rather sharp.

Figs. 25 and 26 show the received power as a function of the azimuth and elevation scan angles. The light traces indicate the power received in free space, i.e., the radiation pattern of the receive antenna. The figures apply to trees without leaves, but very similar curves were recorded for trees with leaves. Again, good qualitative agreement with theoretical predictions is observed. For short distances into the orchard, i.e., at vegetation depths of one and three trees, the presence of the coherent component is evident by the narrow peak of the scan pattern. At larger vegetation depths, corresponding to propagation paths through eight and eleven trees, the coherent component has disappeared within the incoherent component which dominates the received power, resulting in a reduced amplitude and substantial beam broadening.

The scintillations in the curves of Figs. 25 and 26 are interference effects (fadings); the exact locations of the maxima and minima should vary rapidly with antenna position so that, in an averaged curve, these fluctuations will disappear. Since transport theory neglects interference effects, the corresponding theoretical curves of Figs. 14 to 18 are smooth.

### 3. Comparison of Theory and Experiments

Theoretical and experimental results show the same general trends and are in good qualitative agreement. One may now try to establish quantitative agreement by choosing the numerical values of the four theoretical parameters  $\Lambda_{YS}$ ,  $\sigma_A$ ,  $\sigma_S$  and  $\alpha$ , such that a "best fit" of the calculated curves to the measured curves is achieved. At the same time, this procedure would yield order of magnitude estimates for the four parameters. The procedure, however, is not without difficulties and, as will become apparent from the discussion below, the presently available experimental data base is not sufficiently large to arrive at definite conclusions. It should be understood, also, that the comparison of theory and experiments involves a certain amount of conjecturing since the measured curves, as opposed to the smooth theoretical curves, show a significant amount of fluctuation. Moreover,

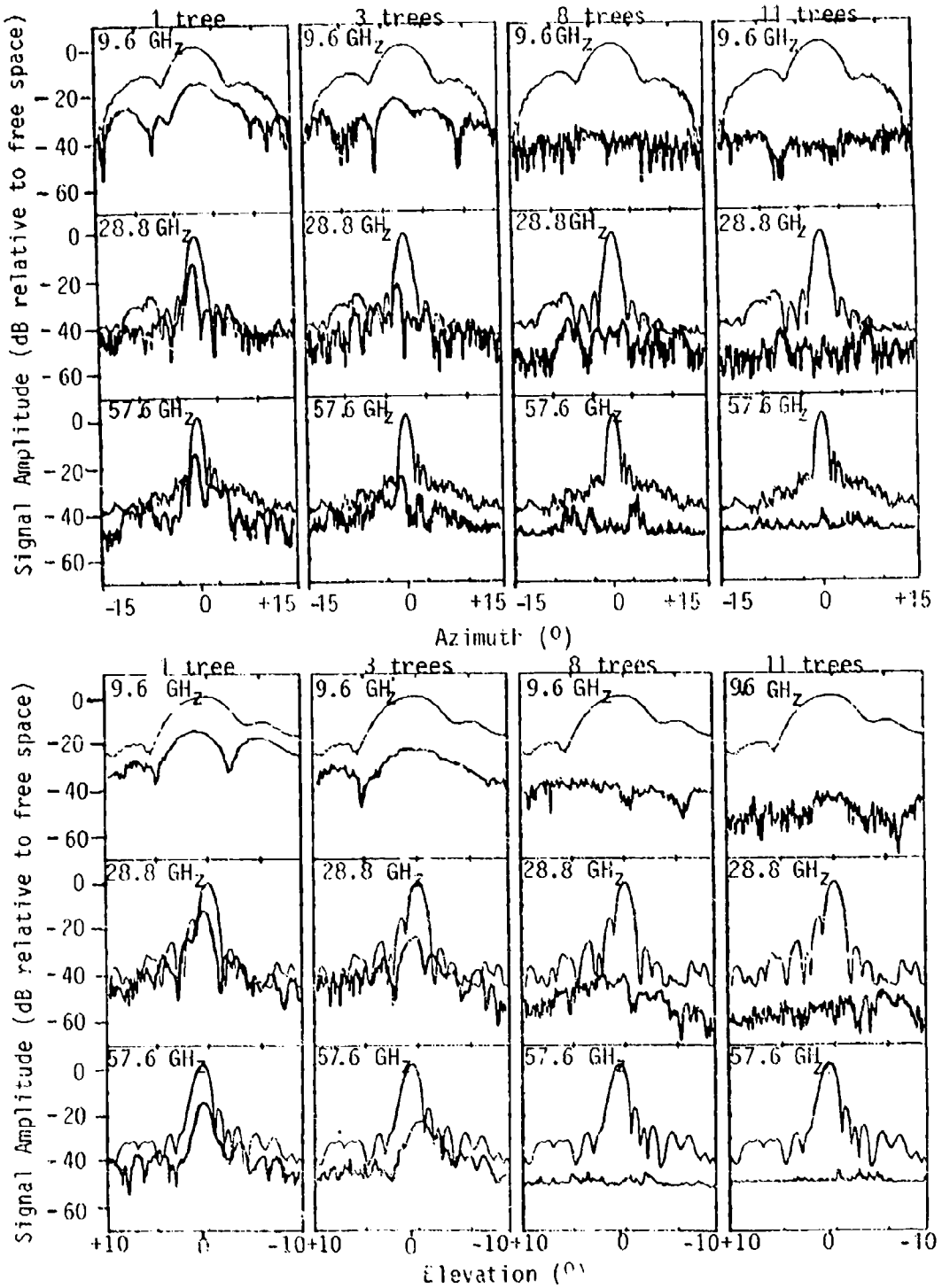


FIGURE 25: Directional Dependence of Received Power at Height of 4 m with 1, 3, 8 and 11 Trees in Path.

The scan range in azimuth is  $\pm 15^\circ$ , in elevation  $\pm 10^\circ$ ; the curves apply to trees without leaves. The light traces show the radiation patterns of the receive antennas.

(From Violette and Espeland [2].)

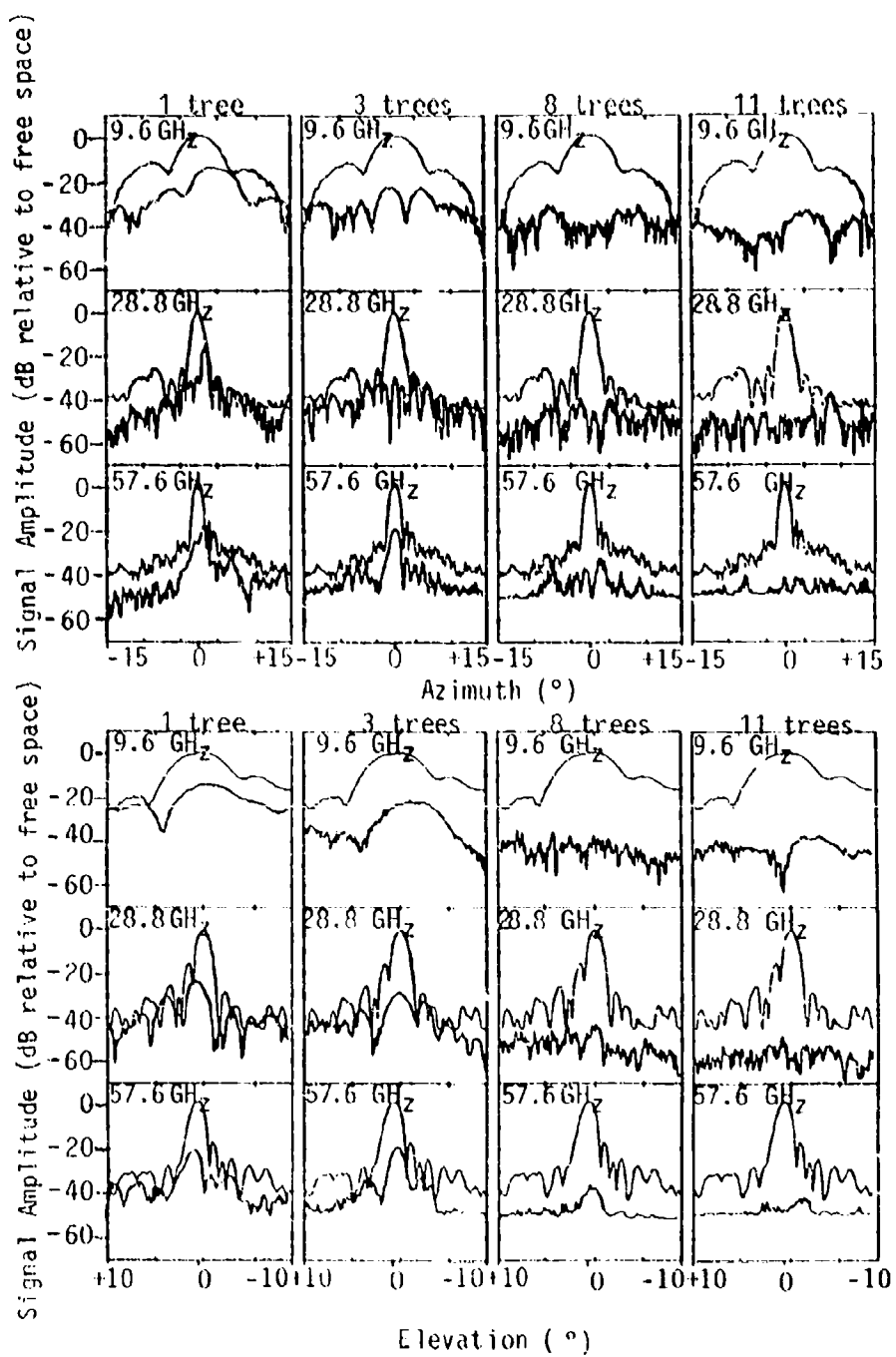


FIGURE 26: Directional Dependence of Received Power at Height of 6 m with 1, 3, 8 and 11 Trees in Path.  
 Conditions are same as in Figure 25.  
 (From Violette and Espeland [2].)

the comparison has to be regarded with caution since the theoretical model contains a priori assumptions and strong simplifications and is not identical with the experimental set-up. In particular, the theoretical model applies to a forest half-space illuminated by a plane wave, while in actuality the incident beam has a finite cross section and the trees have a finite height so that losses occur due to radiation into the ground and into the air region above the forest canopy; such losses are not accounted for in the theory.

In the following, a critical assessment is attempted in how far each of the four theoretical parameters can be determined from the experimental data. For the purpose of this assessment, the parameters are rewritten in the form  $\Delta_{YS}$ ,  $\sigma_T = \sigma_A + \sigma_S$ ,  $W = \sigma_S / (\sigma_A + \sigma_S)$ , and  $\alpha$ .

(1) The width  $\Delta_{YS}$  of the forward lobe of the phase function determines the (changing) beamwidth and amplitude of the  $I_1$ -component of the incoherent intensity, and would have to be determined from the experimental curves of Figs. 25 and 26. But these curves are not in a form to facilitate comparison with theoretical data and no attempt is made here to specify  $\Delta_{YS}$  from this data. For the following discussion,  $\Delta_{YS}$  is not a critical quantity and we shall assume, as in the theoretical curves of Figs. 14 to 18, that the forward lobe of the phase function has a 3 dB beamwidth of  $6^\circ$ , though this value may be rather small.

(2) The extinction cross section  $\sigma_T$  determines the attenuation rate at short distances into the random medium where the coherent component dominates. With Equation (40), we have in this range:

$$P_R / P_{\max} = e^{-\sigma_T Z} = e^{-\sigma_T Z}$$

In accordance with the experimental situation, we have assumed here that  $\sigma_R = \sigma_p = 0$ . The relation permits one to determine  $\sigma_T$  from the measured range dependence curves of Figs. 23 and 24. Recalling that the tree spacing is  $\approx 13$  m, one finds

$$\sigma_T = \sigma_A + \sigma_S \approx \begin{cases} 0.4 \text{ m}^{-1} & \text{for trees in leaf} \\ 0.25 \text{ m}^{-1} & \text{for trees without leaves} \end{cases} \quad (43a)$$

These values correspond to the steep initial part of the experimental curves and are typical for both mm-wave frequencies (28.8 and 57.6 GHz) and both heights above ground (4 m and 6 m). However, these values appear to be very high. Since, in a forest, all scatter objects are large compared to a mm wavelength,  $\sigma_T$  should be close to the high frequency limit, which is obtained for  $\lambda_0 \rightarrow 0$ . In this limit, the extinction cross section approaches the obstruction cross section per volume of the random medium. Thus, according to Equation (43a), trees in leaf would obstruct ~40% of the planar field of view for any meter of vegetation depth, and trees without leaves would lead to a 25% obstruction per meter. Although values of this magnitude may occur locally, it is very unlikely that they can be regarded as representative.

A possible explanation for these large  $\sigma_T$  values can be derived from the fact that in a forest environment all scatter objects are large compared to a mm wavelength. Behind large obstructions such as strong branches, deep shadow will exist\* and since the measurements were performed over a path through maximum vegetation density, it is very likely that the receiving antenna was operating within such shadow zones. The measured data may thus indicate a higher value for  $\sigma_T$  than one would obtain in the average, i.e., by performing similar experiments over a number of parallel, laterally offset vegetation paths (including the maximum density path) and by averaging the powers received over these paths. In transport theory, which neglects interference effects, this averaging process is implied.

At large vegetation depths, on the other hand, deep shadow zones are not expected to exist since the incoherent (multiscattered) component is well developed in this region and will "fill in" any potential shadow zones. Hence, it should be possible to achieve good agreement between the experimental and theoretical range dependencies at large  $r$ .

Since the above values for  $\sigma_T$  appear to be very much on the high side, curve fitting of the theoretical and experimental range dependence curves was attempted not only for these  $\sigma_T$  values but for moderately and strongly reduced values of  $\sigma_T$  as well, i.e., for

$$\sigma_T = \begin{cases} 0.3 \text{ m}^{-1} & \text{for trees in leaf} \\ 0.2 \text{ m}^{-1} & \text{for trees without leaves} \end{cases} \quad (43b)$$

\*Note that we are concerned here with the range of small vegetation depths where the coherent (highly directional) component dominates and the incoherent component is not as yet significantly developed.

and

$$\sigma_T = \begin{cases} 0.1 \text{ m}^{-1} & \text{for trees in leaf} \\ 0.05 \text{ m}^{-1} & \text{for trees without leaves} \end{cases} \quad (43b)$$

Using these values, reasonable agreement should be achievable at moderate and large distances into woods. At short distances, discrepancies are unavoidable, since the assumed theoretical attenuation rate of the coherent component differs from the measured rate.

(3) The albedo  $W$  and the ratio  $\alpha$  of the forward scattered power to the total scattered power were adjusted to obtain reasonable overall agreement of the calculated and measured range dependence curves. Agreement was established simply by trial and inspection. Figs. 27 and 28 show the results for the  $\sigma_T$  values of Equations (43a) and (43b), respectively. In these figures the received power in dB (vegetation loss) is plotted as a function of the normalized distance  $\tau = \sigma_T Z$ . The solid lines show the theoretical curves; the experimental curves (dashed lines) are those of Fig. 23 applying to a propagation path at a height of 4 m above ground.

At large  $\tau$ , good overall agreement between the theoretical and experimental range dependence is obtained in particular in Fig. 28. At small  $\tau$ , the agreement is reasonable for trees without leaves; for trees with leaves, the measured vegetation loss is significantly higher than the theoretical loss, in particular near the sharp bend of the experimental curve.

Both figures indicate that the parameters  $W$  and  $\alpha$  must be chosen close to unity to achieve reasonable agreement, i.e.,

$$W, \alpha = 0.9 \text{ to } 0.95.$$

For the small  $\sigma_T$  values of Equation (43b), conclusive results were difficult to obtain since the range of small  $\tau$ , where significant deviations between the theoretical and experimental curves occur, is now extended and the range of large  $\tau$ , where good agreement can be achieved in principle, is correspondingly reduced. However, it appears that, in this case, the conditions on  $W$  and  $\alpha$  are somewhat relaxed leading to values of 0.8 to 0.95 for  $W$  and 0.6 to 0.9 for  $\alpha$  (where the larger  $W$  values correspond to the smaller  $\alpha$  values and vice versa).

It is evident that these results are preliminary and do not lead to definite conclusions concerning the numerical values to be assigned to the four theoretical

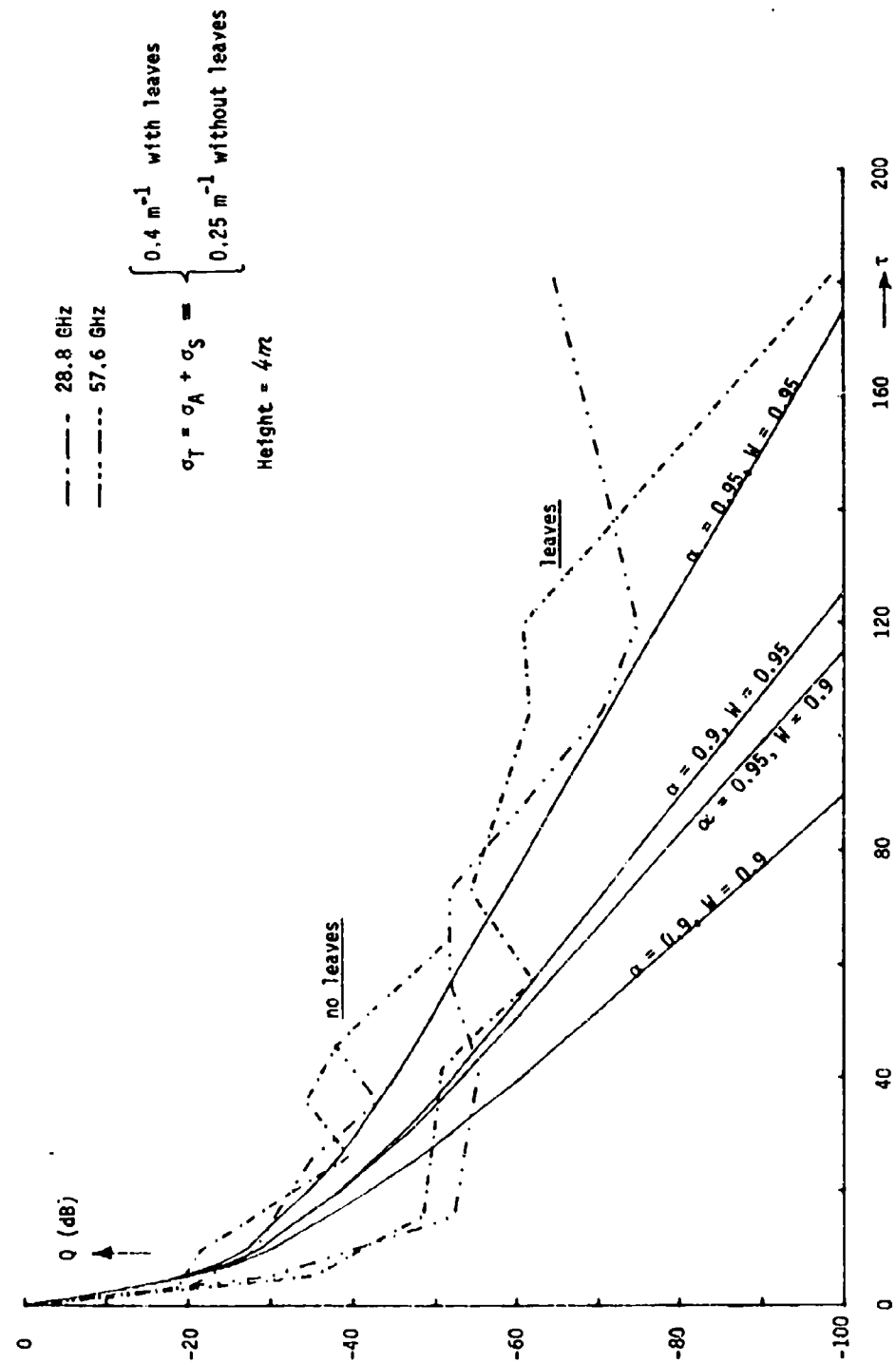


FIGURE 27: Comparison of Theoretical and Experimental Range Dependence

The experimental curves are those of Fig. 23 and apply to a transmission path at 4 m height. In the theoretical curves, the parameters  $W$  and  $\alpha$  were adjusted for good agreement with the experimental curves. The abscissa scale refers to the normalized vegetation depth  $\tau = \sigma_T Z$  where it is assumed that  $\sigma_T = 0.4 \text{ m}^{-1}$  for trees in leave and  $\sigma_T = 0.25 \text{ m}^{-1}$  for trees without leaves

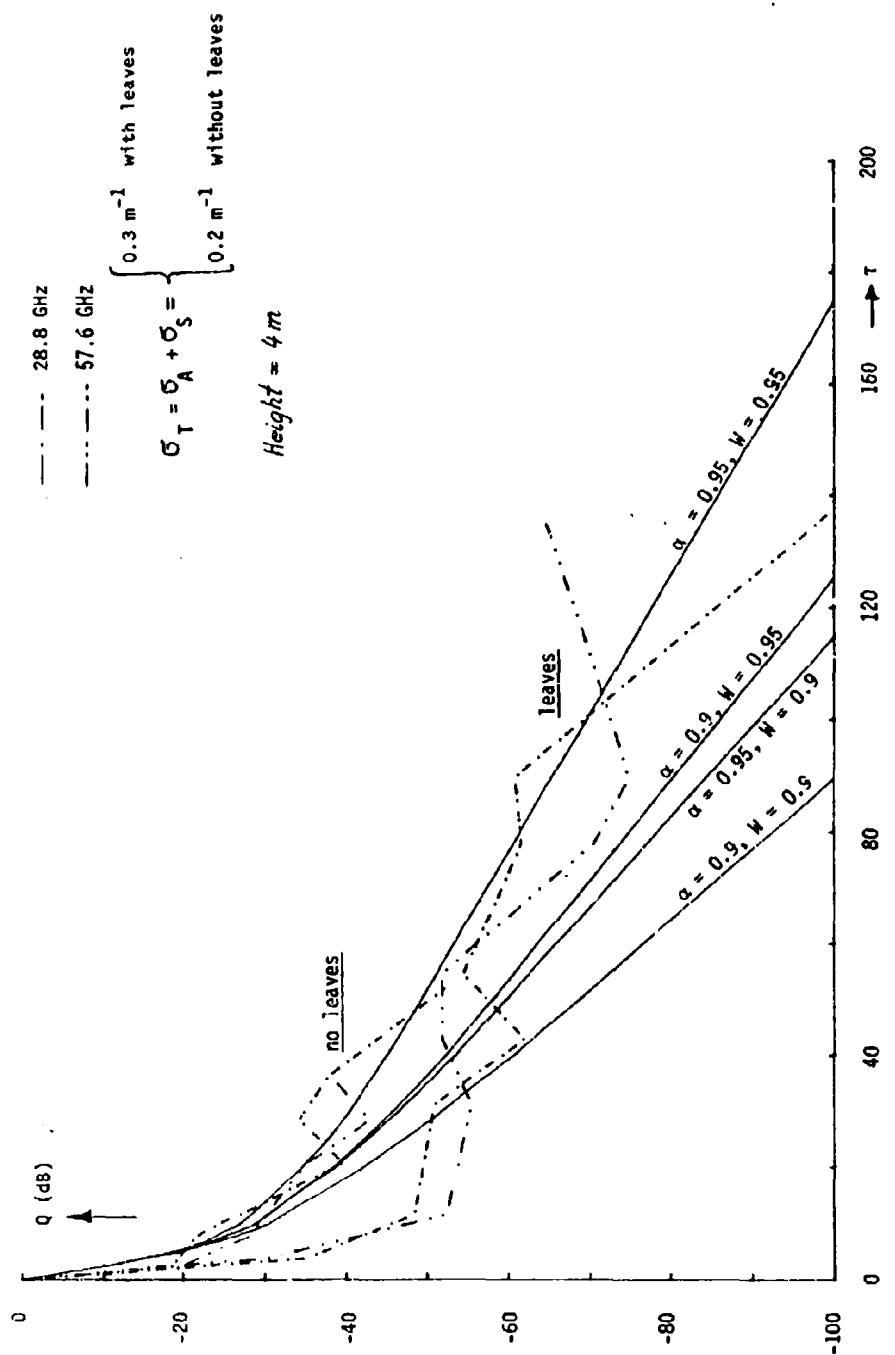


FIGURE 28: Comparison of Theoretical and Experimental Range Dependence.

Same conditions as in Figure 27 except that  $\sigma_T = 0.3 \text{ m}^{-1}$  for trees in leaf and  $\sigma_T = 0.2 \text{ m}^{-1}$  for trees without leaves.

parameters. It appears, however, that both  $\alpha$  and  $W$  should not be too far away from unity which would indicate that forward scattering is a significant effect for mm-wave propagation in woods and forests, and that scattering exceeds absorption by a substantial margin.

## V. CONCLUSIONS

A theoretical approach for the study of mm-wave propagation in woods and forest has been derived and compared to experimental data obtained by an independent investigation [1, 2]. The theory models the vegetation environment as a statistically homogeneous random medium of scatterers characterized by a scatter function (phase function) with a narrow forward lobe and an isotropic background. The scalar transport equation has been used to determine both the coherent and the incoherent field intensities in this medium; the particular problem solved is that of a vegetation halfspace illuminated by a plane wave incident from the air halfspace. The propagation and scatter properties of the vegetation medium are characterized by four parameters which, in principle, can be determined by a comparison of theoretical and experimental results. Numerical evaluations have provided information on the range dependence of mm-waves in woods and forests, and on beam broadening effects.

Comparison with measured data has shown good qualitative agreement between theory and experiments. Both indicate that the attenuation rate of mm waves in woods and forests decreases from a high value at small distances into the medium to a lower value at large distances, and that significant beam broadening occurs, resulting in a very broad beamwidth at large vegetation depths. Reasonably good quantitative agreement between experimental and theoretical results can be established at large vegetation depths (by appropriate adjustment of the parameters of the theoretical model). But the experimental data indicates a higher attenuation rate at short distances into woods than can be accommodated by the present theory. The comparison between theory and experiments has not yielded conclusive quantitative results at the present stage; but it indicates that the forest environment at mm wavelength is a strongly scattering medium whose scatter cross section per volume substantially exceeds the absorption cross section and that strong forward scattering occurs, which is expected since all scatter objects have large dimensions compared to a mm wavelength.

Further study is needed in the following areas:

(1) The very high attenuation rate measured at short distances into woods and the rather sharp transition to a region of lower attenuation rate, which occurs after transmission through a few trees, requires explanation.

(2) More conclusive (experimental or theoretical) information is needed on the numerical values to be assigned to the four (averaged) parameters by which the theory characterizes the forest environment at mm wavelength. These parameters include the scatter cross section per volume, the absorption cross section per volume, the width of the forward lobe of the scatter characteristic (phase function), and the ratio of the forward scattered power to the total scattered power. In more general terms, the characterization of the forest environment at mm wavelengths by a set of suitably defined, measurable electrical parameters is a very important, but up to now, unresolved problem. The theory presented here is a first attempt in this direction.

(3) The present theory deals with the simple model of a forest halfspace with a planar boundary surface illuminated by a plane wave. A more realistic model would replace the forest halfspace by a two-layer horizontal slab model over a ground plane with suitably defined absorption and scattering properties. The model is indicated in Fig. 29. Furthermore, a vector transport equation formulation of the problem is needed if depolarization effects of mm waves in forests are to be included in the theory. Analytical/numerical difficulties in treating a model of this type, however, may be formidable.

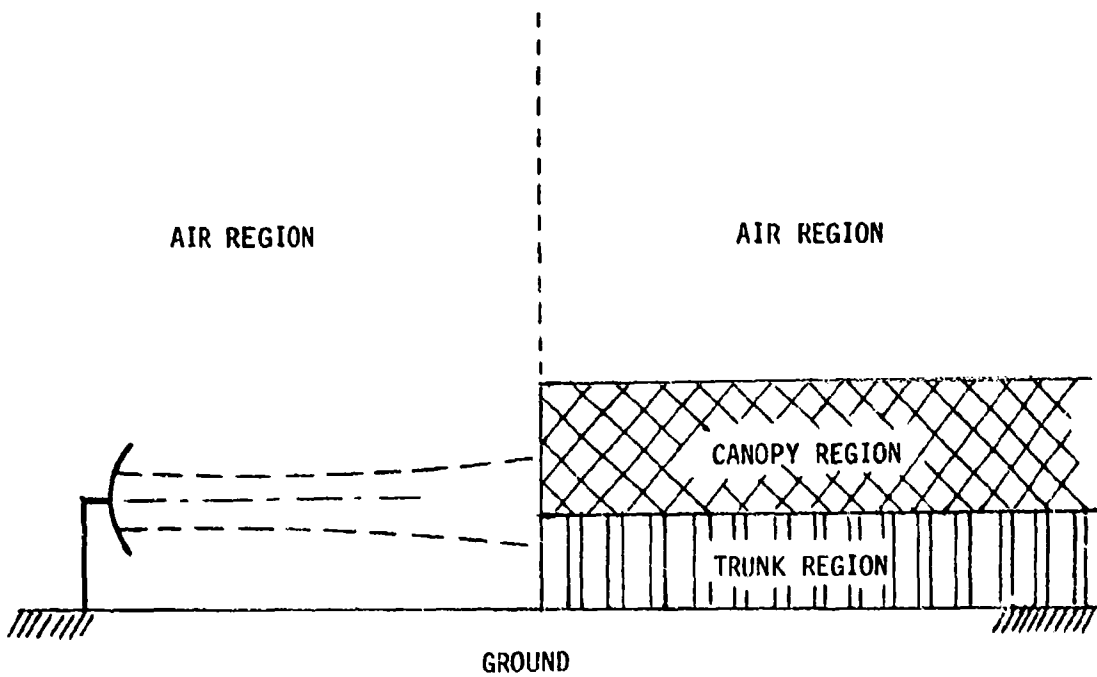
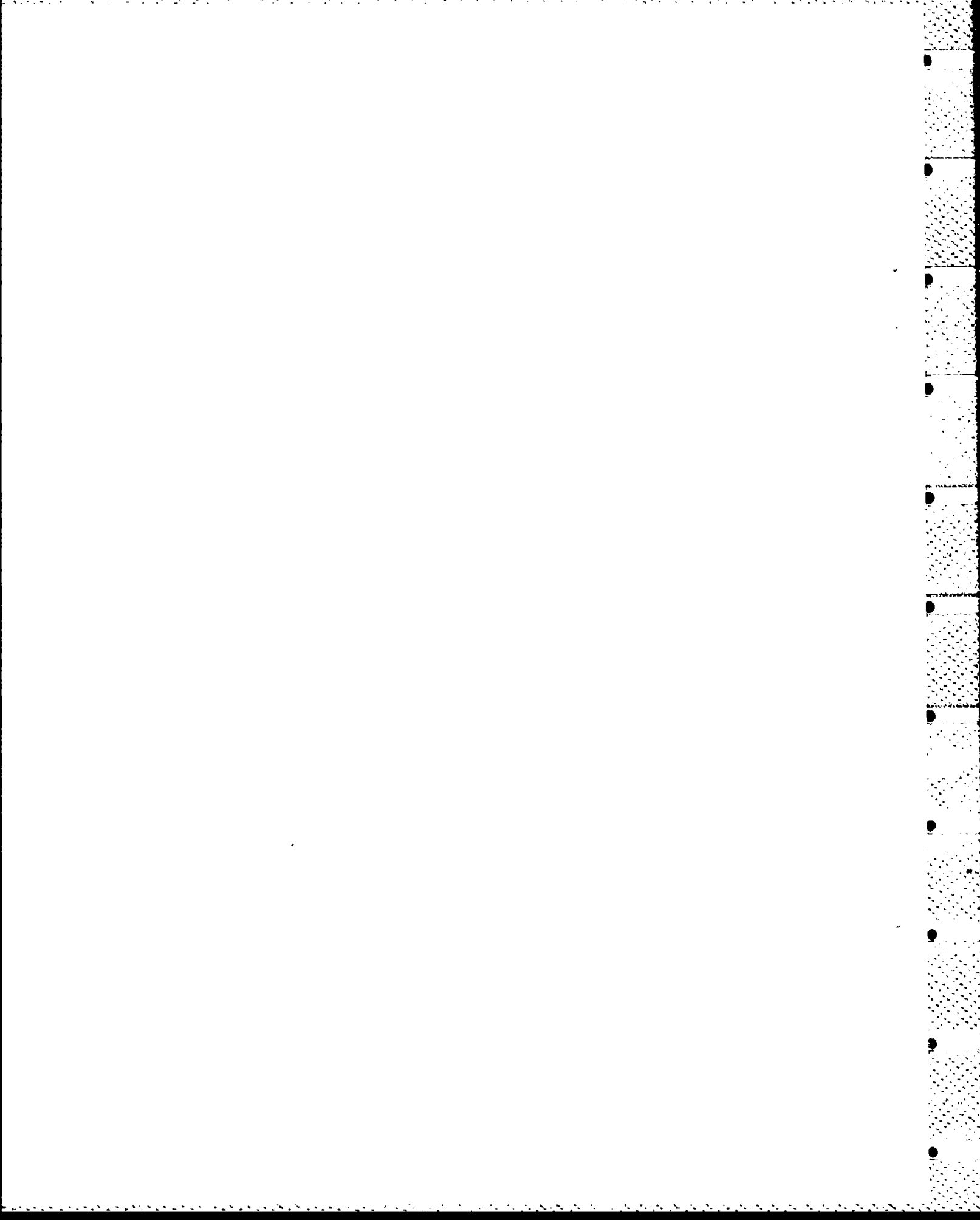


FIGURE 29: Advanced Theoretical Model for the Analysis of Millimeter Wave Propagation in Woods and Forests.

REFERENCES

- [1] E. J. Violette, R. H. Espeland, A. R. Mitz and F. A. Goodknight, SHF - EHF Propagation Through Vegetation on Colorado East Slope, R&D Technical Report CECOM-81-CS020-F, Fort Monmouth, NJ, June 1981.
- [2] E. J. Violette and R. H. Espeland, Vegetation Loss Measurements at 9.6, 28.8 and 57.6 GHz Through a Pecan Tree Orchard in Texas, R&D Technical Report CECOM-83-2, Fort Monmouth, NJ, March 1983.
- [3] A. Ishimaru, Wave Propagation and Scattering in Random Media, Vol. 1, Chapter 7 and following, Academic Press, New York, 1978.
- [4] S. Chandrasekhar, Radiation Transfer, Dover Publications, Inc., New York, 1960.
- [5] K. Case and P. Zweifel, Linear Transport Theory, Addison-Wesley, 1969.
- [6] M. N. Ozisik, Radiative Transfer and Interactions with Conduction and Convection, John Wiley and Sons, 1973.



## APPENDIX A

### Energy Density Associated with $I_1$ .

The integral

$$U_1(z) = \int_0^{2\pi} \int_0^{\pi} I_1(z; \theta, \phi) \sin \theta d\theta d\phi \quad (A.1)$$

which appears on the right side of Equation (16b) can be evaluated in closed form. We use Equation (16a) and perform an integration in  $\theta, \phi$  (over  $\Omega = 4\pi$ ) on both sides. This leads to the following differential equation for  $U_1(z)$ :

$$\cos \theta_p \frac{dU_1}{dz} + (\sigma_A + (1-\alpha)\sigma_S)U_1 = -\frac{\sigma_A + \sigma_S}{\cos \theta_p} z \quad (A.2)$$

We have made use here of the relation

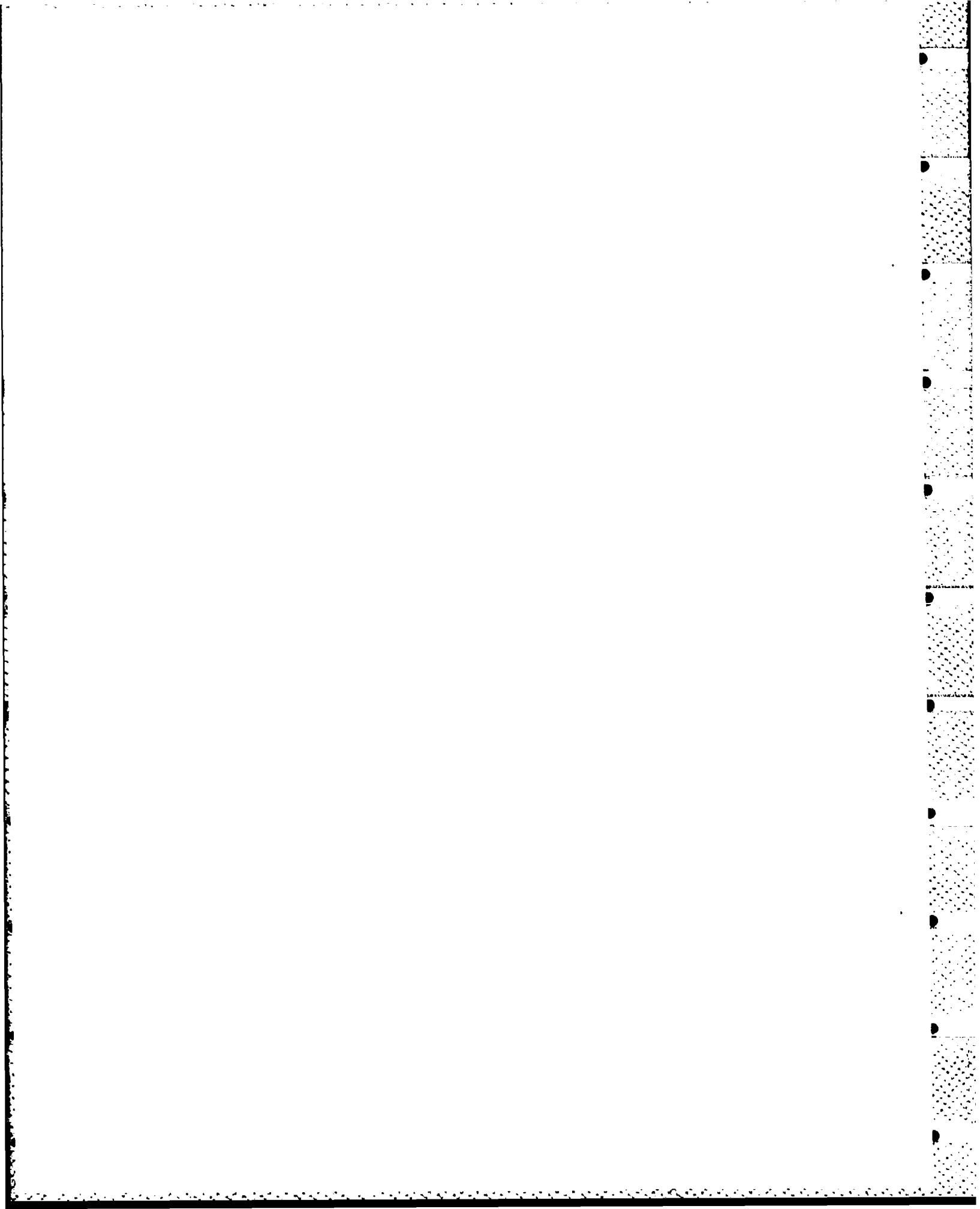
$$\frac{1}{4\pi} \int_0^{2\pi} \int_0^{\pi} q(\gamma) \sin \theta d\theta d\phi = 1$$

which follows from Equations (4) and (14a), and have replaced the factor  $\cos \theta$  on the right side of Equation (16a) by  $\cos \theta_p$ . The approximation is discussed in the main text.

Equation (A.2), a linear differential equation of first order, can be solved in closed form. With the boundary condition  $U_1(0) = 0$  which takes into account that  $I_1(0; \theta, \phi)$  is zero in the range of forward directions,  $0 \leq \theta \leq \frac{\pi}{2}$  (see Equation (21a)), and negligible in the range of backward radiation,  $\frac{\pi}{2} \leq \theta \leq \pi$ , we obtain:

$$U_1(z) = S_p \left\{ \exp \left( -\frac{\sigma_A + (1-\alpha)\sigma_S}{\cos \theta_p} z \right) - \exp \left( -\frac{\sigma_A + \sigma_S}{\cos \theta_p} z \right) \right\} \quad (A.3)$$

As a final remark, we note that  $U_1(z)$  is proportional to the energy density associated with the specific intensity  $I_1$ .



## APPENDIX B

### Solution of Recursion Relation for $I_1$ .

The coefficients  $b_m(\theta, \phi)$  of the specific intensity  $I_1$  are determined by the recursion relations (Equations (23) of main text):

$$b_1(\theta, \phi) = \frac{S_p}{4\pi} \frac{\cos \theta_p}{\cos \theta} \cdot q(\gamma_p) \quad (B.1)$$

$$b_m(\theta, \phi) = \frac{1}{4\pi} \frac{\cos \theta}{\cos \theta_p} \frac{1}{m} \int_0^{2\pi} \int_0^\pi q(\gamma) b_{m-1}(\theta', \phi') \sin \theta' d\theta' d\phi' \quad (B.2)$$

$m = 2, 3, \dots$

$$\text{where } \cos \gamma = \cos(\phi - \phi') \sin \theta \sin \theta' + \cos \theta \cos \theta'$$

$$\cos \gamma_p = \cos(\phi - \phi_p) \sin \theta \sin \theta_p + \cos \theta \cos \theta_p$$

$$\text{For } q(\gamma) = \left(\frac{2}{\Delta_{YS}}\right)^2 e^{-\left(\frac{\gamma}{\Delta_{YS}}\right)^2}, \quad \Delta_{YS} \ll \pi \quad (B.3)$$

these equations can be solved by assuming that  $b_m$  has the general form

$$b_m(\theta, \phi) = B_m \left(\frac{2}{\Delta_{Ym}}\right)^2 e^{-\left(\frac{\gamma_p}{\Delta_{Ym}}\right)^2} \quad (B.4)$$

$$\text{with } \Delta_{Ym} \ll \pi$$

$$m = 1, 2, \dots$$

Equation (B.2) requires that

$$B_m \left(\frac{2}{\Delta_{\gamma_m}}\right)^2 e^{-\left(\frac{\gamma_p}{\Delta_{\gamma_m}}\right)^2} = \frac{B_{m-1}}{4\pi} \frac{\alpha \omega}{\cos \theta_p} \frac{1}{m} \left(\frac{4}{\Delta_{\gamma_S} \Delta_{\gamma_{m-1}}}\right)^2 \times \\ \times \int_0^{2\pi} \int_0^\pi \exp\left(-\left(\frac{\gamma}{\Delta_{\gamma_S}}\right)^2 - \left(\frac{\gamma'_p}{\Delta_{\gamma_{m-1}}}\right)^2\right) \sin \theta' d\theta' d\phi'$$
(B.5)

where  $\cos \gamma'_p = \cos (\phi_p - \phi') \sin \theta_p \sin \theta' + \cos \theta_p \cos \theta'$

In evaluating the integral on the right side, it is important to understand that in the integrand we are dealing with three directions, i.e.,  $\theta, \phi$  and  $\theta_p, \phi_p$  and  $\theta', \phi'$ . For the purpose of the integration, the directions  $\theta, \phi$  and  $\theta_p, \phi_p$  are fixed while  $\theta', \phi'$  varies. Note, furthermore, that  $\gamma$  and  $\gamma'_p$  are the angles which the variable direction includes with the fixed directions while  $\gamma_p$ , the angle between  $\theta, \phi$  and  $\theta_p, \phi_p$  is a constant; see Fig. B1.

Since it is assumed that the "beamwidths"  $\Delta_{\gamma_S}$  and  $\Delta_{\gamma_m}$  are small, the integral will have appreciable values only if the directions  $\theta, \phi$  and  $\theta_p, \phi_p$  are in close proximity to each other so that there is a  $\theta', \phi'$  range in which both  $\gamma$  and  $\gamma'_p$  are small simultaneously. Only this range will yield a significant contribution to the integral. To determine this contribution, we introduce a local coordinate system on the unit sphere over which the  $\theta', \phi'$  integration is performed. This coordinate system is indicated in Fig. B2 in planar projection. The coordinate  $u$  is counted along the great circle through  $\theta, \phi$  and  $\theta_p, \phi_p$ ; the coordinate  $v$  is counted in the direction normal to this circle. Both  $u$  and  $v$  are measured in radians. Evidently,

$$\gamma^2 = \left(\frac{\gamma_p}{2} + u\right)^2 + v^2, \quad \gamma'_p = \left(\frac{\gamma_p}{2} - u\right)^2 + v^2$$

and

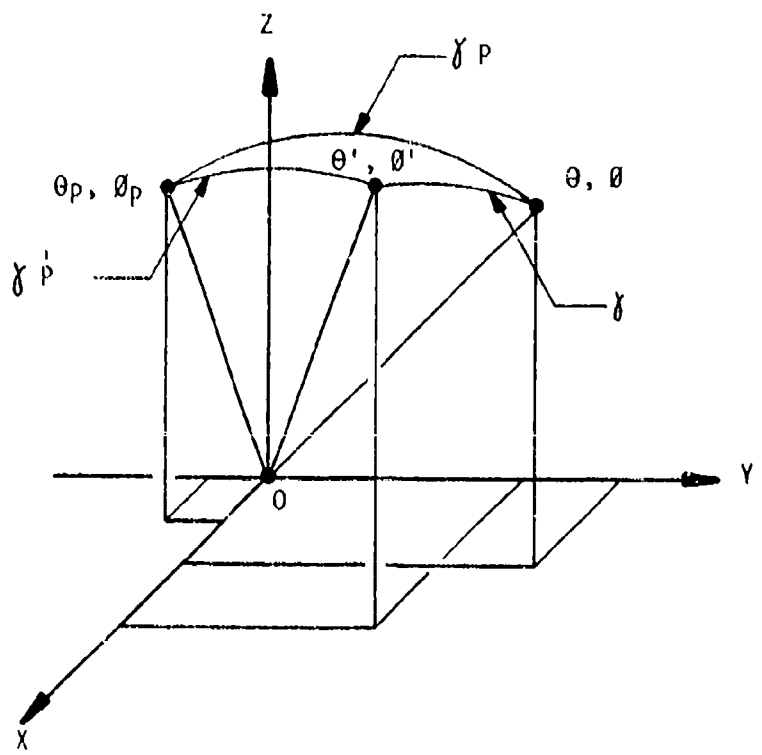


FIGURE B1: Directions  $v, \phi$  and  $v'_p, \phi'_p$  and  $v', \phi'$ .  
 For purposes of performing integration in Equation (B.5).  
 Direction  $v', \phi'$  is variable, while directions  $v, \phi$  and  
 $v'_p, \phi'_p$  are fixed.

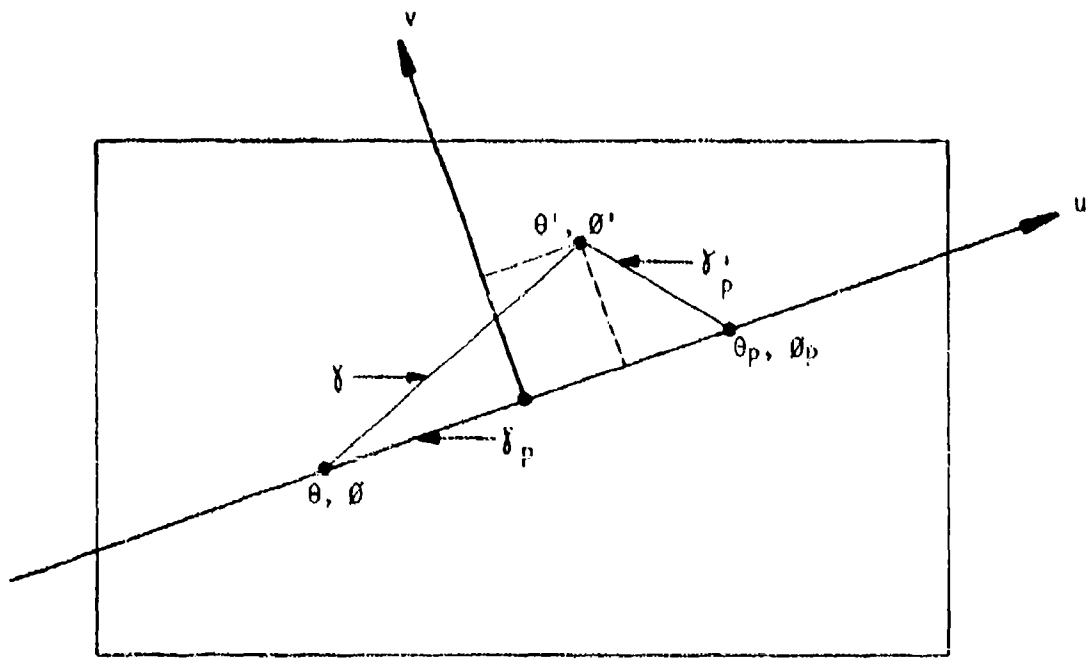


FIGURE B2: Local Coordinate System on the Unit Sphere  
(Planar Projection)

$$\begin{aligned}
& \int_0^{2\pi} \int_0^\pi \exp \left\{ - \left( \frac{\gamma}{\Delta \gamma_S} \right)^2 - \left( \frac{\gamma_p}{\Delta \gamma_{m-1}} \right)^2 \right\} \sin \theta \, d\theta \, d\phi \\
& \approx \iint_{-\infty}^{+\infty} \exp \left\{ - \left[ \left( \frac{\gamma_p/2+u}{\Delta \gamma_S} \right)^2 + \left( \frac{\gamma_p/2-u}{\Delta \gamma_{m-1}} \right)^2 \right] - \left[ \frac{1}{\Delta \gamma_S^2} + \frac{1}{\Delta \gamma_{m-1}^2} \right] v^2 \right\} du dv \\
& = \frac{\gamma_p^2}{\Delta \gamma_S^2 + \Delta \gamma_{m-1}^2} \\
& = \frac{\pi}{\frac{1}{\Delta \gamma_S^2} + \frac{1}{\Delta \gamma_{m-1}^2}} e^{-\frac{\pi^2}{\Delta \gamma_S^2 + \Delta \gamma_{m-1}^2}}
\end{aligned} \tag{B.6}$$

The extension of the range of integration to infinity has a negligible effect on the value of the integral. Equation (B.5) is satisfied provided

$$\frac{1}{\Delta \gamma_m^2} = \frac{1}{\Delta \gamma_S^2 + \Delta \gamma_{m-1}^2}, \quad B_m = B_{m-1} \cdot \frac{1}{m} \cdot \frac{\alpha W}{\cos \theta_p}$$

With Equations (B.1), (B.3) and (B.4), we have

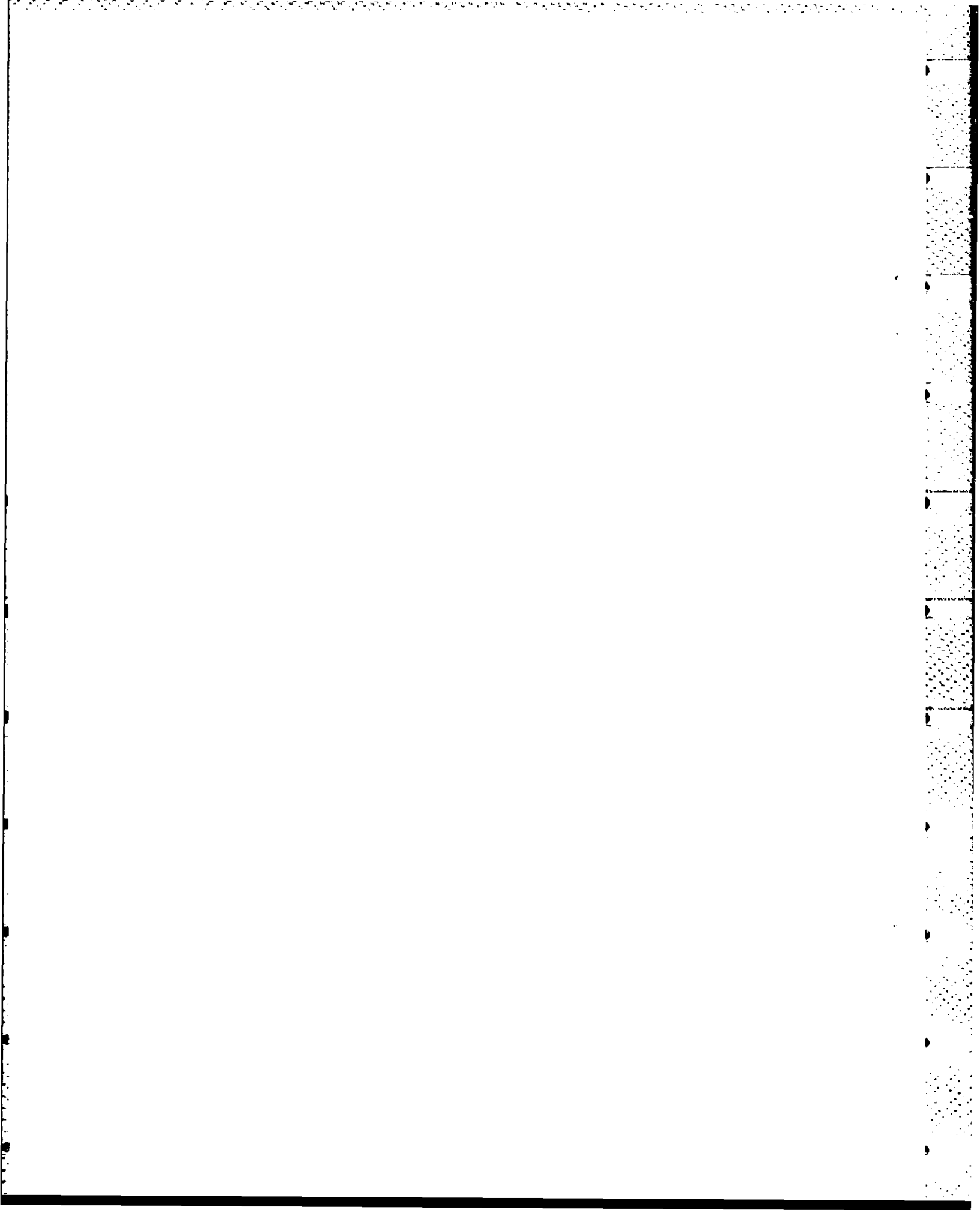
$$\Delta \gamma_1 = \Delta \gamma_S, \quad B_1 = \frac{s_p}{4\pi} \frac{\alpha W}{\cos \theta_p}$$

Hence, with Equations (B.6b)

$$\Delta \gamma_m = \sqrt{m} \Delta \gamma_S, \quad B_m = \frac{s_p}{4\pi} \frac{1}{m!} \left( \frac{\alpha W}{\cos \theta_p} \right)^m$$

and with Equation (B.4):

$$b_m(u, \phi) = \frac{s_p}{4\pi} \frac{1}{m!} \left( \frac{\alpha W}{\mu_p} \right)^m \cdot \frac{4}{m \cdot \Delta \gamma_S^2} \cdot e^{-\frac{\gamma_p^2}{m \cdot \Delta \gamma_S^2}} \tag{B.7}$$



## APPENDIX C

### Asymptotic Behavior of $I_2$ .

The asymptotic behavior of  $I_2$  for large  $\hat{\tau}$  is determined by the expansion term associated with the largest eigenvalue,  $S_N$ , which is the only eigenvalue greater than unity and, thus, provides the slowest attenuation rate. With Equations (25) and (31), we have

$$I_2(\hat{\tau}; \mu) \rightarrow \frac{S_p}{2\pi} A_N e^{-\frac{\hat{\tau}}{S_N}} \sum_{n=0}^N \frac{F_n(\mu)}{1 - \frac{\mu_n}{S_N}} \quad \text{for } \hat{\tau} \rightarrow \infty \quad (C.1)$$

where  $A_N$  is an amplitude coefficient determined by the boundary condition at  $\hat{\tau} = 0$  and  $S_N$  is the largest solution of the characteristic Equation (32). With Equation (30b), this characteristic equation may be written in the form

$$\frac{N}{2} \sum_{n=0}^N \frac{\Delta \mu_n}{1 - \frac{\mu_n}{S_N}} = 1 \quad (C.2)$$

where  $\Delta \mu_n = \frac{\mu_{n+1} - \mu_{n-1}}{2}$

As  $N$  increases the sum on the right side of Equation (C.1) approaches the function  $(1 - \frac{\mu}{S_N})^{-1}$ . Since  $S_N > 1$ , no singularity will occur and we have

$$I_2(\hat{\tau}; \mu) \rightarrow \frac{S_p}{2\pi} e^{-\frac{\hat{\tau}}{S_a}} A_a f_a(\mu) \quad \text{for } \hat{\tau} \rightarrow \infty \quad (C.3)$$

where

$$f_a(\mu) = \frac{1}{1 - \frac{\mu}{S_a}}, \quad A_a = \left( \frac{A_N}{1 - \frac{1}{S_N}} \right)_{N \rightarrow \infty}, \quad S_a = (S_N)_{N \rightarrow \infty}$$

Similarly, the sum on the left side of Equation (C.2) converges towards the integral  $\int_{-1}^{+1} (1 - \frac{\mu}{S_a})^{-1} d\mu$  as  $N \rightarrow \infty$  and the characteristic equation for  $S_a$  takes the form

$$\frac{\hat{W}}{2} \int_{-1}^{+1} \frac{d\mu}{1 - \frac{\mu}{S_a}} = \frac{\hat{W}}{2} \ln\left(\frac{S_a + 1}{S_a - 1}\right) = 1 \quad (C.4)$$

The quantities  $S_a$ ,  $A_a$  and  $i_a$  are shown in Figs. 7, 8 and 9 as functions of  $\hat{W}$ . While  $f_a$  and  $S_a$  are fully described by Equations (C.3) and (C.4) and depend on  $\hat{W}$  only, the amplitude  $A_a$  depends also on the boundary conditions at  $\hat{\tau} = 0$  and the direction of incidence of the primary plane wave. Fig. 9 implies  $\theta_p = 0$  and boundary condition (21b), i.e.,  $I_2(0, \mu) = 0$  for  $0 \leq \mu \leq 1$ . Numerical evaluations have shown that for sufficiently large  $N > 20$ , the highest order term ( $k = N$ ) in Equation (34) approximates Equation (C.3) closely.

Equations (C.3) and (C.4) can also be obtained directly by rigorous solution of Equation (19b) with the forcing term suppressed. This term decreases with  $\exp(-\hat{\tau}/\mu_p)$  and is insignificant at large  $\hat{\tau}$ . This approach, however, leaves the asymptotic amplitude  $A_a$  undetermined.